

ROTATING FLOWS AROUND SHARP CORNERS
AND IN CHANNEL MOUTHS

By

JOSEF YURI CHERNIAWSKY

B.Sc., McGill University, 1973

M.Sc., University of Victoria, 1977

A THESIS SUBMITTED IN PARTIAL FULFILLMENT OF
THE REQUIREMENTS FOR THE DEGREE OF
DOCTOR OF PHILOSOPHY

In

THE FACULTY OF GRADUATE STUDIES

Department of Oceanography

We accept this thesis as conforming
to the required standards

THE UNIVERSITY OF BRITISH COLUMBIA

July 1985

© Josef Yuri Cherniawsky, 1985

24

In presenting this thesis in partial fulfilment of the requirements for an advanced degree at the University of British Columbia, I agree that the Library shall make it freely available for reference and study. I further agree that permission for extensive copying of this thesis for scholarly purposes may be granted by the head of my department or by his or her representatives. It is understood that copying or publication of this thesis for financial gain shall not be allowed without my written permission.

Department of Oceanography

The University of British Columbia
1956 Main Mall
Vancouver, Canada
V6T 1Y3

Date Sep. 30, 1985

supervisor: Dr. Paul H. LeBlond

Abstract

This thesis examines buoyancy driven steady flows in mouths of sea straits and around coastal protrusions. At high latitudes, the Coriolis force keeps these currents banked against the coast even around relatively sharp re-entrant (convex) corners with radii of curvature that are comparable to the width of the current. On the other hand, if the radius of curvature of the corner is much smaller than the width of the current, the current may leave the coast at the apex of the corner.

A central part of the thesis is the solution of the nonlinear problem of a steady inviscid reduced gravity flow in a wedge, $0 < \theta < \pi/a$ (with $a > 1/2$), around a sharp corner on an f -plane. An exponential upper layer upstream depth profile, $h = H \exp(-x/X)$ (where x and X are the offshore distance and the current width scale, respectively), is combined with conservation of potential vorticity, Bernoulli and transport equations. The resulting nonlinear equations are expanded in a Rossby number $\epsilon = V/fX$ (where f is the Coriolis parameter and V is the upstream boundary value of velocity). The $O(1)$ and $O(\epsilon)$ equations are solved. First, they are simplified via transformations of the transport streamfunction variables: $\Psi_0 = p^{4/3}$ and $\Psi_1 = 2p^{1/3}q$. By

modifying the results of Bromwich's (1915) and Whipple's (1916) diffraction theory, the $O(1)$ solution is expressed in a compact integral form,

$$p = \frac{2a \sin(a\theta)}{\pi} \int_0^{\infty} \frac{\cos(kr \sin hu) \cosh(au) du}{\sinh^2(au) + \sin^2(a\theta)}.$$

The $O(\epsilon)$ contribution q is calculated using an approximate Green's function method. The wedge of an angle $3\pi/2$ ($a=2/3$) is used as an example to show details of the solution. The results exhibit the relative importance of the centrifugal, Coriolis and pressure gradient forces. Centrifugal upwelling (surfacing) of the interface occurs very close to the apex. For a rounded re-entrant corner, the upwelling is important only if the radius of curvature is much smaller than the lateral scale X . Moreover, for re-entrant corners, the flow is supercritical within an arc, whose size depends upon the Rossby number and the angle of the wedge. Using two or more corner solutions, plausible flow streamlines can be generated in more complicated domains, as long as no two corners are closer than the Rossby radius of deformation. This procedure is illustrated with two examples: (a) circulation in a channel mouth and (b) flow around a square bump in a coastline. Finally, baroclinic circulation is modeled for boundaries that approximate coastlines near the mouth of Hudson Strait.

TABLE OF CONTENTS

	page
ABSTRACT	ii
LIST OF FIGURES	vi
ACKNOWLEDGEMENTS	ix
CHAPTER 1: INTRODUCTION	1
CHAPTER 2: MODELS OF SEA STRAITS	8
CHAPTER 3: STATEMENT OF THE PROBLEM	15
CHAPTER 4: THE UPSTREAM PROFILE	19
CHAPTER 5: SOLUTIONS INSIDE A CHANNEL	24
CHAPTER 6: SCALING AND DERIVATION OF THE GOVERNING EQUATIONS	28
CHAPTER 7: ROTATING FLOW AROUND A SHARP BEND	35
THE $O(1)$ SOLUTION	36
THE $O(\epsilon)$ SOLUTION	42
THE VALIDITY OF THE SOLUTION	45
SUPERCRITICAL FLOW	46
SEPARATION	48
CHAPTER 8: THE CASE OF MORE COMPLICATED GEOMETRIES	64
CIRCULATION IN THE MOUTH OF A CHANNEL	64
FLOW AROUND A SQUARE BUMP	68
CHAPTER 9: BAROCLINIC CIRCULATION IN HUDSON STRAIT	76
THE TRANSPORTS	77
LATERAL SCALES	79
THE CIRCULATION	82
CHAPTER 10: DISCUSSION	93

REFERENCES	98
APPENDIX A: DERIVATION OF THE $O(\epsilon)$ EQUATION FOR s_1	102
APPENDIX B: BEHAVIOUR OF s_0 FOR SMALL OR LARGE r	104
APPENDIX C: THE EXTENT OF THE CENTRIFUGAL UPWELLING	107

LIST OF FIGURES

figure #		page
1	The western part of the sub-polar gyre of the North Atlantic.	4
2	Re-entrant circulation in (a) Lancaster Sound and (b) Hudson Strait.	5
3	(a) Mean currents in Hudson Strait in Aug.-Oct., 1982. (b) Current trajectories near the mouth of Hudson Strait at moorings 6 and 7.	6
4	Marsili's (1681) experiment, designed to duplicate an estuarine-type circulation in the Strait of Bosphorus.	12
5	Temperature, salinity and sigma-t section across the mouth of Hudson Strait.	13
6	Sample surface configuration from Gill, 1977.	14
7	Schematic representation of a channel mouth.	18
8	3 profiles of the upper layer depth: (a) linear near $h=H(1-x/X)$, (b) exponential $h=He^{-x/X}$ and (c) exponential $h=D+He^{-x/X}$.	23
9	Profiles of h inside a channel for (a) $Q_- = Q_+$ and (b) $Q_- = 2Q_+$, for several values of width, d .	27
10	The incoming current profile as an evanescent "wave" emanating from the boundary along $\theta = \pi/a$.	53

figure #		page
11	Diffraction term $2F(\psi)$, with $\psi = \pi/a - \theta$ and $a = 2/3$: (a) its functional behaviour, (b) as a rotating sink of a unit strength.	54
12	(a) The $O(1)$ streamfunction $s_0 = p^{2/3}$ and its homogeneous counterpart, s_h . (b) Contours of M .	55
13	(a) The right hand side of (6.23), f . (b) The $O(\epsilon)$ streamfunction variable s_1 . (c) The total transport streamfunction $\Psi = \Psi_0 + \epsilon\Psi_1$, for $\epsilon = 0.5$. (d) Comparison between Ψ_0 ($\epsilon = 0$) and Ψ ($\epsilon = 0.5$).	56
14	(a) The $O(\epsilon)$ depth variable h_1 . (b) Contours and (c) 3-dimensional view of $h = h_0 + \epsilon h_1$, ($\epsilon = 0.5$).	58
15	Depth integrated kinetic energy hU : (a) $\epsilon = 0$, (b) $\epsilon = 0.5$.	60
16	Contours of (a) r_1 , (b) r_2 and (c) F_r , superimposed upon a few streamlines of Ψ ($\epsilon = 0.5$)	61
17	Conceptual drawing of the boundary streamline $\Psi = 1$ (a) just after separation and (b) after reattachment.	63
18	h_0 inside a channel, compared to the exact solution, h , for several values of width, d : (a) $A = 0$ and (b) $A = 1$.	71

figure #		page
19	Circulation in the mouth of a channel: contours of the transport streamfunction Ψ_0 for $d=1.0$, $f=0.1$: (a) $A=0$, (b) $A=1$.	72
20	Location y_0 of the stagnation streamline $\Psi_0(y_0)$ as functions of A , for 3 values of width: $2d=1$, $2d=2$ and $2d=3$.	73
21	(a)-(f) Construction of the solution for a flow around a square bump in a coastline. A square bump in a channel for (g) $A=0$ and (h) $A=1$.	74
22	(a) The eastern Hudson Strait and Ungava Bay area. (b) Simplified model boundaries.	85
23	Temperature and salinity sections in Ungava Bay.	86
24	An example of thermal surface signature of circulation in Hudson Strait and Ungava Bay.	88
25	Ice cover in Ungava Bay and Hudson Strait.	89
26	Temperature, salinity and sigma-t transects across Hudson Strait, Aug. 1982.	90
27	Model contours of (a,c) h_0 and (b,d) Ψ_0 for (a,b) $X=20\text{km}$ and (c,d) $X=30\text{km}$.	91
28	(a) An approximation s_p and the exact s_0 for 3 small values of r . (b) s_1 and s_0 for large r .	106
29	Contours of Ψ and h ($\epsilon=0.5$) for (a) $b=-2$, (b) $b=-3$ and (c) $b=-4$.	112

ACKNOWLEDGEMENTS

First, I extend my gratitude to my supervisor, Dr. Paul LeBlond, for suggesting this interesting problem and for helping with its completion. I am also grateful to a number of people at UBC and IOS for being patient and helpful when I needed their advice. These include Drs. Andrew Bennett, Paul Budgel, David Farmer, Michael Forman, Howard Freeland, Falconer Henry, Humphrey Melling and Steve Pond. Special thanks are due to Drs. Lawrence Mysak and Richard Thomson for their constructive critique of this thesis. I also thank Dr. John Garrett, Division Head of Ocean Physics at IOS, and Dr. Richard Thomson for arranging my two year stay at the Institute (I admit, the view from the window is superb).

Finally, I happily thank my wife, Esther, for her loving support, cheer and encouragement and our children, Tali and Zevi, for just beeing here.

Chapter 1

Introduction

There have been an increasing number of oceanographic investigations of the Canadian Arctic in the past decade. This is mainly due to recent oil exploration activities and increased marine traffic in the area. Details of circulation patterns in Arctic straits have now begun to be determined. While the water movement in the Arctic Archipelago is generally from northwest to southeast (e.g., Collin, 1962), many of the straits are wide enough to accommodate two baroclinic currents in opposite directions (LeBlond, 1980). Because of this, coastal currents in the area tend to loop in and out of channels. In some instances, a portion of the incoming flow continues even further into the channel, against prevailing eastward transports. Some examples of these re-entrant flows may be seen on Figure 1, which shows a part of the sub-polar gyre of the North Atlantic and, in particular, the movement of Baffin Current in and out of Lancaster Sound and Hudson Strait. The understanding of the physical processes which govern the motion of water masses in the area is required for theoretical and predictive models of (a) icebergs and sea-ice hazards to drilling and navigation, (b) pollutant transport from drilling and shipping sources and (c) biological production zones.

The existence of the opposing currents in arctic channels was explained by LeBlond (1980) in terms of simple geostrophic

dynamics of upper layer wedge-type boundary flows. Here, I concentrate mainly on the details of baroclinic currents turning various corners, as they loop in and out of channels (such as Lancaster Sound and Hudson Strait), or navigate coastal protrusions. This topic of rotating flows around sharp corners, and its relation to the circulation in and out of sea straits, has not yet been examined in detail.

The formulation is similar to that used by Whitehead et al. (1974), Gill (1977), Nof (1978a,b) and others, to study the rotational hydraulics of channel flows, but it is not restricted to slowly varying coastlines. The full two-dimensional nonlinear problem is treated here. In contrast to previous investigations, the model potential vorticity is not assumed to be uniform. Instead, it is derived from a chosen upstream profile.

The re-entrant flows in Lancaster Sound and in Hudson Strait were observed and measured via the distribution of water properties (Campbell, 1958; Osborn et al., 1978; Fissel et al., 1982), flow measurements from drifting and moored instruments (LeBlond et al., 1981; Fissel et al., 1982; Drinkwater, 1985), and by iceberg drift observations (Marko et al., 1982). Surface drogue tracks in the mouths of Lancaster Sound and Hudson Strait are shown on Figure 2 (from Fissel et al., 1982; LeBlond et al., 1981). Among the many drogues that were released near the entrances of these two channels, not a single one was observed to penetrate much further than a distance comparable to the width of the channel. On the other hand, current meter records

(Figures 3a,b, from Drinkwater, 1985 and LeBlond, et al., 1981), iceberg sightings (Smith, 1931), geostrophic calculations (Campbell, 1958; Drinkwater, 1985) and drogues released inside the channels (Fissel and Marko, 1978), all show the presence of opposing currents much farther inside these channels. This apparent contradiction will also be addressed.

The plan of this thesis is as follows: certain relevant theoretical models of flows in straits are reviewed in Chapter 2. Chapter 3 contains the formulation of the problem of baroclinic circulation near a channel mouth. Chapter 4 includes discussion about the upstream conditions. One-dimensional solutions far inside a channel are derived in Chapter 5. The governing equations for a two-dimensional reduced gravity flow around an arbitrary corner are derived in Chapter 6 via a regular perturbation expansion in a Rossby number ϵ . The $O(1)$ and $O(\epsilon)$ solutions are calculated in Chapter 7. The re-entrant wedge of an angle $3\pi/2$ is used as an example to show the details of the solution. In Chapter 8, the model is extended to more complicated geometries, such as channel mouths and bumps in coastlines, while in Chapter 9, the model is used to construct a baroclinic circulation in the mouth of Hudson Strait. Finally, an overview of the results and suggestions for further work are presented in the last Chapter.

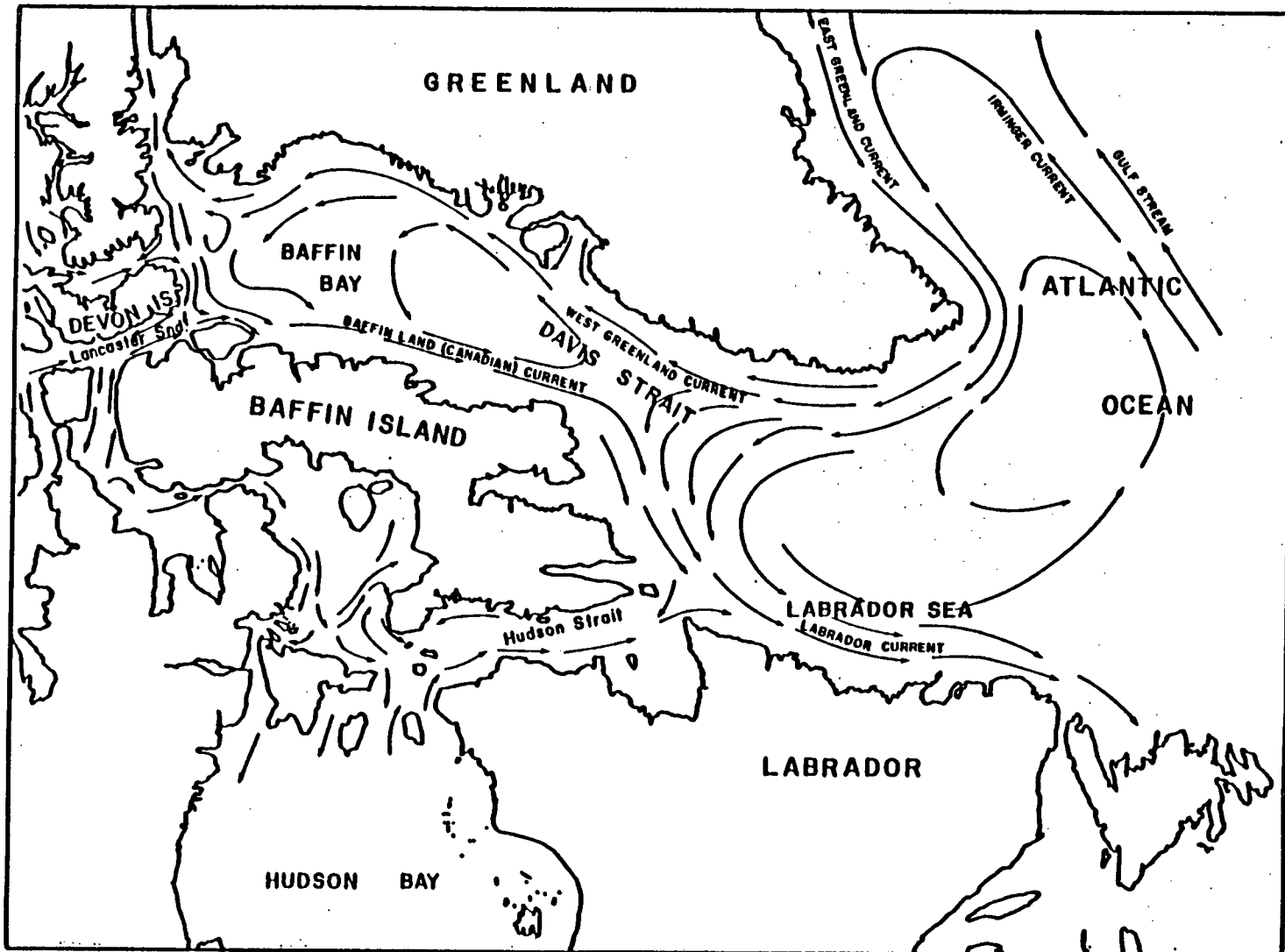


Figure 1. The western part of the sub-polar gyre of the North Atlantic (adapted from Fenco and Slaney, 1978).

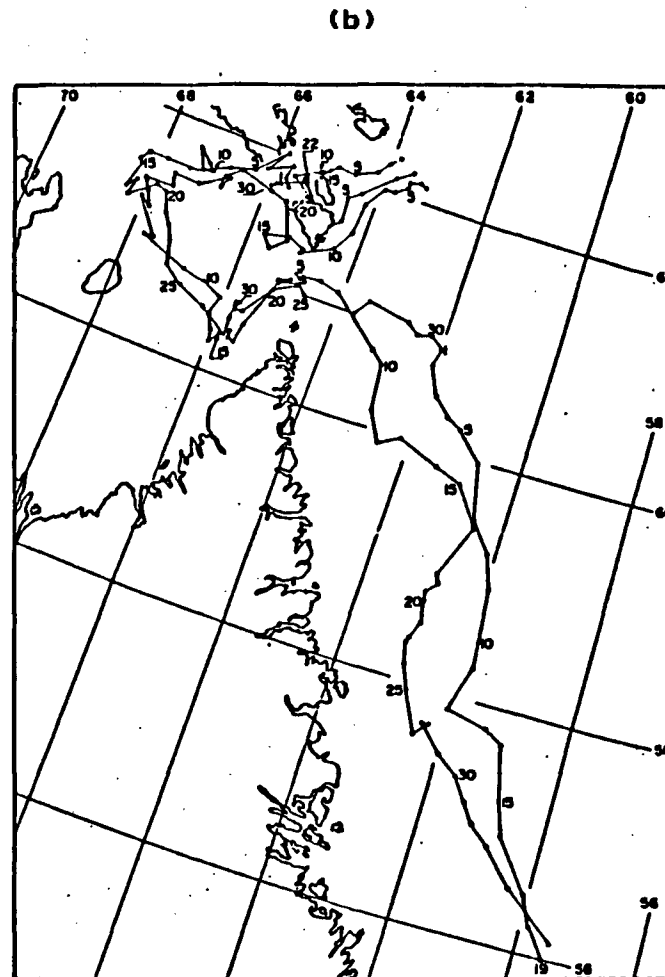
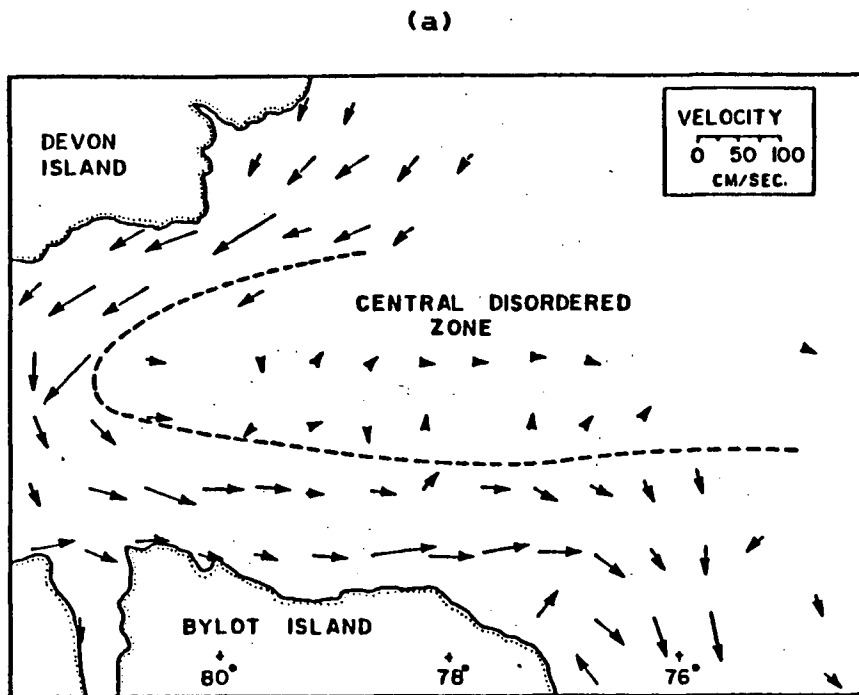


Figure 2. Reentrant circulation in (a) Lancaster Sound (reproduced with permission from Fissel et al., 1982) and (b) Hudson Strait (reproduced with permission from LeBlond et al., 1981), as exhibited by near-surface drogue tracks.

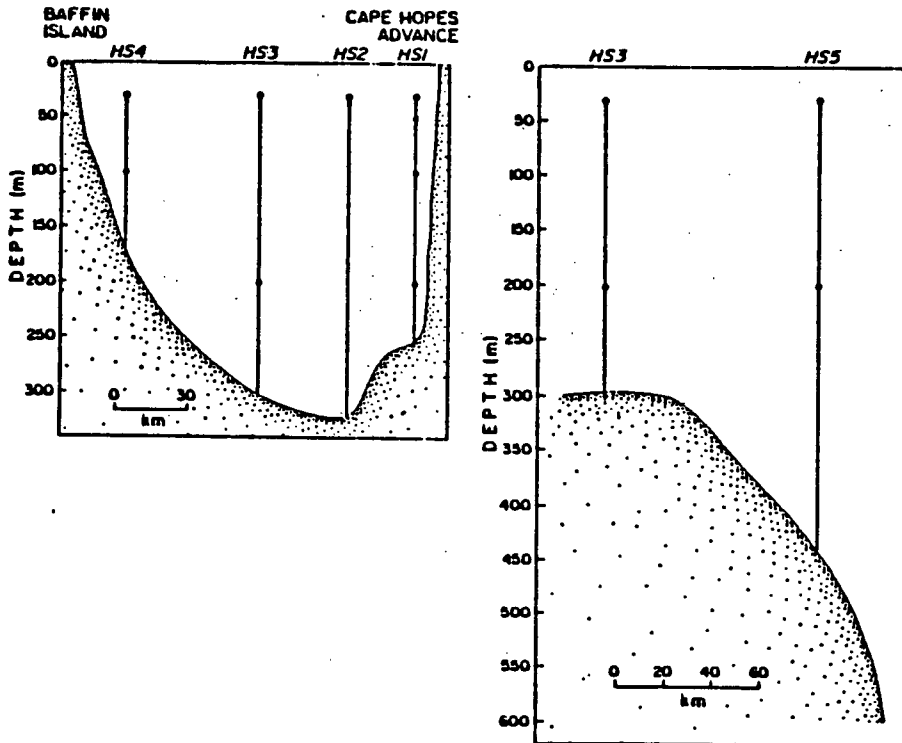
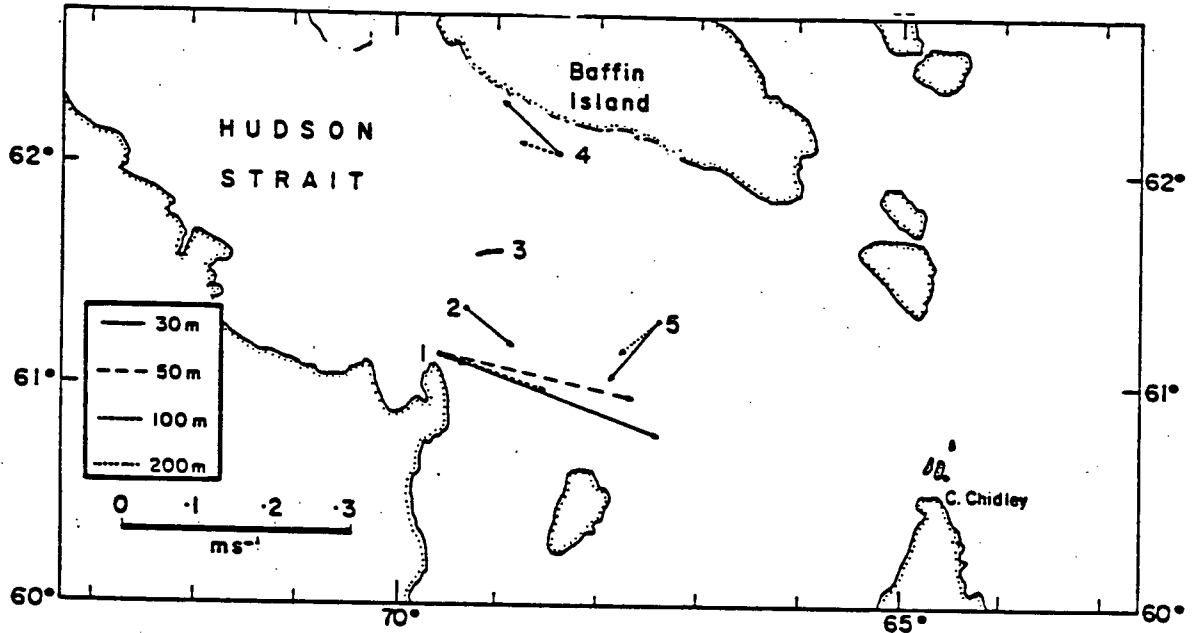


Figure 3a. Upper panel: mean currents in Hudson Strait during Aug. - Oct. 1982. Lower panel: moorings HS1-HS5 profiles (reproduced with permission from Drinkwater, 1985).

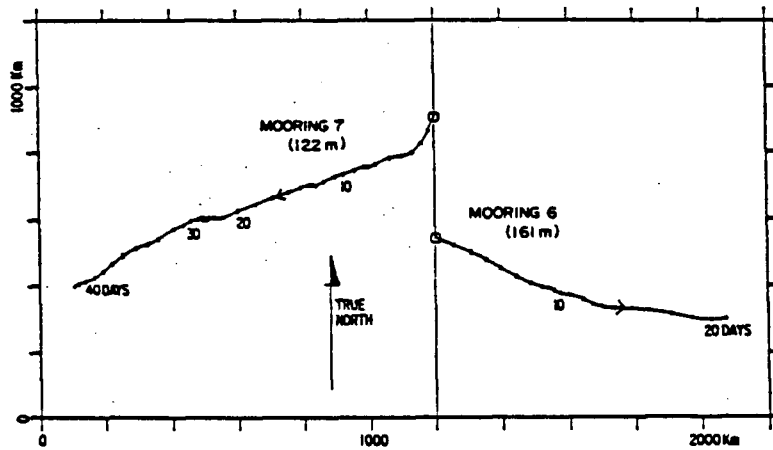
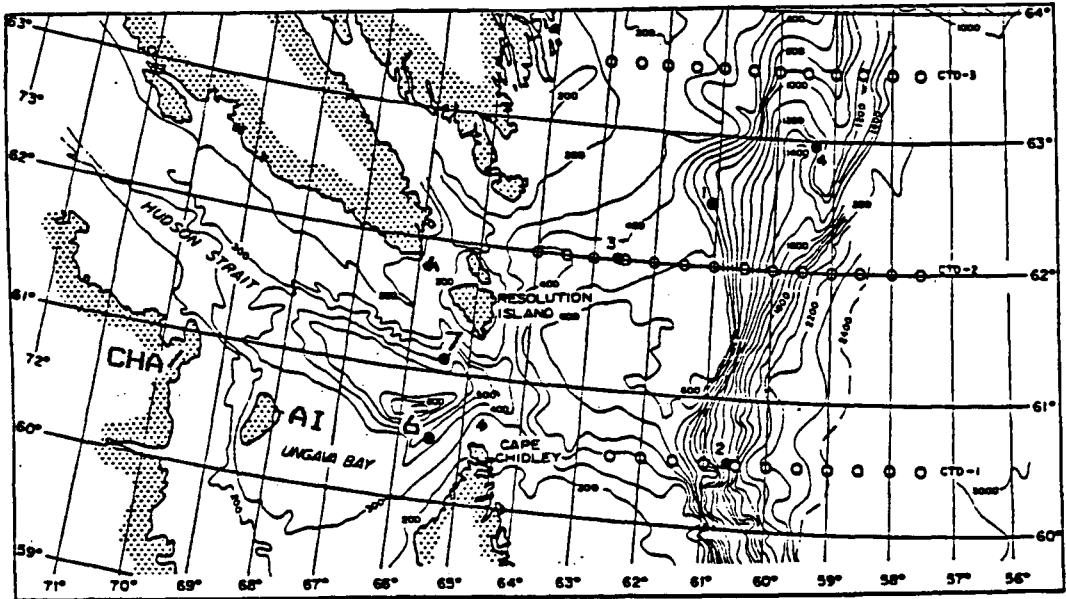


Figure 3b. Lower panel: current trajectories near the mouth of Hudson Strait at moorings 6 and 7, whose location is shown on the map in the upper panel (reproduced with permission from LeBlond et al., 1981; CHA - Cape Hope's Advance, AI - Akpatok Island).

Chapter 2

Models of sea straits

The early theory of water movements through sea straits is given in chapter 5 in Gill (1982). Marsili (1681) used a taut rope to measure currents at various depths in the Strait of Bosphorus. He found that below a certain depth the water moves in opposite direction to the surface currents. He then weighed water samples from the Black Sea and from the Mediterranean and found that the Black Sea water is lighter. From this, he deduced the classical picture of a two-layer estuarine exchange between two seas. Not yet satisfied, he also performed an experiment (figure 4), in which a partition separated the dyed undercurrent water from the lighter surface water. Two holes, one near the top and the other near the bottom, were opened and the resulting flow reproduced the currents in the Bosphorus.

The Strait of Bosphorus is narrow and hence the cross-channel interface slope, resulting from the earth's rotation, is not important. On the other hand, when a channel is wide, the sloping interface eventually meets the surface. The outgoing light water forms a current wedge on the right side (looking downstream), while the incoming denser flow is now mainly concentrated on the opposite side. A good example of a wide channel estuarine exchange is that of Hudson Strait. Figure 5 shows temperature salinity and density (σ_t) sections across the mouth of Hudson Strait (from MacLaren Atlantic, 1977,

reproduced from Osborn et al., 1979). Note that in addition to the light water wedge near the south side (see the sigma-t section on figure 5), there is also a smaller one on the north side.

The theory of water exchange through straits in a rotating frame of reference is quite recent. A seminal and often quoted work is that of Whitehead et al. (1974), who carried out a theoretical and laboratory study of a two-layer rotating channel flow under geostrophic balance. They solved the problem of a) a bottom layer flow and b) two-layered flows in opposite directions over a weir. Since they assumed an infinite bottom depth in the upstream basin, their potential vorticity function was identically zero and the Bernoulli function a constant. These assumptions led to a linear geostrophic velocity profile and parabolic shape for the interface. For small upstream height, they found that the interface intercepts the channel floor at some distance from shore. Because of the assumptions involved (one-dimensional flow, infinite depth upstream), their model is inappropriate for the present study, although it provides a useful guide for understanding the physics of the situation.

Nof (1978a,b), in his studies of outflows from channels into wider basins, expanded the potential vorticity equation and the Bernoulli equation, in powers of the Rossby number $\epsilon = V/2fb$ (where f is the Coriolis parameter, V is the velocity scale and b is the half-width of the channel) for the one-layer case

(1978a), and in powers of the Froude number $F=V^2/g'H$ (where H is the upper layer depth in the channel) in his two-layer model (1978b). The important assumption for the latter case was that $F/\epsilon \ll 1$ (i.e., a narrow channel). He used these expansions to solve the one- and two-layer problems of the geostrophic adjustment in outflows over a step from a channel into a wider basin. He found that the flow separates from the right or from the left (depending on step-up or step-down in the one-layer case and on the length of the channel in his two-layer model) if the Rossby number is smaller than some critical value. Since velocity profiles in the mouth of the channel were prescribed a priori, his solutions are not directly applicable to the present study.

Gill (1977) was the first to obtain analytical solutions for the flow of a homogeneous fluid with a nonzero potential vorticity (i.e., a finite depth upstream) down a rotating channel with a sill and a slowly varying cross-section. He then determined the position of a "control" section, where the long-wave disturbances have a zero phase speed. For certain sill heights and upstream potential vorticity values, he found that a part of the flow is reversed before the sill, i.e., a re-entrant circulation pattern was established (figure 6). Gill's (1977) model is concerned mainly with the hydraulic control of a downchannel flow by a sill and a gradually narrowing profile, which does not include flows around sharp corners and in channel mouths. In some respects, the present work may be complementary

to that of Gill (1977), since his solutions for a slowly varying channel can be matched to (and prescribe the relative transports for) the model of circulation in the mouth of a channel. Roed (1980) performed a similar analysis for the case of a single coastline with a slowly varying curvature and depth profile.

I am aware of only one example of an analytical solution for the flow around a fast changing coastline. Hughes (1981, 1982) has modeled an upper layer flow with separation (and a downstream control by another coastline) around a sharp corner on a low-latitude f -plane; i.e., in the limit of slow rotation. In the present case, I attempt to do the same, but for the case of a mid- to high-latitude f -plane, where the stronger Coriolis force tends to keep the boundary current attached to the coast on its right, even around corners with significant curvatures.

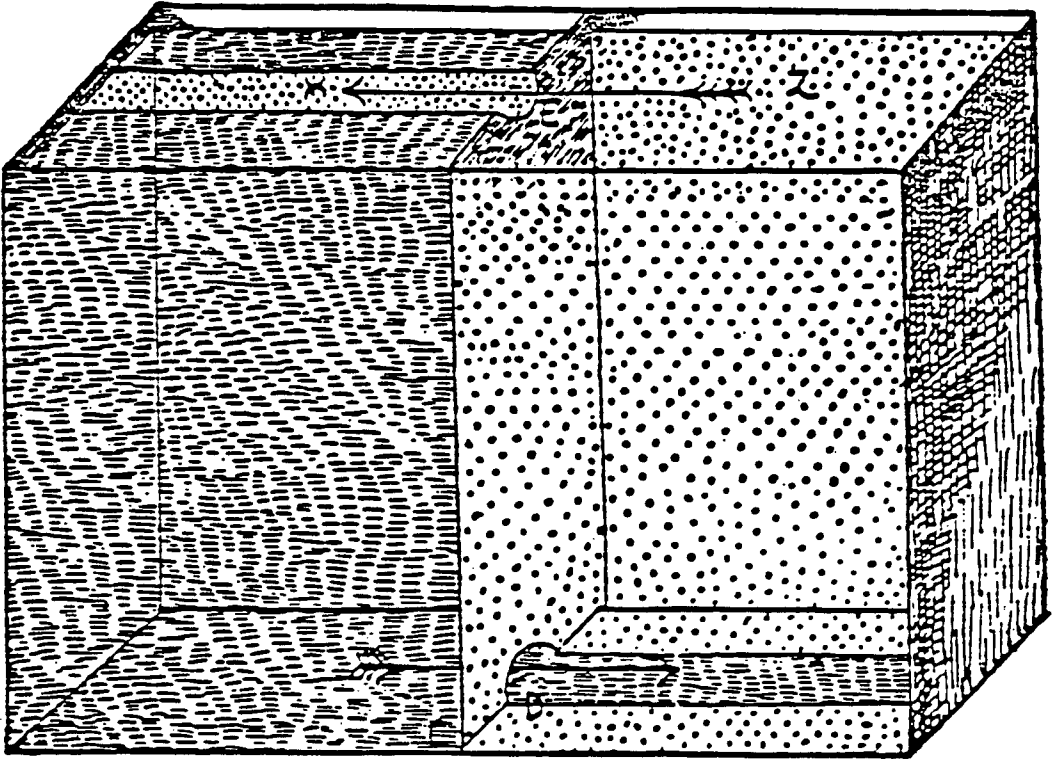


Figure 4. Marsili's (1681) experiment that was designed to model an estuarine-type circulation in the Strait of Bosphorus. (reproduced with permission from Gill, 1982).

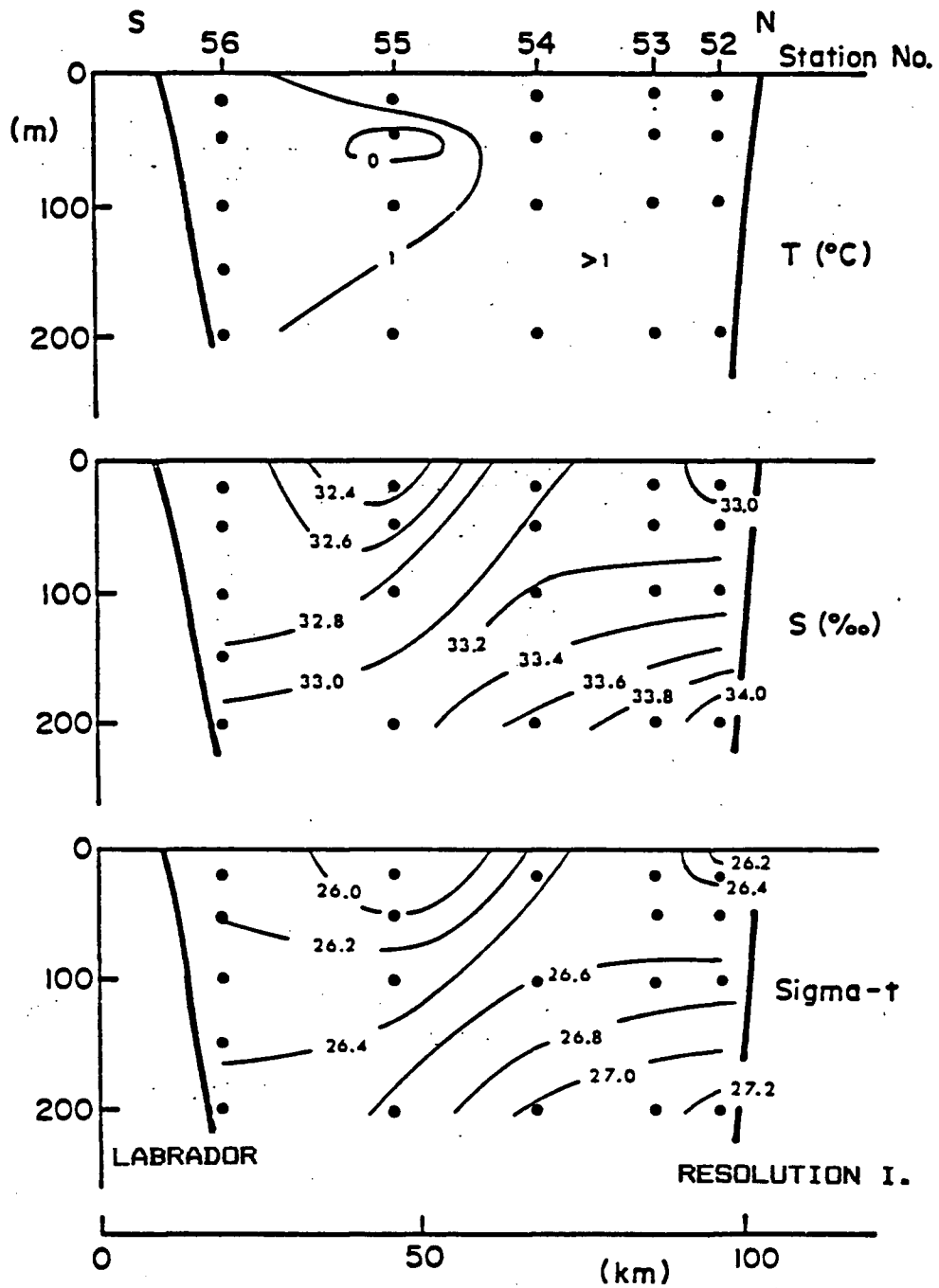


Figure 5. Temperature, salinity and sigma-t section across the mouth of Hudson Strait (from MacLaren Atlantic, 1977, as reproduced in Osborn et al., 1979). See the upper panel in Figure 3b for the location of Resolution Island.

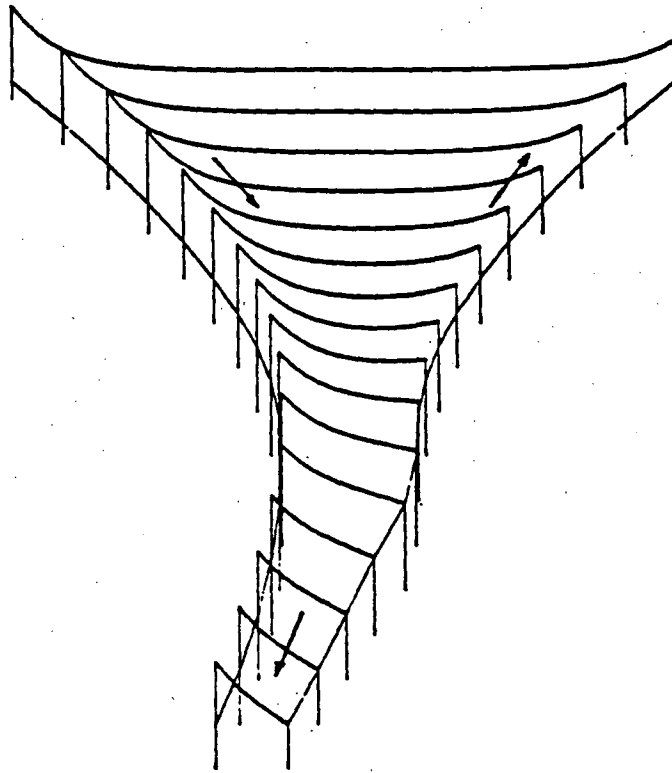


Figure 6. Sample surface configuration (exaggerated scale) from Gill, 1977 (with permission). Downchannel is at the bottom. Note how the surface slopes on opposite sides before the channel narrows, indicating geostrophic flow along directions shown by the arrows.

Chapter 3

Statement of the problem

In this chapter, we present our problem in a general form for an arbitrary domain. More specific examples are given in subsequent chapters. The analysis of steady inviscid coastal flows is based on the conservation principles that govern the motion of an incompressible fluid in a rotating frame of reference. The first two equations express conservation of energy and vorticity. These are the Bernoulli equation

$$(u^2 + v^2)/2 + g'h = G(\Psi), \quad (3.1)$$

(where $g'=(\Delta\rho/\rho)g$ is the reduced gravity) and the potential vorticity equation

$$(v_x - u_y + f)/h = K(\Psi). \quad (3.2)$$

Their derivation can be found in standard textbooks (e.g., Gutman, 1972; Pedlosky, 1979). The transport streamfunction Ψ is related to the depth of the interface h and the horizontal velocity components u and v through

$$hv = \Psi_x \quad \text{and} \quad -hu = \Psi_y. \quad (3.3)$$

The latter two equations follow from the volume conservation

principle for a nondivergent motion

$$(hu)_x + (hv)_y = 0 . \quad (3.4)$$

$G(\Psi)$ and $K(\Psi)=G'(\Psi)$ (Charney, 1955; Gutman, 1972) are functions of integration that are derived from the upstream conditions. This derivation is done in the next chapter for a particular case of an exponential wedge profile. The boundary condition at the coast is specified by assuming it to be a streamline. For example, ^{for} the case of a channel mouth (figure 7), we need to specify the value of Ψ on each boundary. The difference between these two boundary values is the net transport out of (or into) the channel and is determined by conditions far inside the channel. Moreover, if a channel has a slowly varying cross-section and a sill (weir) inside, then Gill's (1977) model can be used to find the net transport. On the other hand, if the channel is wide (and/or the sill is too far inside, as in the case of Lancaster Sound) the net baroclinic transport is a parameter of the problem. This is discussed in detail in Chapter 5, where one-dimensional solutions for a channel are given.

The problem must also be well-posed. This is true as long as the flow does not separate from a boundary. In this inviscid case, the separation may be caused either by adverse pressure gradients or by a flow around a very sharp re-entrant corner. In the latter case, the strong centrifugal force will move the

fluid away from the corner and, according to (3.1), the separation will result from a vanishing upper layer depth. As we shall see in Chapter 7 (and Appendix C), in the case of a right-bounded wedge-type flow, this centrifugal separation occurs only at re-entrant corners that have radii of curvature much smaller than the lateral scale of the flow. When this happens, the problem is not well-posed and the solutions, that are derived below, are no longer valid.

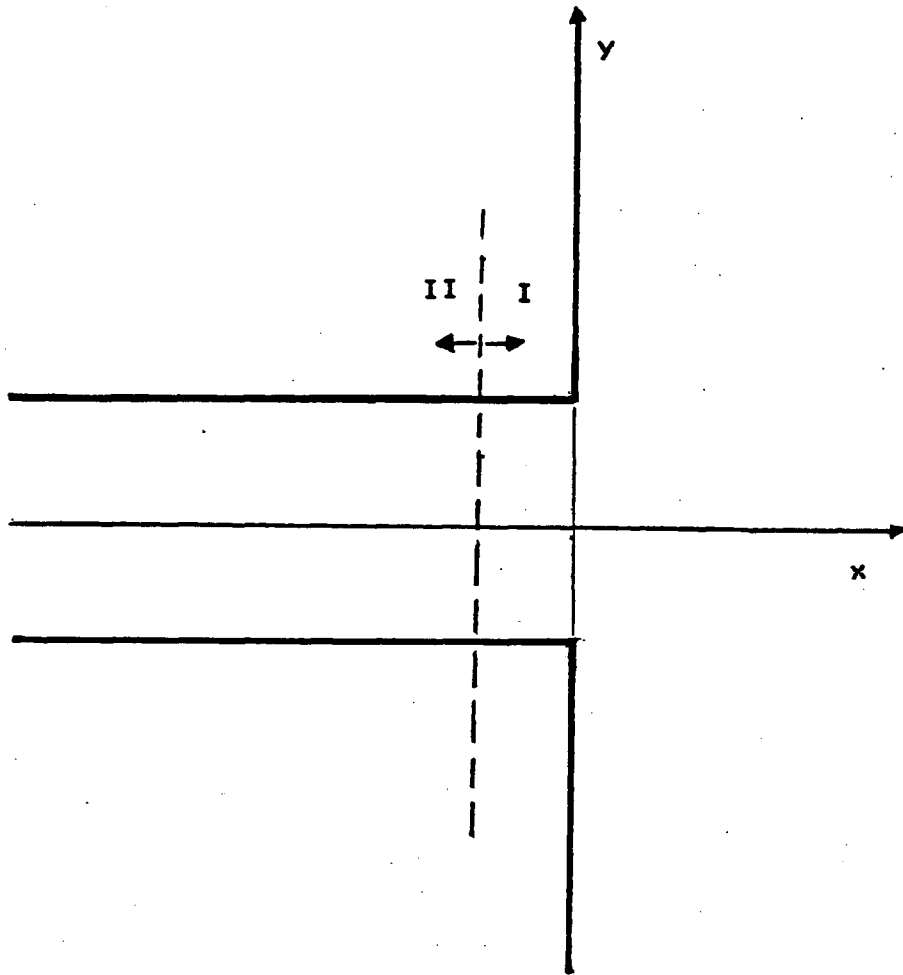


Figure 7 Schematic representation of a channel mouth. It is assumed that the problem of the circulation in the mouth (region I) can be separated from that inside the channel (region II).

Chapter 4

The upstream profile

LeBlond (1980) showed that when a coastal current is in a geostrophic balance with the pressure gradient due to a linearly sloping interface (Figure 8a), then the interface meets the surface (forming a front) at a distance X , given by

$$X = R/F = C^2/fV . \quad (4.1)$$

Here, $R=C/f$ is the Rossby internal deformation radius, $F=V/C$ is the Froude number based on the velocity $C=(g'H)^{1/2}$ of long internal gravity waves, and V and H are, respectively, the flow speed and the upper layer thickness at the coastal boundary. In order to allow for a smooth transition between the coastal current and the offshore region we assume that the interface depth decreases exponentially offshore (therefore eliminating fronts; see Figure 8b) with the same scale X . Letting $k=1/X$, we have

$$h(x) = He^{-kx} . \quad (4.2)$$

If we assume that the velocity is geostrophically balanced, we also have

$$v(x) = g'h_x/f = -Ve^{-kx} , \quad (4.3)$$

where $V=g'H/fX$ ($=FC$) if we use (4.1). When the first equation in (3.3) is integrated with respect to x , we find that the transport streamfunction is given by

$$\Psi(x) = Qe^{-2kx}, \quad (4.4)$$

where the constant of integration was set to zero and $Q=\Psi(0)=VHX/2$. Note that Q is also the total transport in a triangular profile (Figure 8a), which lends support to using X as the horizontal length scale. It is worthwhile to note that for an exponential depth profile, X remains invariant (i.e., it does not change with the distance offshore) if we replace C and F with their local values $c(x)=[g'h(x)]^{1/2}$ and $F(x)=|v(x)|/c(x)$.

In order to see the connection between the decay scale X and the Rossby radius of deformation, used by many authors as a lateral scale for coastal flows (e.g., Nof 1979a,b; Stommel and Luyten, 1984), we consider (for a moment) a current thickness profile that is given by

$$h(x) = D + He^{-kx}, \quad (4.5)$$

where D is some nonzero constant reference depth (Figure 8c). If we now assume a uniform potential vorticity, then, for the one-dimensional case, equation (3.2) becomes

$$(v_x + f)/h = f/D. \quad (4.6)$$

But, $v_x = kV e^{-kx}$ and $kV = F^2 f$, so that from (4.6) we get

$$(f/D)(1 + F^2 e^{-kx}) / (1 + H e^{-kx}/D) = f/D, \quad (4.7)$$

which gives

$$H/D = F^2. \quad (4.8)$$

Thus,

$$X = R/F = (g'D)^{1/2}/f = R_0, \quad (4.9)$$

which means that in this case (when $D \neq 0$), X is the Rossby radius based on the reference depth D . We note that for $F < 1$, $H < D$, so that for a vanishing D (Figure 8b) the uniform potential vorticity equation (4.6) is not applicable, R_0 is meaningless and X as defined by (4.1) is the natural decay scale. By defining a potential depth $H_p = H/F^2$, we get a modified expression, $X = (g'H_p)^{1/2}/f$, so that in a wider sense, we can call X a Rossby deformation radius (based on H_p). The use of the "potential depth" in constant potential vorticity models, though not always so named, is not new (e.g., Stommel, 1965; Flierl, 1979; Gill and Schumann, 1979; Luyten and Stommel, 1984).

We now use (4.2)-(4.4) in the one-dimensional versions

of (3.1) and (3.2) and obtain

$$G(\Psi) = (g'f)^{1/2}(2\Psi)^{1/2} + \epsilon(f/H)\Psi, \quad (4.10)$$

and,

$$K(\Psi) = (g'f)^{1/2}(2\Psi)^{-1/2} + \epsilon(f/H), \quad (4.11)$$

where the Rossby number ϵ is given by

$$\epsilon = F^2 = V^2/(g'H) = V/(fX). \quad (4.12)$$

When these are combined with (3.1) and (3.2) we get a pair of nonlinear equations which, together with (3.3) and appropriate boundary conditions (to be specified later), define the physical problem of inviscid rotational flow along a coast.

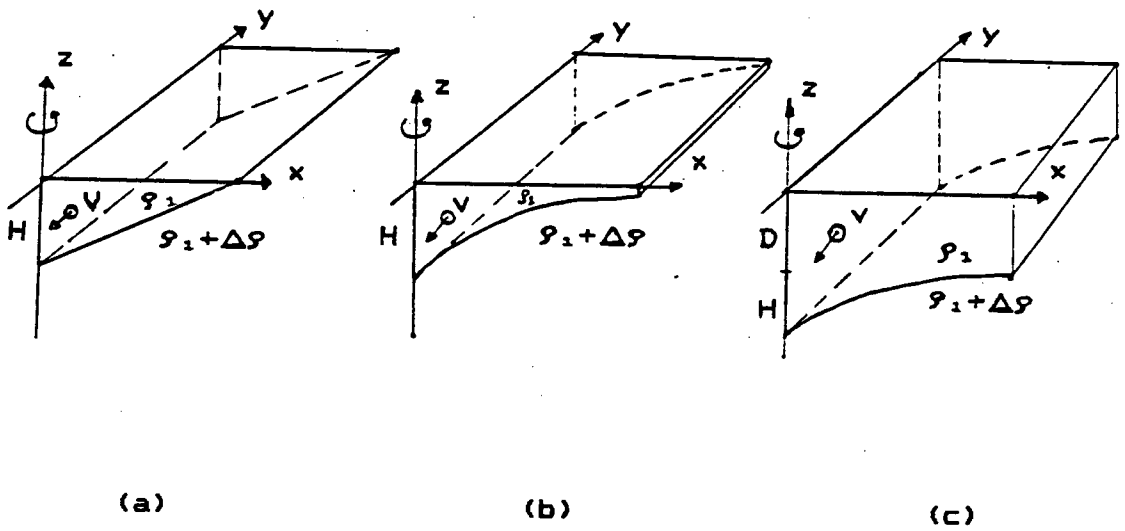


Figure 8. 3 profiles of the upper layer depth: (a) linear $h=H(1-x/X)$, (b) exponential $h=He^{-x/X}$, and (c) exponential $h=D+He^{-x/X}$.

Chapter 5

Solutions inside a channel

For simplicity, let us assume initially that, as shown on Figure 7, the channel is of uniform width $2d$. For strictly along-channel flow, the cross-channel velocity v and all the x -derivatives are zero. Therefore, the momentum equations reduce to the geostrophic relation

$$-fu = g'h_y. \quad (5.1)$$

When combined with (3.3) and integrated once, we find that

$$h^2 = 2f\Psi/g', \quad (5.2)$$

i.e., h is also a streamline. For an exponential upstream profile, (4.11) gives the potential vorticity function in terms of h ,

$$K(h) = f/h + \epsilon f/H. \quad (5.3)$$

When the last equation is substituted into (3.2), we get, after using (5.1), a linear equation for h

$$h_{yy} - k^2h = 0. \quad (5.4)$$

Here, as in Chapter 4, $k=1/X$. The boundary values of h are

$$h(\pm d) = (2fQ_{\pm}/g')^{1/2}, \quad (5.5)$$

where $Q_{\pm}=\Psi(\pm d)$ are the transport streamfunction values on each boundary.

For computational convenience, it was tacitly assumed here that X , and hence also k , in (5.4), are uniform across the channel. This is the situation which corresponds to a uniform stratification. The solution of (5.4) and (5.5) is

$$h(y) = \bar{h}\cosh(ky)/\cosh(kd) - \hat{h}\sinh(ky)/\sinh(kd), \quad (5.6)$$

where,

$$\bar{h} = [h(-d)+h(+d)]/2 \quad \text{and} \quad \hat{h} = [h(-d)-h(+d)]/2. \quad (5.7)$$

Finally, Ψ and u can be calculated using (5.1) and (5.2).

Figures 9a,b show profiles of h for several values of d/X when Q_{\pm} are equal (Figure 9a, the case of zero net transport) and when $Q_{-}=2Q_{+}$ (Figure 9b). For small d/X , the two boundaries influence each other strongly, dictating either a zero flow condition (for $Q_{-}=Q_{+}$) or unidirectional down-channel flow (for $Q_{-}=2Q_{+}$). As d/X increases, the two sides become decoupled, allowing independent existence of coastal currents on each side and, hence the possibility of penetration of flows into the channel at the mouth.

Equation (5.6) is the same as Gill's (1977) (5.2). It may

often be valid to assume that d/X (either d , or X , or both) varies gradually along the axis of the channel, on a scale that is much larger than X . In this case, Figures 9a,b may also be thought of as a view into a channel of a slowly varying relative width d/X , showing the same recirculation across the channel as in Figure 6 (Gill's, 1977, Figure 9e). We note that in contrast to most previous investigations (as in Gill, 1977), we did not assume a uniform potential vorticity. Indeed, even inside the channel, $K(h)$ is not uniform (equation (5.3)). In contrast, the quantity

$$-u_y/h = \epsilon f/H = V/XH, \quad (5.8)$$

is uniform in this one-dimensional case. Note that for an area element $dA=dx dy$, this quantity is the ratio between circulation $dC=-[u(y+dy/2)-u(y-dy/2)]dx=-u_y dA$ and volume $dV=hdA$ of a material vortex tube element.

It is easy to match (join) nonuniform (e.g., narrowing) channel solutions (like the one above, or Gill's, 1977) to a solution around the channel mouth. For example, it can be done (as on Figure 7) one X unit away from the mouth, where, presumably, the corners no longer influence the flow and the streamlines are approximately parallel to the sides of the channel.

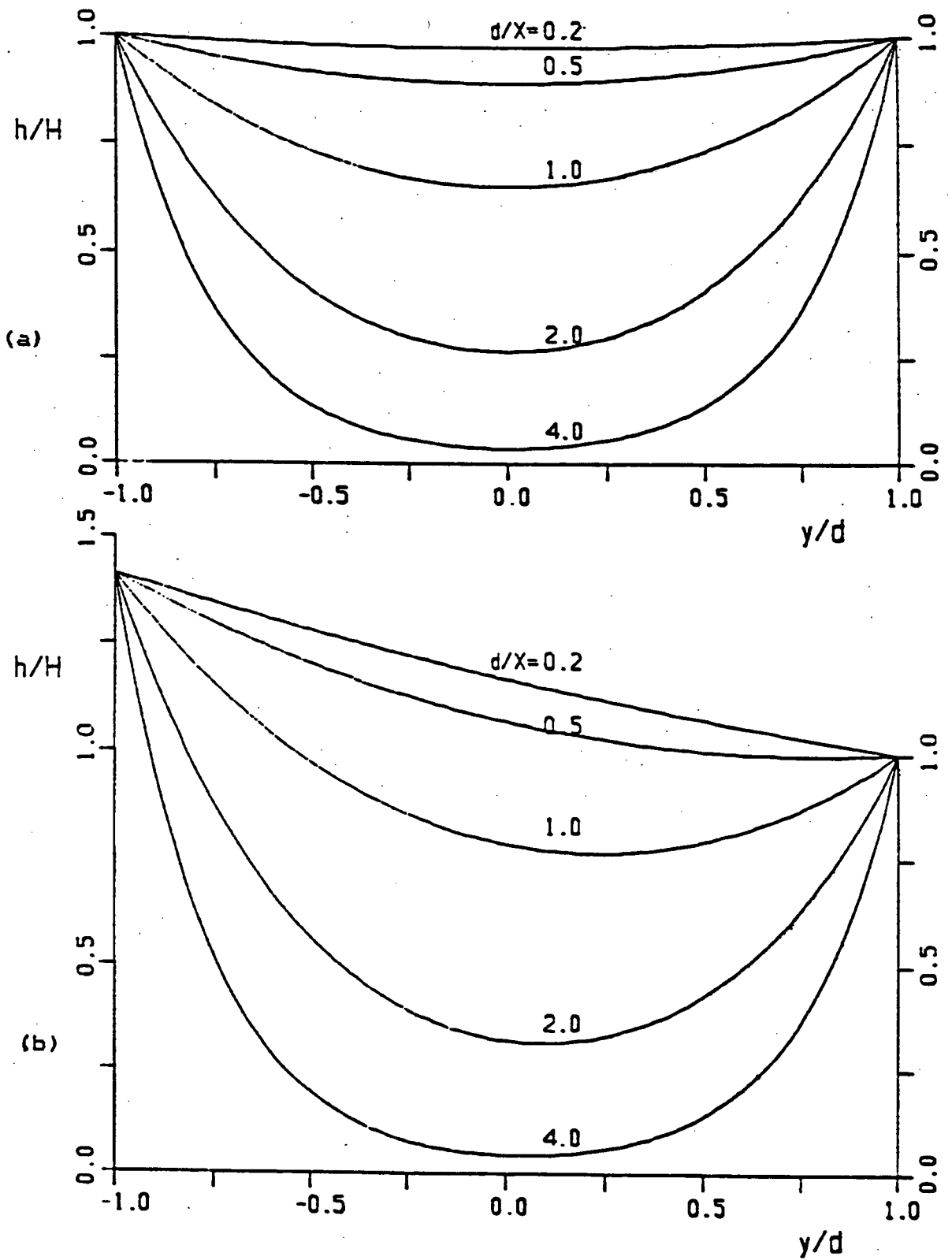


Figure 9. Profiles of h inside a channel for (a) $Q_- = Q_+$ and (b) $Q_- = 2Q_+$, for several values of width, d .

Chapter 6

Scaling and derivation of the governing equations.

It is not possible to tackle directly the set of nonlinear partial differential equations (3.1)-(3.3) in the general two-dimensional case. Instead, we use a regular perturbation expansion in the Rossby number $\epsilon (=F^2)$. First, it is convenient to nondimensionalize the variables according to

$$(x,y)=X(x',y'), \quad (u,v)=V(u',v'), \quad h=Hh', \quad \Psi=Q\Psi', \quad (6.1)$$

where X , V , H and Q are the lateral scale and the upstream boundary values of velocity, interface depth and transport streamfunction, respectively, as defined in Chapter 4.

Substitution into (3.1)-(3.3) gives (after dropping the primes) the nondimensional equations

$$h + (\epsilon/2)(u^2 + v^2) = \Psi^{1/2} + (\epsilon/2)\Psi, \quad (6.2)$$

$$1 + \epsilon(v_x - u_y) = h\Psi^{-1/2} + \epsilon h, \quad (6.3)$$

$$2vh = \Psi_x \quad \text{and} \quad -2uh = \Psi_y. \quad (6.4)$$

We eliminate square roots by changing to a new streamfunction variable s , according to

$$\Psi = s^2. \quad (6.5)$$

As a result, (6.2)-(6.4) become

$$2h + \epsilon(u^2 + v^2) = s(2 + \epsilon s) \quad (6.2')$$

$$s[1 + \epsilon(v_x - u_y)] = h(1 + \epsilon s) \quad (6.3')$$

$$vh = ss_x \quad \text{and} \quad -uh = ss_y. \quad (6.4')$$

We consider s , h , u and v as regular functions of the Rossby number ϵ , expressing them in regular perturbation expansions of the form

$$(s, h, u, v) = \sum_{j=0}^{\infty} \epsilon^j (s_j, h_j, u_j, v_j) \quad (6.6)$$

As a result, we get from (6.2') to orders ϵ^0 , ϵ^1 and ϵ^2 , respectively

$$h_0 = s_0, \quad (6.7a)$$

$$2h_1 + u_0^2 + v_0^2 = 2s_1 + s_0^2, \quad (6.7b)$$

$$h_2 + u_0u_1 + v_0v_1 = s_2 + s_0s_1. \quad (6.7c)$$

From (6.3'), we obtain

$$s_0 = h_0, \quad (6.8a)$$

$$s_1 + s_0(v_{0x} - u_{0y}) = h_1 + h_0s_0, \quad (6.8b)$$

$$s_2 + s_1(v_{0x} - u_{0y}) + s_0(v_{1x} - u_{1y}) = h_2 + h_1s_0 + h_0s_1. \quad (6.8c)$$

Finally, the continuity equations (6.4') yield

$$v_0 h_0 = s_0 s_{0x}, \quad -u_0 h_0 = s_0 s_{0y}, \quad (6.9a)$$

$$v_0 h_1 + v_1 h_0 = (s_0 s_1)_x, \quad -u_0 h_1 - u_1 h_0 = (s_0 s_1)_y. \quad (6.9b)$$

We can now use these equations to get a single equation for the $O(1)$ streamfunction variable s_0 and another one for the $O(\epsilon)$ contribution s_1 . From either (6.7a) or (6.8a), we have

$$h_0 = s_0, \quad (6.10)$$

which shows that the $O(1)$ interface depth is a streamline. As a result, from (6.9a), we obtain the $O(1)$ velocities,

$$v_0 = s_{0x} \quad \text{and,} \quad -u_0 = s_{0y}, \quad (6.11)$$

so that, at least to this order, the flow is geostrophic. Consequently, we also get the $O(1)$ relative vorticity

$$v_{0x} - u_{0y} = \nabla^2 s_0 \quad (6.12)$$

and, the $O(1)$ kinetic energy

$$U_0 = (u_0^2 + v_0^2)/2 = (\nabla s_0)^2/2. \quad (6.13)$$

From (6.7b) it follows that the $O(\epsilon)$ layer depth is

related to s_1 via

$$h_1 = s_1 + [s_0^2 - (\nabla s_0)^2]/2, \quad (6.14)$$

while, from (6.8b), we find

$$h_1 = s_1 + s_0(\nabla^2 s_0 - s_0). \quad (6.15)$$

We combine the last two equations to obtain the differential equation for s_0 :

$$\nabla^2 s_0 - s_0 = [s_0^2 - (\nabla s_0)^2]/2s_0. \quad (6.16)$$

Even to this leading order, the equation is nonlinear. This nonlinearity can be traced back to the nonuniformity of the potential vorticity, which is a consequence of (4.2). From (6.14), we see that the right hand side of (6.16), which looks like the departure of the $O(1)$ kinetic energy from its value upstream (divided by the depth h_0 , see equations (6.2) and (6.7b)), is also the $O(\epsilon)$ departure of the depth h from the streamline s (as given in (6.14)), and this difference contributes to the balance between the relative vorticity term, $\nabla^2 s_0$, and the vortex stretching term s_0 ($=h_0$). As we shall see in the next section, the right hand side of (6.16) vanishes whenever the motion is rectilinear, which is the case upstream or far away from boundaries. In particular, upstream, where $h=s$

identically, $h_1=s_1=0$ and hence, the relative vorticity is equal to s and the kinetic energy is equal to $s^2/2$ (which can be verified directly from the exponential profile). Following the same method, it is not difficult to show that in the case of a *uniform* potential vorticity function $K(\Psi)$, the right-hand side of (6.16) vanishes and hence, the $O(1)$ equation for s_0 is linear.

The derivation of the equation for s_1 is given in appendix A. The result is

$$s_0 \nabla^2 s_1 + \nabla s_0 \cdot \nabla s_1 + (\nabla^2 s_0 - \mathfrak{J} s_0) s_1 = W, \quad (6.17)$$

where (see appendix A)

$$W = [s_0^2 - (\nabla s_0)^2]^2 / 4s_0 + s_0^3 - 1/2 (\nabla s_0 \cdot \nabla) (\nabla s_0)^2. \quad (6.18)$$

The function W can be rewritten more concisely as

$$W = s_0 (M^2 + s_0^2) - (\nabla s_0 \cdot \nabla) U_0, \quad (6.19)$$

where $M = s_0/2 - U_0/s_0$ is the right-hand side of (6.16) and U_0 is the $O(1)$ kinetic energy, given by (6.13). It can be shown that far from the apex, in regions of rectilinear flow, W vanishes identically, together with M . The question of singularity near the apex of a re-entrant corner is considered in the next chapter, where explicit solutions are derived.

We can linearize (6.16) and simplify the left side of

(6.17) if we use transformations

$$s_0 = p^{2/3} \tag{6.20}$$

and,

$$s_1 = p^{-1/3}q . \tag{6.21}$$

This results in two modified Helmholtz equations, a homogeneous one for p :

$$\nabla^2 p - (3/2)^2 p = 0 ; \tag{6.22}$$

and an inhomogeneous one for q :

$$\nabla^2 q - (3/2)^2 q = p^{-1/3}W . \tag{6.23}$$

Also, since $s^2 = \psi = \psi_0 + \epsilon \psi_1 + \dots$, we get

$$\psi_0 = p^{4/3} \quad \text{and} \quad \psi_1 = 2p^{1/3}q. \tag{6.24}$$

Equations (6.20)-(6.24) define the physical problem if the shape of the domain and the boundary conditions are specified. In the next chapter, we solve these equations for a domain bounded by two straight walls, i.e., a wedge of an arbitrary angle π/a , where the angular parameter a is not smaller than $1/2$. We will then obtain, in Chapter 8, approximate solutions for flows along coastlines, which can be represented by a (possibly discontinuous)

combination of corners, as long as no two corners are closer than one Rossby radius.

Chapter 7

Rotating flow around a sharp bend

We proceed now to solve the problem, stated in the previous chapter, for the case of a domain bounded by two straight walls, which are located at $\theta=0$ and $\theta=\pi/a$, with $a>1/2$ (Figure 10). As stated previously, we assume that a geostrophic current with an exponential depth profile, given by (4.2), approaches the bend from upstream, with the $\theta=\pi/a$ boundary on its right. We also assume that, unless it should appear explicitly from the solution of the problem, there is no separation of streamlines from the bounding wall. Consequently, the current turns the bend, even for a re-entrant corner, and the far downstream depth profile is identical to that far upstream of the corner.

The equations to be solved are (6.22) and (6.23), and the corresponding boundary conditions are

$$p = 1 \quad \text{at } \theta = 0, \pi/a \quad (7.1)$$

and

$$q = 0 \quad \text{at } \theta = 0, \pi/a. \quad (7.2)$$

We begin with the first set.

The $O(1)$ solution

Before we start, it should be pointed out that equations (6.22) and (7.1) are closely connected with the problem of diffraction of a Kelvin wave by a wedge. The latter was solved by Roseau (1967) and also by Packham and Williams (1968) for a general wedge angle using a complex integral representation. Buchwald (1968) used the Wiener-Hopf technique to solve the diffraction problem for the particular case of a Kelvin wave incident at a right-angled corner. In principle, the solution of our problem should be obtainable from the latter by a limiting process, wherein the Kelvin wave transforms into a geostrophic current with an exponential profile, in the limit of zero frequency. Unfortunately, due to its complexity, only asymptotic forms of the wave solution were presented in the above papers.

The methods employed by Roseau and by Packham and Williams are related to the "Sommerfeld diffraction problem", which deals with the diffraction of electromagnetic waves by a conducting wedge. Sommerfeld (1896) solved this problem for the case of a half-screen (wedge of an angle 2π) and for an angle which is a submultiple of $2n\pi$, where n is a positive integer (for an illuminating discussion, the reader is referred to Sommerfeld's book "Optics", 1954, section 38). His method was generalized to an arbitrary angle by Macdonald (1915), Bromwich (1915), Whipple (1916) and Carslaw (1919). Some of the extensive literature on the subject has been reviewed by Oberhettinger (1954).

Since we intend to use the results of diffraction theory, we briefly review its formulation. We need consider only the special case of a plane wave of unit strength, $F_0 = \exp\{ik[ct + r\cos(\theta - \theta_0)]\}$, incident from the direction θ_0 at a right angle to an edge of the wedge. After removal of the time dependence, the Sommerfeld diffraction problem reduces to solving the Helmholtz equation,

$$\nabla^2 V + k^2 V = 0, \quad (7.3)$$

subject to conditions that the solution V is zero on each boundary and that it satisfies a suitable radiation condition.

Bromwich (1915) used the case of the wedge π/n , where n is a positive integer, as a starting point of the familiar method of images. He replaced the sum of the images by a complex integral and then extended his formulae to hold for any (real and positive) value of $n=a$. Subsequently, by deforming the integration path, Whipple (1916) was able to show that the solution can be written as

$$V = \text{"sum of visible images"} - \\ - F(\pi + \theta - \theta_0) - F(\pi - \theta + \theta_0) + F(\pi - \theta - \theta_0) + F(\pi + \theta + \theta_0), \quad (7.4)$$

where the diffraction terms F are given by

$$F(\psi) = \frac{a \sin(a\psi)}{2\pi} \int_0^{\infty} \frac{\exp(-ikrcoshu) du}{\cosh(au) - \cos(a\psi)}, \quad (7.5)$$

integrated along the positive u-axis. The "visible images" are the incident wave F_0 and its images that are "visible" at (r, θ) . Whipple also showed that each diffracted term $F(\psi)$ satisfies equation (7.3).

In order to solve the boundary value problem, defined by (6.22) and (7.1), we change k to ik ($k=3/2$ in equation (6.22)) and describe the incoming current as an evanescent plane "wave" emanating from the boundary at $\theta=\pi/a$. Thus, the "wave source" is presumed to "radiate" from the direction $\theta_0=\pi/a+\pi/2$ (Figure 10), in which case

$$F_0 = \exp[krcos(\theta-\theta_0)] = \exp[krsin(\theta-\pi/a)], \quad (7.6)$$

As a result, the diffracted term (7.5) becomes (see Whipple, 1916, for details)

$$\begin{aligned} F(\psi) &= \frac{a \sin(a\psi)}{2\pi} \int_0^{\infty} \frac{\exp(ikrsinhu) du}{\cosh(au) - \cos(a\psi)} = \\ &= \frac{\sin(a\psi)}{4\pi} \int_0^{\infty} \frac{\exp[ikrsinh(u/a)] du}{\sinh^2(u/2) + \sin^2(a\psi/2)}. \end{aligned} \quad (7.7a,b)$$

Due to the difference in boundary conditions ($p=1$, while $V=0$ on both boundaries), we cannot use (7.4) directly, but must seek an alternate combination of the F terms. We investigate

first the functional behaviour of $F(\psi)$, which may be summarized as follows (Figures 11a,b):

- i) $F(\psi)$ is continuous for $0 < \psi < 2\pi/a$ and has a period of $2\pi/a$,
- ii) $F(\psi) \rightarrow 0$ as $\psi \rightarrow \pi/a$, and
- iii) $F(\psi) \rightarrow 1/2$ as $\psi \rightarrow +0$ and $F(\psi) \rightarrow -1/2$ as $\psi \rightarrow -0$.

Properties i) and ii) are readily seen by inspecting (7.7a). Property iii) means that F has a jump discontinuity at $\psi=0$. This is because as $\psi \rightarrow 0$, $\sin(a\psi)$ multiplied by the integral has a finite limit there, while the sin function changes its sign. Indeed, if we put $b = \sin(a\psi/2)$, then, as $b \rightarrow 0$, most of the contribution to the integral comes from the vicinity of $u=0$, in which case $\sinh u \approx u$, $\sinh(au/2) \approx au/2$. The real part of (7.7b) gives, for $b \neq 0$ (since $\sin(a\psi) = 2\sin(a\psi/2)\cos(a\psi/2) \approx 2b$ there),

$$F(b) \approx \frac{ab}{2\pi} \int_0^{\infty} \frac{\cos(kru) du}{(au/2)^2 + b^2} .$$

Changing to $x=au/2$, $du=2dx/a$, we get

$$F(b) \approx \frac{b}{\pi} \int_0^{\infty} \frac{\cos(2krx/a) dx}{x^2 + b^2} = \frac{b}{2|b|} \exp(-2kr|b|/a). \quad (7.8)$$

Hence, for small ψ

$$2F(\psi) \approx \text{sign}(\psi) \exp(-kr|\psi|) \rightarrow \text{sign}(\psi), \quad \text{as } \psi \rightarrow 0.$$

From the above properties of $F(\psi)$, it follows that the solution of the boundary value problem (6.22) and (7.1) is given by the sum of the four diffraction terms

$$p(r, \theta) = 2F(\theta) + 2F(\pi/a - \theta),$$

or, explicitly,

$$\begin{aligned} p &= \frac{2a \sin(a\theta)}{\pi} \int_0^{\infty} \frac{\exp(ikr \sinh u) \cosh(au) du}{\cosh^2(au) - \cos^2(a\theta)} = \\ &= \frac{2 \sin(a\theta)}{\pi} \int_0^{\infty} \frac{\exp[ikr \sinh(u/a)] \cosh u du}{\sinh^2 u + \sin^2(a\theta)}. \end{aligned} \quad (7.9a,b)$$

Since each F term satisfies (6.22) (with $k=3/2$), then so does p . One can also show this directly by taking derivatives of p with respect to r and θ and substituting back into (6.22). While trying this out, it is useful to know that the value of the integral in (7.9b) does not change when its upper limit is replaced by $\infty + id$, with the only condition that $0 < d < a\pi$. This is needed since when differentiated with respect to r , (7.9b) gives an apparently divergent integral, that can be transformed into a convergent one by integration by parts, and the integrated terms vanish when the upper limit has this extra $+id$ (analogous to artificial viscosity, which is often used as a convenient way to

get convergence at infinity; see, for example, Carrier et al., 1966, p. 337).

It is also a simple exercise to show that for the particular case of a straight coastline, $a=1$, (7.9) reduces to the upstream profile $p=e^{-kx}$, where x is the normal distance to the boundary and $k=3/2$ (hence, $s_0=e^{-x}$). For $a \neq 1$, a numerical quadrature can be used to evaluate (7.9), or (7.7). The term $2F(\pi/a-\theta)$ can be thought of as representing a linear rotating flow from the upstream into a sink at the apex of the corner. Similarly, $2F(\theta)$ would be a source flow from the apex. Their sum, raised to the power $2/3$, according to (6.20), gives s_0 , the $O(1)$ streamfunction, which is plotted on Figure 12a for $a=2/3$ (most of the Figures are drawn for this choice of a). s_h , the solution to the homogeneous counterpart of (6.16), is also shown on this Figure. The difference between the two is very small, <0.03 . This means that M , the nonlinear forcing term on the right hand side of (6.16), plotted on Figure 12b, has a small effect on the $O(1)$ solution (it moves the streamlines somewhat away from the corner). As expected, for large r , s_0 reduces to the upstream profile e^{-x} , where x is the distance from either boundary, while for small r , it is given by the potential flow streamfunction p_p , raised to the power $2/3$. This is shown in more detail in Appendix B. We should add that while looking at Figures 12a,b and the figures that follow, we must remember that, since the distances are in units of $X=R/F$, the actual dimensions of these drawings are inversely proportional to $F=e^{1/2}$.

The $Q(\epsilon)$ solution

We now proceed to solve the second boundary value problem, equations (6.23) and (7.2). Formally, the solution may be written as

$$q(x,y) = \iint f(x',y')G(x,y|x',y')dx'dy', \quad (7.10)$$

where the integration is over the specified domain, f is the right hand side of (6.23),

$$f = p^{-1/3}W, \quad (7.11)$$

and W is given by (6.19). The Green's function $G(x,y|x',y')$ satisfies

$$\nabla^2 G - k^2 G = \delta(x-x')\delta(y-y') \quad (7.12)$$

and vanishes on the boundary. It can be written in terms of the modified Bessel functions (see, for example, Stakgold, 1968),

$$G(r,\theta|r',\theta') = -\frac{2a}{\pi} \sum_{n=1}^{\infty} \sin(na\theta)\sin(na\theta')K_{n\alpha}(kr_>)I_{n\alpha}(kr_<), \quad (7.13)$$

with $r_> = \max(r,r')$ and $r_< = \min(r,r')$. Due to the symmetry of the wedge problem, only the odd terms in (7.13) contribute to the integral in (7.10). We will also be satisfied with approximating

the $O(\epsilon)$ term q . Calculations show that even if only the leading term in (7.13),

$$G \approx -(2a/\pi) \sin(a\theta) \sin(a\theta') K_0(kr_>) I_0(kr_<), \quad (7.14)$$

is retained, the value of q is increased by no more than a few percent. We compute (7.10) using a simple quadrature routine. Figures 13a,b show contours of the function f and of $s_1 = s_0^{-1/2} q$, respectively. Somewhat surprisingly, the maximum value of s_1 is less than 0.2, and as a result, no separation is evident in the streamlines of $\Psi = s_0^2 + 2\epsilon s_0 s_1$, which are shown on Figure 13c for $\epsilon = 0.5$. While this value of ϵ may seem to be somewhat large (for (6.6) to be valid), it is, nevertheless, used here for demonstration purposes. The only noticeable effect of the $O(\epsilon)$ term on the transport streamfunction Ψ is to move the streamlines away from the corner (Figure 13d), an effect which may be attributed to the centrifugal acceleration of the fluid. A word of caution: since we nondimensionalized distances with $X = R/\epsilon^{1/2}$, we cannot compare dimensional velocities for the two values of $\epsilon = 0$ and 0.5 on the basis of streamline separations only (Figure 13d). In fact, since $\epsilon \rightarrow 0$ implies $X \rightarrow \infty$, statements concerning the $\epsilon = 0$ case can only be interpreted in this limiting sense.

Using (6.14), we calculate the $O(\epsilon)$ depth,

$$h_1 = s_1 + Ms_0, \quad (7.15)$$

and, from (6.9b) and (7.15), we obtain the $O(\epsilon)$ velocities,

$$u_1 = -s_{1y} - Mu_0 \quad (7.15a)$$

and

$$v_1 = s_{1x} - Mv_0. \quad (7.15b)$$

Contours of h_1 are plotted on Figure 14a, while Figures 14b and 14c show the total depth of the interface $h=h_0+\epsilon h_1$. The depth integrated kinetic energy

$$hU = h[U_0 + \epsilon(u_0u_1+v_0v_1)]$$

is shown in Figures 15a,b for the two values of $\epsilon=0$ and $\epsilon=0.5$. Figure 14c shows the effect of the nonlinear advection terms: a *centrifugal upwelling* for a re-entrant ($a<1$) corner. In contrast, downwelling would be expected at an inside ($a>1$) corner. It is also apparent that for large ϵ and/or large corner curvature, we may expect a surfacing of the pycnocline; i.e., separation of the streamlines from the boundary just before or at the corner. This is only vaguely discernible on Figure 13c. Due to the assumed power series form, equation (6.6), there is little confidence in the above derived solution (see below) that close to the corner, where the $O(\epsilon)$ terms are larger than the $O(1)$ term (next section). This is especially true for re-entrant corners. A separate calculation, which was done for smaller scales (see Appendix C), shows a separation of streamlines very

close to the apex. The question of the validity of the solution is examined below, while separation is discussed in the end of the chapter.

The validity of the solution

For a re-entrant corner of infinite curvature, the solution is not valid at the apex, where the velocities u and v are infinite. We must also require that each of the four series in (6.6) converge to a finite limit. We cannot prove convergence of (6.6), but ask, as an approximate requirement, that the $O(\epsilon)$ terms be of the same order of magnitude, or smaller, than the $O(1)$ terms. To be more definite, we require that

$$|s_1| < s_0, \quad (7.16a)$$

$$|h_1| < h_0 = s_0, \quad (7.16b)$$

and $|U_1| < U_0, \quad (7.16c)$

where $U_1 = u_0 u_1 + v_0 v_1$ is the $O(\epsilon)$ kinetic energy term. Using (7.15) and (6.11), the last inequality may also be written as

$$|\nabla s_0 \cdot \nabla s_1 - 2MU_0| < U_0. \quad (7.17)$$

Figures 12a and 13b show that (7.16a) is satisfied everywhere. Forming the ratios

$$r_1 = |h_1/h_0| = |M + s_1/s_0| \quad (7.18)$$

and

$$r_2 = |2M - \nabla s_0 \cdot \nabla s_1 / U_0|, \quad (7.19)$$

we plot contours of r_1 and r_2 on Figures 16a,b, superimposed upon a few streamlines Ψ (for $\epsilon=0.5$). We notice that for the chosen parameters ($a=2/3$, $\epsilon=0.5$), our solution is valid (r_1 and r_2 both less than 1) for streamlines $\Psi < 0.9$.

Figures 16a,b show that, depending on ϵ , the solution is valid for relatively (but, not infinitely) sharp re-entrant corners, as long as the rounded boundary (e.g., the $\Psi=0.9$) streamline does not penetrate far inside the curve $r_1=1$.

Supercritical flow

Since for a re-entrant corner the velocity of the fluid is high near the apex, we expect the flow to be supercritical there. The local Froude number,

$$F_r = F[(u^2 + v^2)/h]^{1/2}, \quad (7.20)$$

is contoured together with Ψ on Figure 16c. For the chosen parameters ($\epsilon=F^2=0.5$, $a=2/3$), half of the total transport is passing through the supercritical region, where $F_r > 1$. This means that disturbances generated downstream of the corner cannot propagate upstream, which may cause a hydraulic jump near the

second (downstream) $F_r=1$ line. In our case, the conditions downstream are determined by the upstream parameters since, in the absence of another boundary close-by, the Kelvin wave can propagate only with the boundary on its right. Hence, (for this steady model) no hydraulic jumps are expected as the flow re-enters the subcritical regime.

It should be pointed out, however, that while no stationary jumps are predicted at a corner, travelling disturbances in a form of shock-waves or bores are quite likely. These may arise, for example, when there is a sudden change in upstream conditions (like an increase in transport), in which case a fully nonlinear shock-wave will be generated. According to Nof (1984), this shock would then propagate downstream (along a strait vertical boundary) at a speed larger than that of a Kelvin wave associated with both the disturbed and the undisturbed flow. Because the shock is faster than the sum of the downstream (with respect to the shock) advection speed and the downstream Kelvin wave speed but slower than the corresponding sum upstream of the shock, no energy is lost from the shock (except for small frictional losses) and the shock retains its form (Nof, 1984). It is not clear however, how such shock is transformed when it rounds a sharp corner. As in the case of monochromatic Kelvin waves (Packham and Williams, 1968; Buchwald, 1968; Miles, 1972), one may expect that a certain amount of diffracted energy loss (Poincare waves) will occur in its higher (superinertial) frequency components. Thus, the

shock-wave downstream of the corner will be less energetic and, possibly, of a different shape than when it was upstream of the corner.

Separation

The power series expansion (6.6) is not valid very close to the apex. We rewrite (6.2')-(6.4'):

$$h + \epsilon w^2/2 = s + \epsilon s^2/2, \quad (7.21)$$

$$1 - \epsilon(w_n + w/r) = h/s + \epsilon h, \quad (7.22)$$

$$-wh = \epsilon s s_n, \quad (7.23)$$

where $w=(u^2+v^2)^{1/2}$ is the speed, r is the radius of curvature of a streamline and the subscript n denotes a normal derivative. We now consider a boundary streamline, $s=1$, and assume r_c to be the radius of curvature that causes its separation. Upon separation, $h=0$, from (7.21), the speed $w=(1+2/\epsilon)^{1/2}$ is constant, and from (7.22) the relative and the planetary vorticities are equal,

$$\epsilon(w_n + w/r_c) = 1. \quad (7.24)$$

Differentiating (7.21) in the normal direction, and substituting into (7.24) yields the momentum equation,

$$-h_n + \epsilon w^2/r_c = w, \quad (7.25)$$

which states that the balance between the pressure gradient and the centrifugal force is held by the Coriolis force. Equation (7.25) is satisfied for any, however small, r_c (with a correspondingly steeper interface slope h_n). Hence, our model does not give us the critical separation curvature. We can get some idea about the size of the upwelling region and, hence, about the critical radius r_c , if we solve the same problem (equations (6.2')-(6.4')) but for smaller scales, of the order of $\epsilon^2 X$, near the apex. This is done in Appendix C. The results of these calculations show that, for example, for $\epsilon=0.5$ and $a=2/3$, $r_c < 0.02$, and the centrifugal upwelling is not important if the radius of curvature of the rounded corner is larger than about $0.1X$. It may be of some interest to match the two solutions (e.g., using the method of multiple scales). But this would take us beyond the scope of this work and also may be of little consequence, since all of the coastal radii of curvature considered here (as, in the mouth of Hudson Strait) are larger than $0.1X$.

In this respect, we would like to point out that the centrifugal upwelling at a sharp cape, and the resulting doughnut-like shape of the interface (Figure 14c), are exactly analogous to (hypothetical, since no one has ever observed them) anomalous warm eddies with a cold core, which have surfaced, for example, as a possible solution in Flierl's (1979) analytical two-layer model of the structure of warm and cold core rings.

The balance of forces is the same -- geostrophy on the outside and a cyclostrophic balance on the inside. Figure 13 in Flierl (1979) shows a straight line relation between the strength of the ring, as it was defined by Flierl: $\epsilon_r = -(2\epsilon + \epsilon^2)^{1/2}$, and its inside radius r_0 . Although this line stops short of the $r_0=0$ axis (presumably due to the singularity of his governing equation), it does seem to indicate that for $\epsilon_r > -1.5$ ($\epsilon < 0.8$), the inner (cold) core of the ring disappears. In that case, the smaller centrifugal force is no longer sufficient to hold the inner slope for the upwelling to take place, and the ring stops being anomalous. Despite the differences, Flierl's constant potential vorticity (and, hence, deeper upper layer; see Chapter 4) radially symmetrical model seems to indicate that the horizontal extent of a centrifugal upwelling around a sharp re-entrant corner should be rather small for ϵ values that are consistent (e.g., $\epsilon < 1/2$) with the power series expansion (6.6). This agrees well with our results, and in particular with Figure 14c (drawn for the $a=2/3$, $\epsilon=1/2$ case).

Because of its limited extent, the centrifugal upwelling is not the most likely cause of separation of the boundary streamline. Other effects may be more important. For example, if there is an adverse pressure gradient which raises the depth of the upper layer to its maximum value, $1+\epsilon/2$, then, from (7.21), we get a stagnation point, where $w=0$, and hence, separation. This pressure gradient could be due to changes in buoyancy, wind forcing, or due to barotropic effects (e.g., changes in

bathymetry). In addition, enhanced Ekman pumping (due to higher velocities at the corner) may contribute to upwelling and, hence, to separation. Consequently, a three-dimensional frictional model may be required to answer this question about the separation at a sharp cape. Merkin and Solan (1979) have shown that in the case of a uniform stream ($V_c = \text{constant}$) of depth H past a circular cylinder of diameter D and for a small Rossby number, $Ro = V_c / fD \ll 1$ (i.e., large D , or small V_c), the flow separates at some point on the cylinder, $\theta < \pi$, if the ratio $(E_v/2)^{1/2} / Ro = (\nu f)^{1/2} D / (2H V_c) < 1$, where E_v is the vertical Ekman number and ν is the eddy viscosity. For $\epsilon \sim 1/2$, the condition $Ro \ll 1$ is equivalent to $X/D \ll 1$. Although this suggests that Merkin and Solan's (1979) results are not applicable to strong flows around sharp corners, an analogous approach may prove fruitful.

While the problem of separation remains to be solved, let us assume for the sake of argument that the flow does separate. This results in an anticyclonic baroclinic jet that would impinge on the straight coastline (downstream of the corner) at some nonzero angle. But, since the speed on the free streamline ($\Psi = 1$, $h = 0$ for the inviscid model) is finite, it cannot pass through a stagnation point and, hence, it must turn right, away from the boundary (Figure 17a). A transient adjustment process follows, whereby part of the flow pours into a closed gyre, while a different streamline, $\Psi < 1$, passes through a stagnation point. As the size and the depth of the gyre increase, higher valued

streamlines move through the stagnation point. An equilibrium is reached, when the depth of the separated streamline attains its maximum value, $h=1+\epsilon/2$, which allows it to pass through the stagnation point (Figure 17b). In this context, the work of Whitehead (1985) on the deflection of a baroclinic jet by a wall becomes relevant. His results indicate that upon impingement the flow bifurcates with a larger part turning to the right, in support of the above description of the adjustment process. The final size of the gyre may be a function of the wedge angle, the Rossby number, and the interfacial friction. This rather qualitative description is based on the assumption that the Bernoulli function and the potential vorticity on each streamline remain invariant during the adjustment process. This assumption may not be entirely true. If generation of some type of gravity or second class waves accompanies the process, then the energy and the final size of the gyre will be affected. It should be emphasized that after separation, the free streamline could turn away from the boundary (i.e., to the left), in which case there will be no reattachment. Therefore, until an explicit solution is found, this paragraph should be regarded as a hypothesis that may guide future study. In addition, comparison should be made with solutions of an equivalent nonrotating ($f=0$) problem.

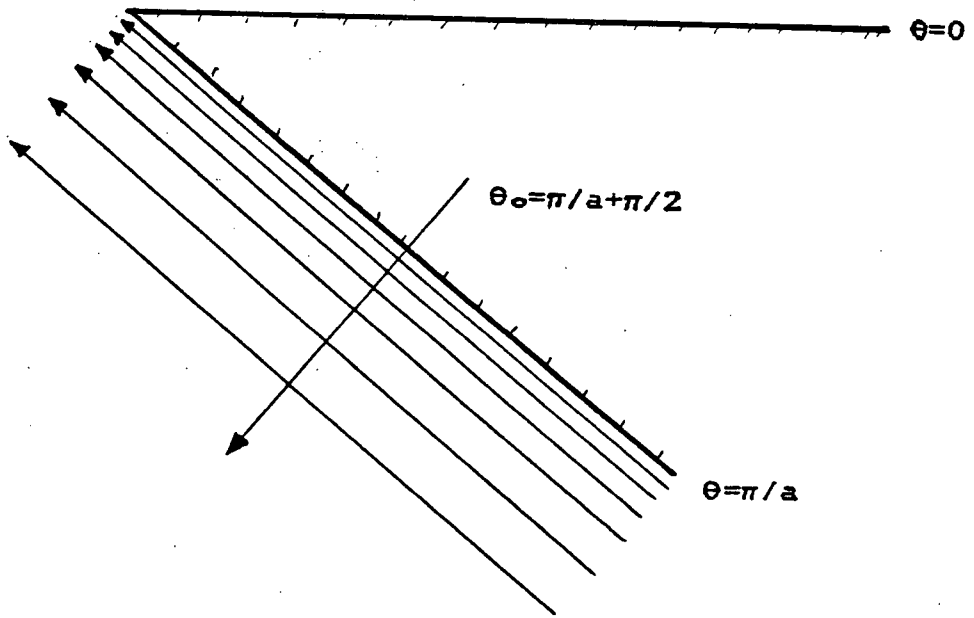


Figure 10. The incoming current profile as an evanescent "wave" emanating from the boundary along $\theta=\pi/a$.

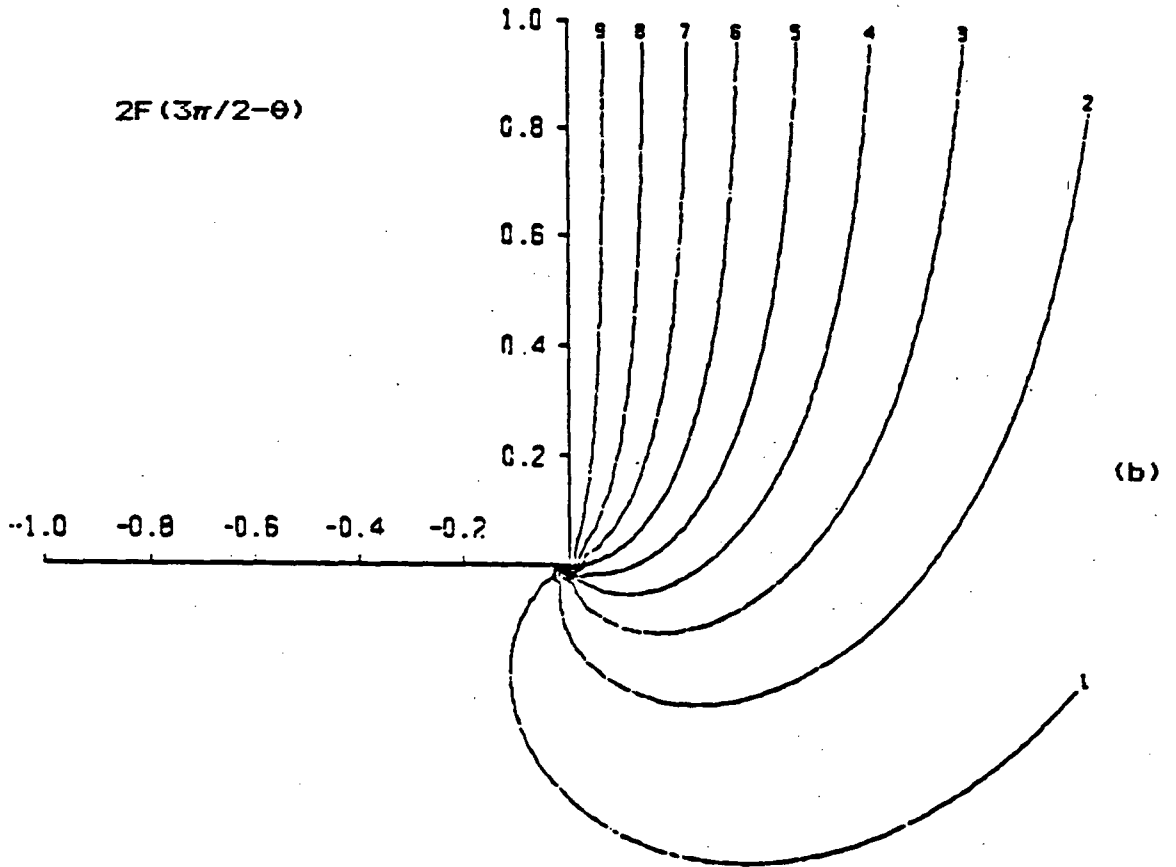
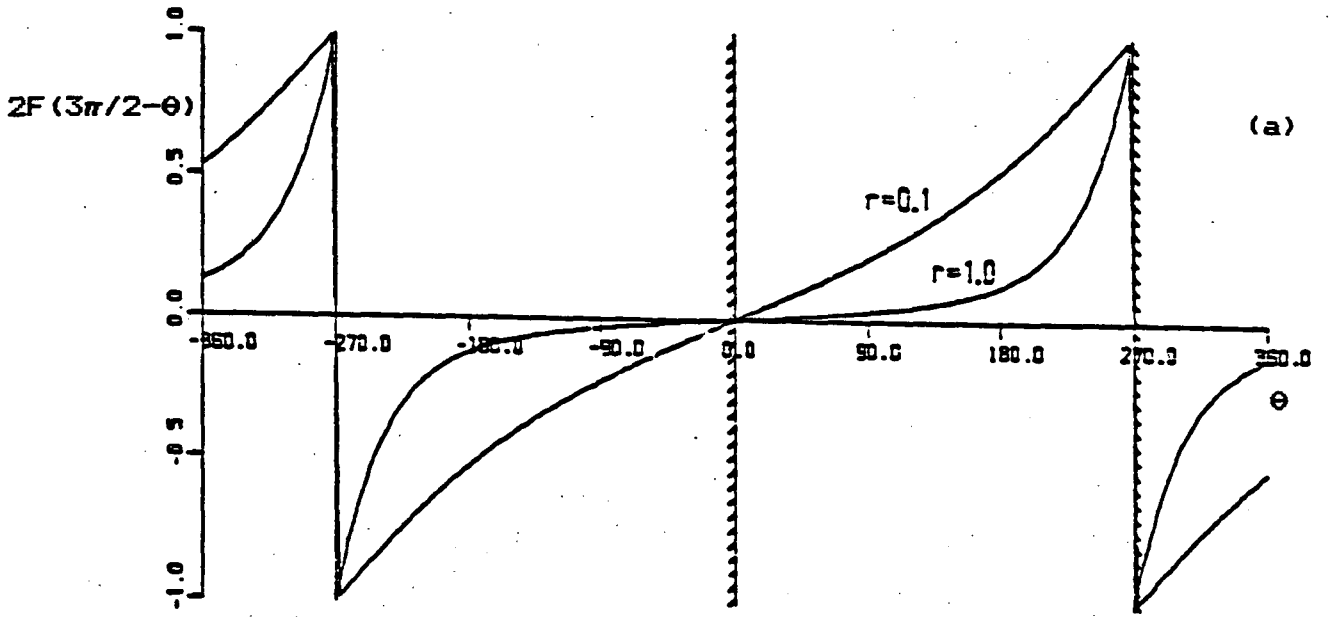


Figure 11. Diffraction term $2F(\psi)$, with $\psi = \pi/a - \theta$ and $a = 2/3$:
 (a) its functional behaviour in the range $-2\pi < \theta < 2\pi$
 for $r = 0.1$ and $r = 1.0$; (b) as a rotating sink of a
 unit strength. The domain is $2X \times 2X$ large and contour
 spacing is 0.1. Unless noted otherwise, the same
 applies to subsequent contour plots.

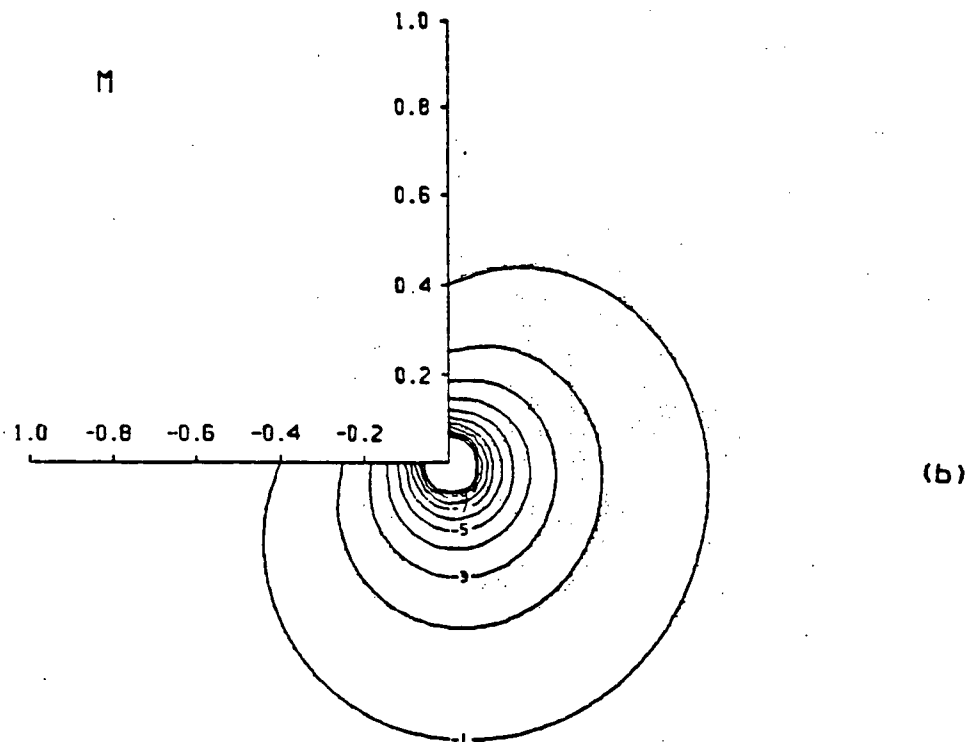
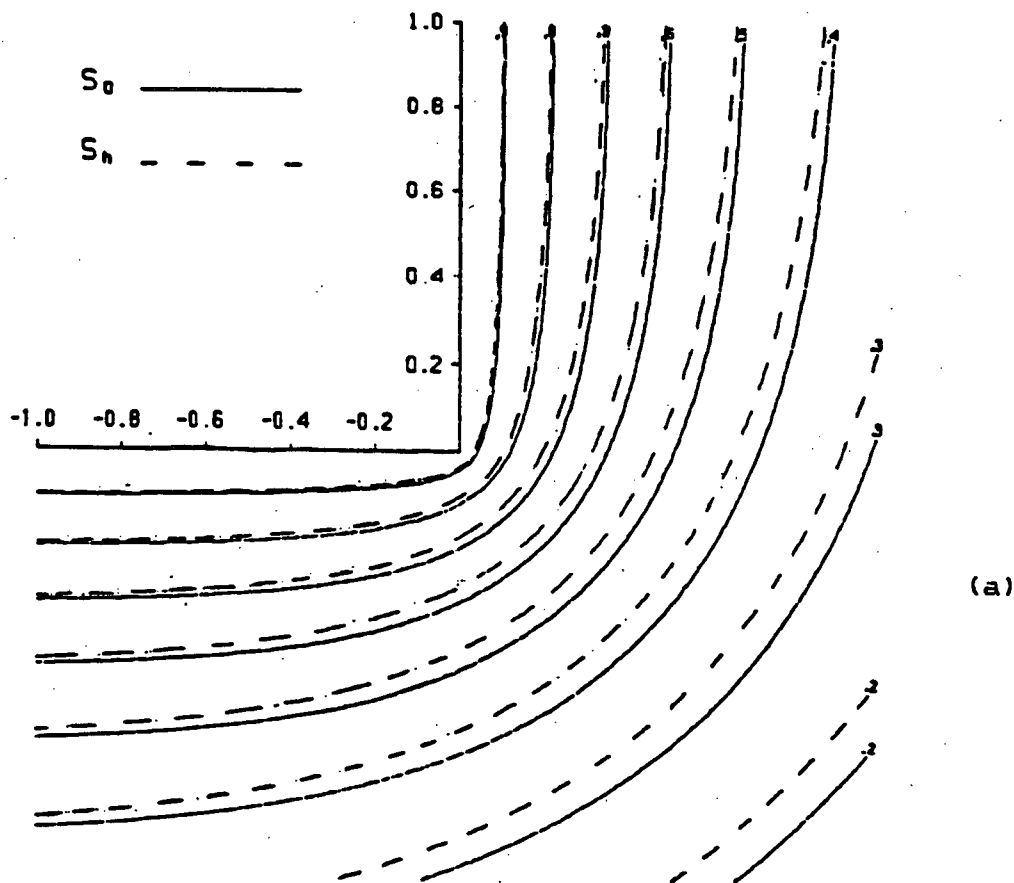


Figure 12. (a) The $O(1)$ streamfunction $s_0=p^{2/3}$ (continuous contours) and its homogeneous counterpart s_h (dashed contours); s_h is the solution of $\nabla^2 s_h - s_h = 0$. (b) Contours of $M=[s_0^2 - (\nabla s_0)^2]/2s_0$.

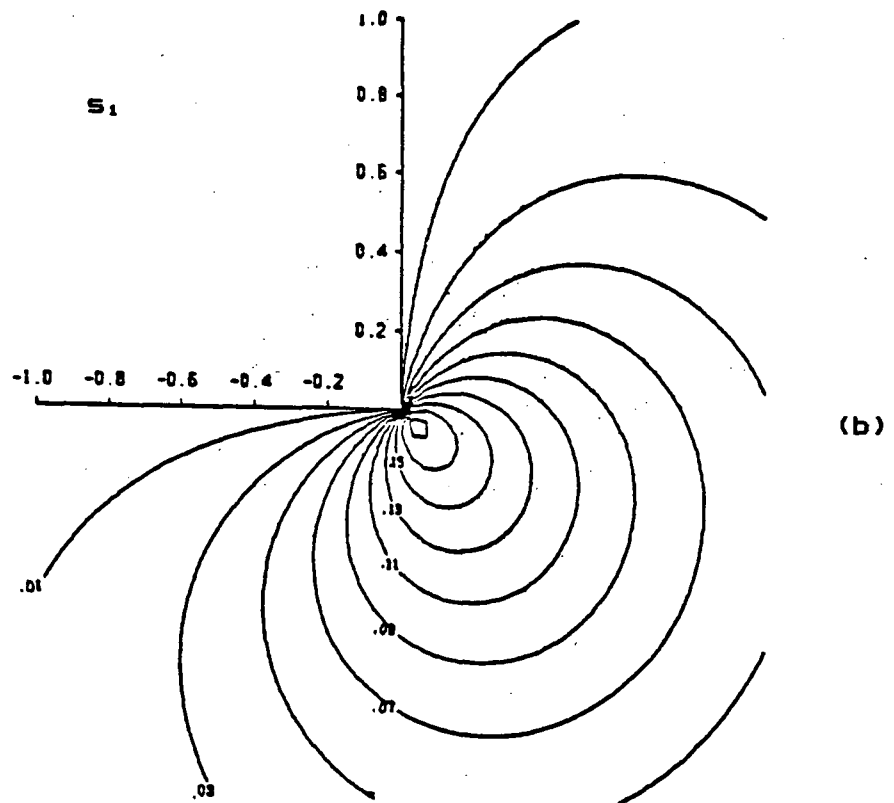
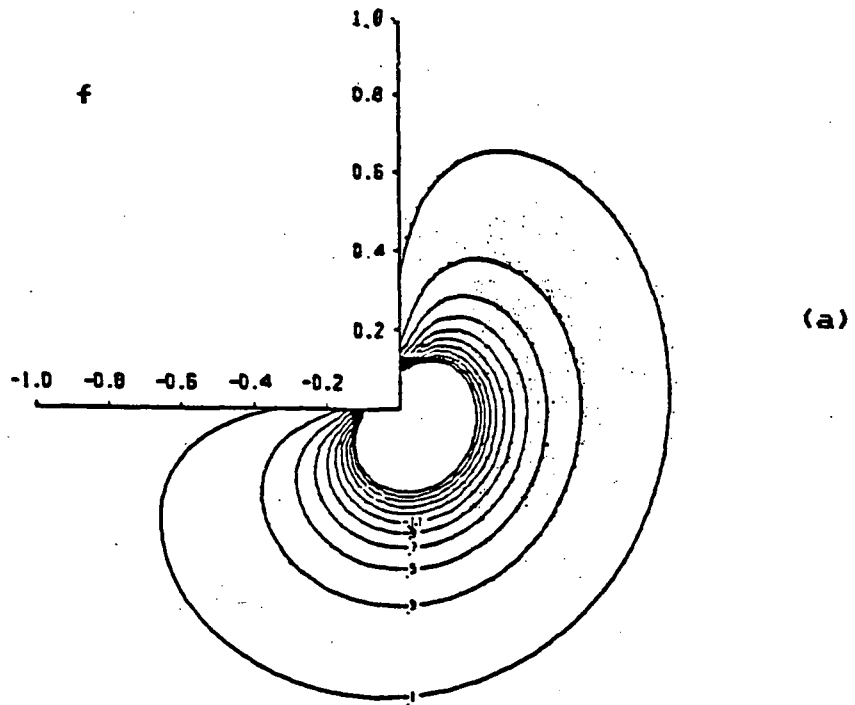
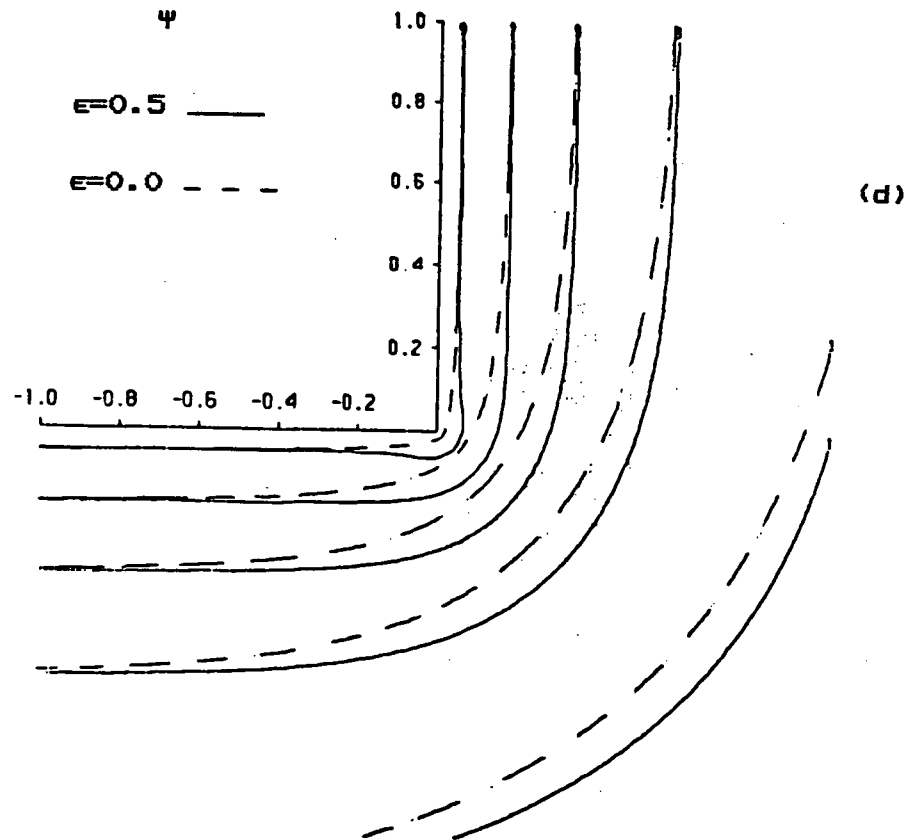
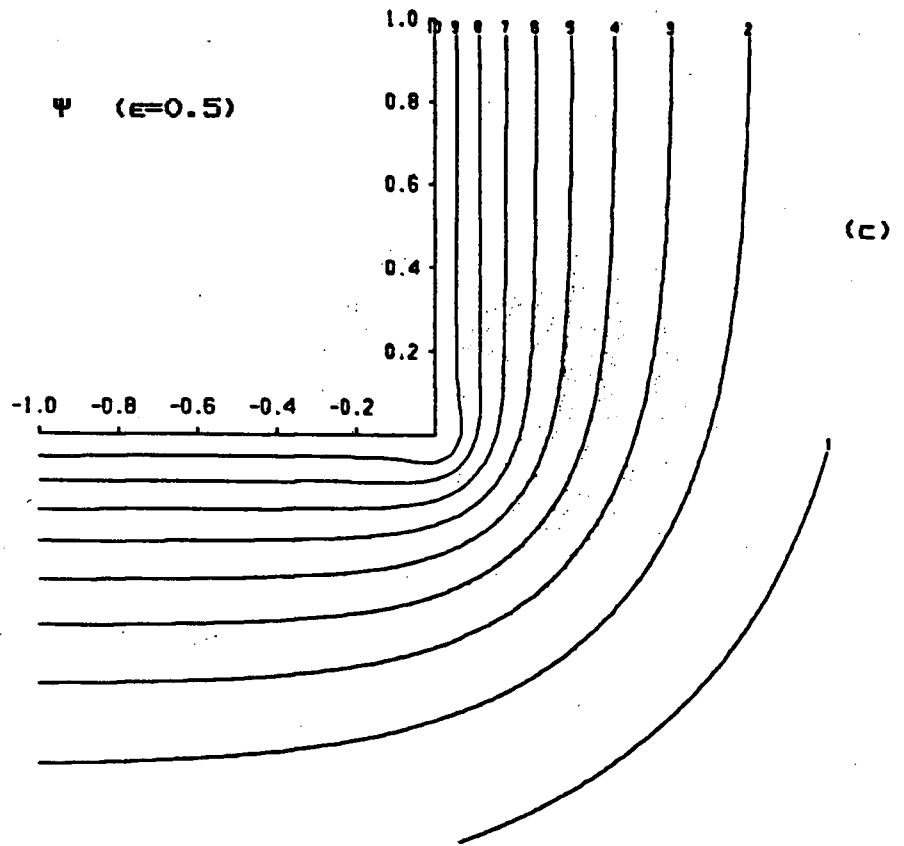


Figure 13. (a) The right hand side of (6.23), $f=p^{-1/3}W$. (b) The $O(\epsilon)$ streamfunction variable s_1 . Here, contour spacing is 0.02. (c) The total transport streamfunction $\Psi=\Psi_0+\epsilon\Psi_1$, for $\epsilon=0.5$. (d) Comparison between Ψ_0 ($\epsilon=0$) and Ψ ($\epsilon=0.5$).



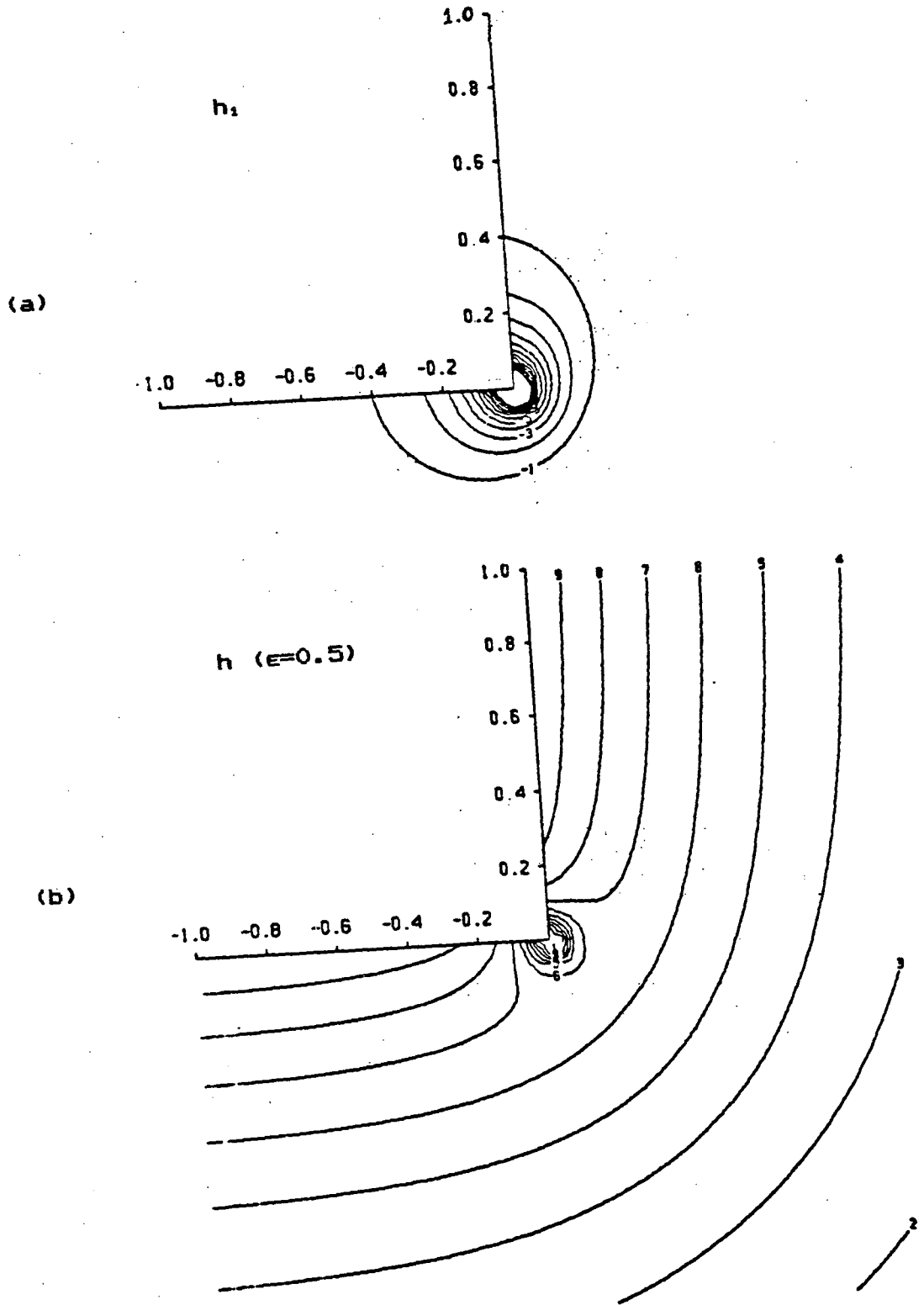
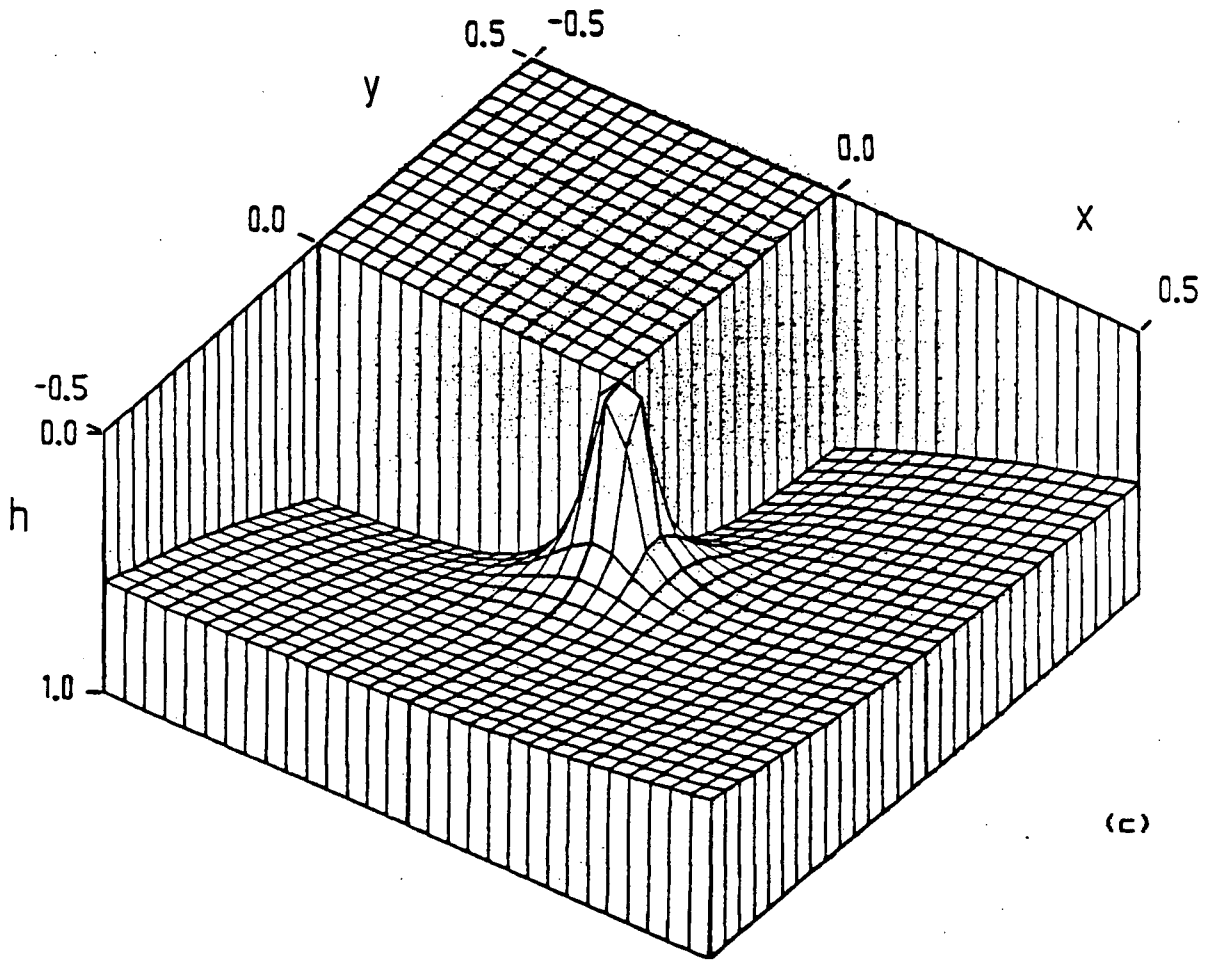


Figure 14. (a) The $O(\epsilon)$ depth variable h_1 . (b) Contours and (c) 3-dimensional view of the depth of the interface $h = h_0 + \epsilon h_1$ (for $\epsilon = 0.5$).



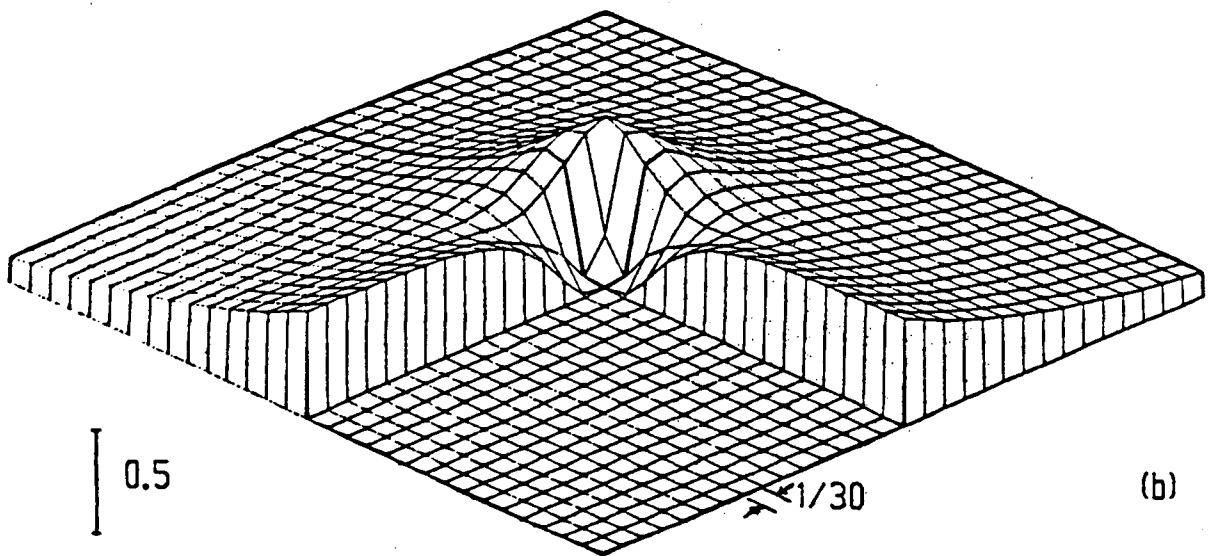
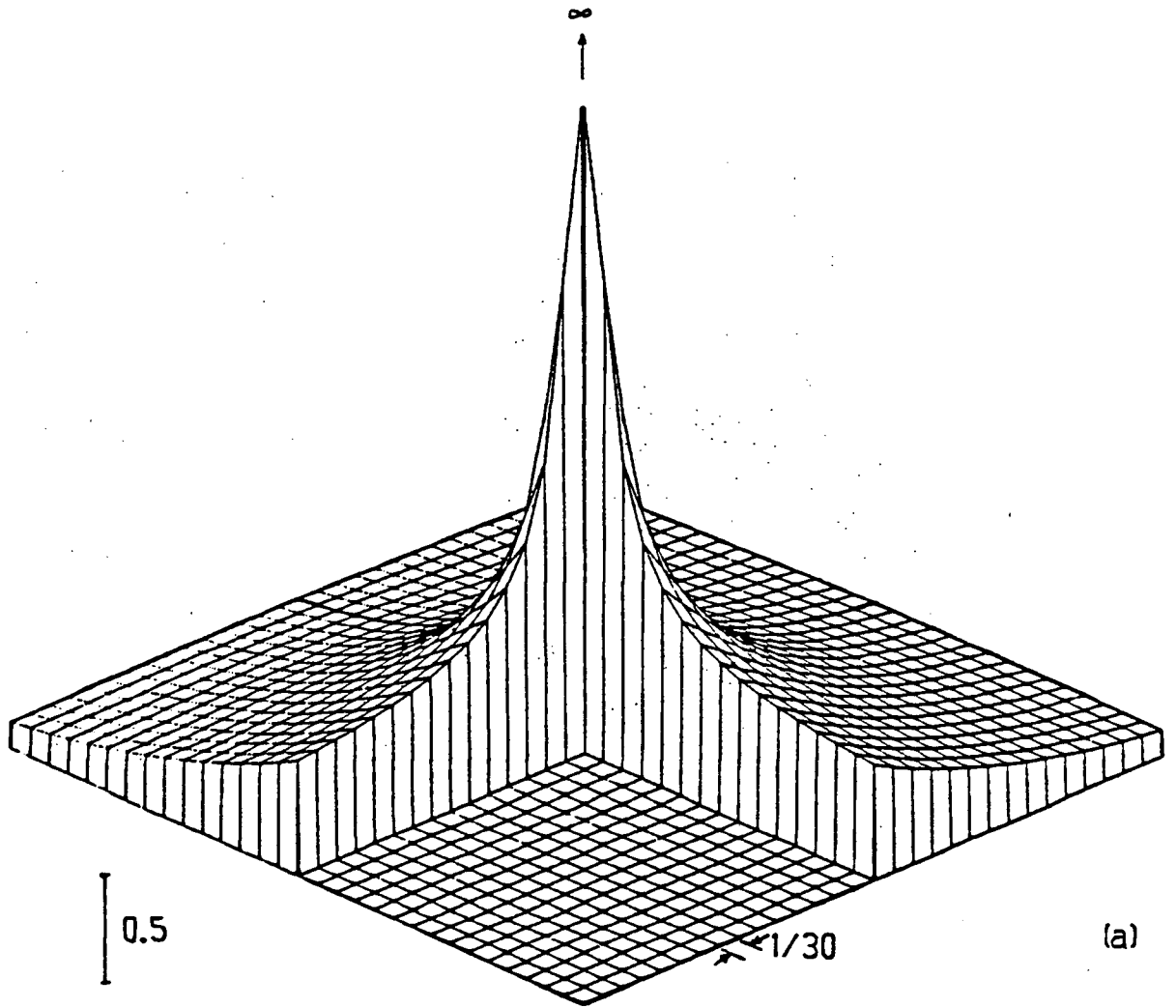


Figure 15. Depth integrated kinetic energy hU : (a) $\epsilon=0$, (b) $\epsilon=0.5$. For clarity, the $\pi/2$ corner was deleted in this figure.

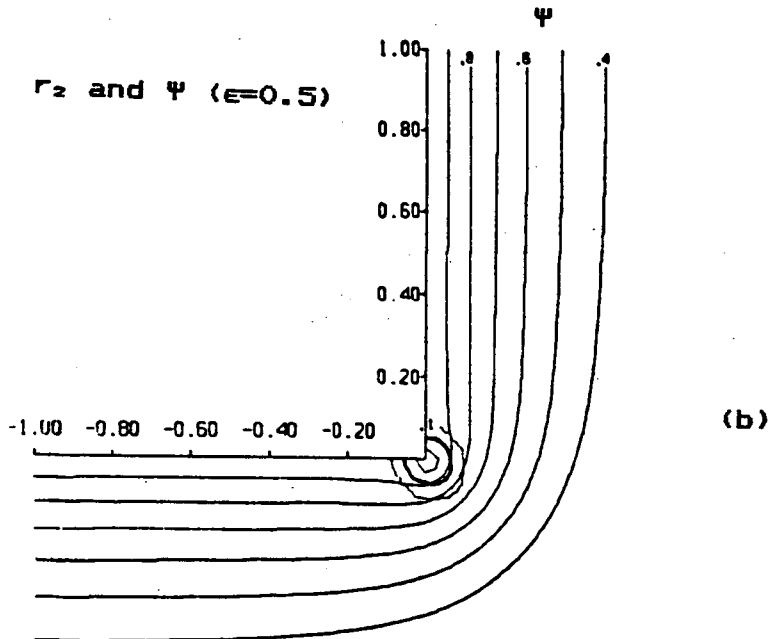
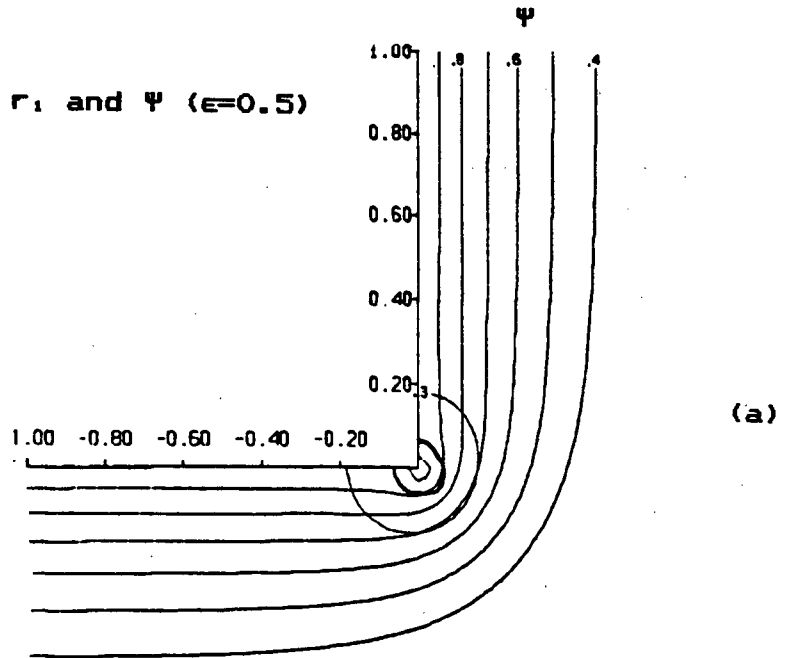
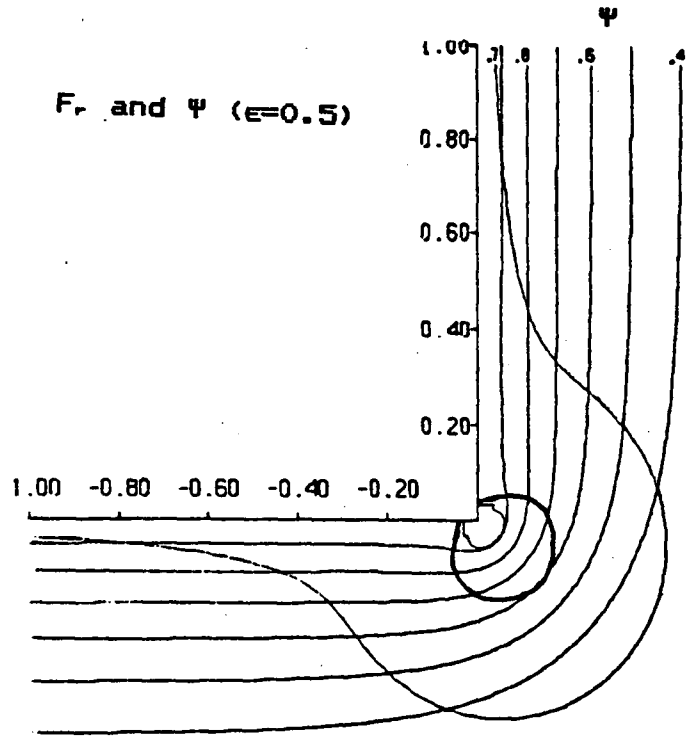


Figure 16. Contours of (a) $r_1=|h_1/h_0|=0.3, 1.0, 2.0$; (b) $r_2=|U_1/U_0|=0.1, 1.0, 3.0$ and (c) Froude number $F_r=0.7, 1.0, 2.0$. These are superimposed upon streamlines of $\Psi=0.4$ to 1.0 ($\epsilon=0.5$).



(c)

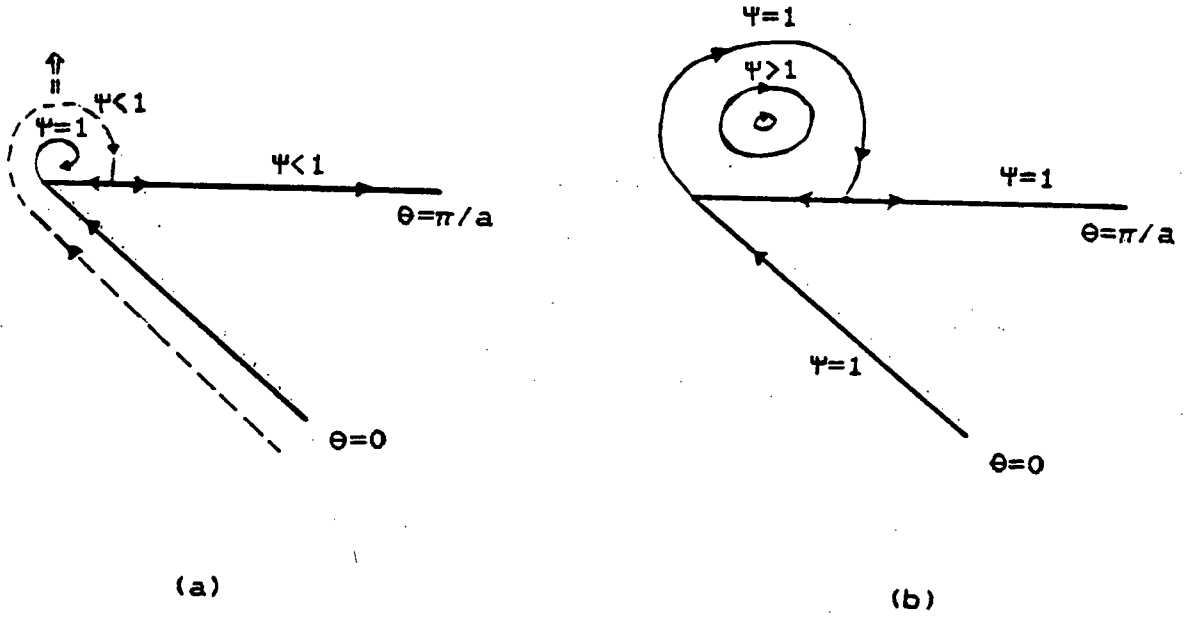


Figure 17. Conceptual drawing of the boundary streamline $\Psi=1$
(a) just after separation and (b) after reattachment.

Chapter 8

The case of more complicated geometries

The corner solution, given in the previous section, is readily extended to coastlines which are composed of two or more corners, as long as no two corners are closer than about one (nondimensional) unit. We invoke this restriction because of the nonlinear behaviour of the corner solution up to distances of 0.5 from the apex (Figure 13b), and because, for $r < 1$, the normal derivative of the diffraction term $F(\theta)$ does not vanish at the boundary $\theta=0$ (Figure 11a). For the case of a channel mouth, this restriction of minimum width can be relaxed if the nonlinear terms are small ($\epsilon \ll 1$). I chose the following examples to demonstrate the method.

Circulation in the mouth of a channel

LeBlond (1980) showed that in the case of wide channels, two baroclinic jets can coexist independently on opposite sides of the channel. In this respect, it may be convenient to classify channels into 3 categories: i) narrow channels, which are narrower than the Rossby radius of deformation; ii) intermediate channels, whose widths are between 1 and 3 Rossby radii; and, iii) wide channels, with widths larger than 3 Rossby radii. In a case when Rossby radii are different on opposite

sides of the channel, some average value can be used. In the absence of additional dynamical constraints (e.g., adverse pressure gradients), the last category, that of a wide channel is trivial, since the two jets do not interact at all. In order to give a simple example, I chose the case of a channel whose sides are at a right angle to the coastline. We orient the axes so that the two sides are parallel to the negative x axis, with the origin halfway between the two corners (as in Figure 7).

The solution $\Psi_0 = p^{4/3}$ is constructed as a linear superposition of two corner solutions,

$$p = B_1 p_1 + B_2 p_2 . \quad (8.1)$$

As we have shown in the previous chapter, our solutions are not valid in small areas around each sharp re-entrant corner. We can overcome this problem by rounding off these corners, so that the areas in question are removed from the domain of the solution. In order to round off the apex of each corner, p_1 and p_2 were rescaled by factors which we call recession parameters, $\exp(1.5\delta_1)$ and $\exp(1.5\delta_2)$, respectively. Each δ_i ($i=1,2$) is actually the distance between the side of the (recessed) corner and the boundary streamline, $\Psi=1$ (away from the apex; for example, on Figures 19a,b, it is the distance between the boundary $x=0, y>2$ and the rescaled streamline $\Psi=1$, since for $x>0$ and $y>2$ the presence of another corner has negligible effect on Ψ).

The constants B_1 and B_2 are calculated (for this case of

a nondivergent channel) from the requirement that far inside the channel

$$p(x,d) = 1 ,$$

and,

$$p(x,-d) = (1 + A)^{3/4} = 1 + B, \quad (8.2a,b)$$

where $A > -1$ is the additional transport out of the channel, $2d$ is the width of the channel and B is defined by (8.2b). For large negative x , $p_1 = \exp[-1.5(-y+d+\delta_1)]$ and $p_2 = \exp[-1.5(y+d+\delta_2)]$. Assuming for simplicity that p_1 and p_2 have equal radii of deformation and that $\delta_1 = \delta_2 = \delta$, we get from the 2-point matching, equations (8.1) and (8.2),

$$B_1 = \exp(1.5\delta) [e^{3d} - (1 + B)] / 2\sinh(3d),$$

and,

$$B_2 = \exp(1.5\delta) [(1 + B)e^{3d} - 1] / 2\sinh(3d), \quad (8.3a,b)$$

so that far inside the channel, where p is independent of x ,

$$p = (1+B/2)\cosh(1.5y)/\cosh(1.5d) - (B/2)\sinh(1.5y)/\sinh(1.5d). \quad (8.4)$$

The resulting $O(1)$ depth of the interface, $h_0 = p^{2/3}$, is shown for 5 different values of d on Figures 18a ($A=0$) and 18b ($A=1$). It is compared to the exact solution h (dashed line) from chapter 5. They are not exactly the same since the function M no longer

vanishes inside the channel and h_0 satisfies the nonlinear equation (6.16). The difference is relatively small, and insignificant for narrow ($d < 0.5$) or wide ($d > 3$) channels. The two solutions would be the same, if we used s in (8.1) instead of p . But then, in order for the linear superposition to be valid, we have to limit ourselves to $d > 0.5$. Note that while this 2-point matching procedure is not exact, it results in only minor distortions of boundary streamlines and is very simple to implement. (Only if $d < 0.5$ and $A \gg 1$ or $1 + A \ll 1$, the distortion may become large, in which case it is advisable to use different recession parameters, a larger one for a corner with a smaller transport.) Note that equation (8.4) is essentially Gill's (1977) equation (5.2), and is applicable to a channel of slowly varying cross-section.

Figures 19a,b show the resulting circulation, Ψ_0 for the case $d=1$, $\beta=0.1$, and for $A=0$ (zero net outflow) and $A=1$ (net outflow equals to the upstream transport). Only about 30% in the first case ($A=0$) and about 40% in the second case ($A=1$) of the upstream transport is recirculated across the mouth and out of the channel. The rest of the incoming transport continues up the channel. This is of course due to the dynamical control placed by the Rossby radius and the width of the channel upon the relative transports on the opposite sides. Differentiating (8.4) we find that p has a minimum at y_0 , given by

$$\tanh(1.5y_0) = [B/(2+B)] \cotanh(1.5d) . \quad (8.5)$$

In that case, $\Psi_0(y_0)$ is, in effect, the fraction of the incoming transport that is deflected across and out of the channel. In particular, when $B=0$ ($A=0$), $y_0=0$ and $\Psi_0(y_0) = [\cosh(1.5d)]^{4/3}$. If $1+B > \cosh(3d)$, then $y_0 > d$, and the flow is out of the channel even on the left bank (looking downstream). Similarly, when $0 < 1+B < \text{sech}(3d)$, then $y_0 < -d$, and the flow is uniformly into the channel. Figure 20a shows the relation between A and y_0 for 3 values of d : 0.5, 1.0, and 1.5 (which span the intermediate width category), while Figure 20b displays corresponding values of $\Psi_0(y_0) = p(y_0)^{4/3}$, the fraction of the incoming transport that is recirculated out of the channel.

A few remarks are in order. For the case of a channel with diverging coastlines, the same 2-point matching technique can be applied to the corners themselves, in which case $2d$ is the distance between the two apices. This is done in the next chapter, where we model the baroclinic flow in the mouth of Hudson Strait. In general, if it is deemed important, the $O(\epsilon)$ contribution s_1 can be calculated using either a narrow channel Green's function (see Buchwald, 1971) or via a numerical approach. Its effect is limited, as was seen in chapter 7, to the immediate neighborhood of each corner.

Flow around a square bump

In order to construct a solution for the second example,

we start with two corner solutions: one for the $3\pi/2$ ($a=2/3$) re-entrant corner, which was described in detail in chapter 7, and the other for an inside $\pi/2$ ($a=2$) corner. In addition, we use source and sink transport streamfunctions, $2F(\theta)$ and $2F(\pi-\theta)$, for a straight ($a=1$) coastline. The procedure is best described graphically, as shown in Figures 21a-f. We first subtract the source and sink functions, $2F(\theta)$ and $2F(\pi-\theta)$, from the re-entrant corner solution (Figure 21a), one unit distance upstream and downstream of the apex. This gives us the source and sink flow, shown on Figure 21b. Deleting the sink function $2F(\pi-\theta)$ from the inside corner solution (Figure 21c), one unit distance upstream of the apex, yields the source flow, shown on Figure 21d. Combining the last source with the sink on Figure 21b gives us the source flow, which is shown on Figure 21e. Finally, combining this source with its image (in the x-axis) sink and raising to the power $4/3$ results in Ψ_0 , the flow about the 2×2 square bump, as shown on Figure 21f. However, subtracting a source and a sink at a point on a straight boundary is equivalent to subtracting an exponential profile from that boundary. In other words, instead of using sources and sinks in the above procedure, one can simply add two corner solutions with a common boundary, and then subtract the resulting surplus exponential current profile from that boundary. The restriction of the common boundary being at least one unit long, stands as before, since the procedure is no longer valid close to the corners, where the profile is not exponential.

It is trivial to add a current in the opposite direction, which is (say) bounded by a wall 2 units away from the bump. The resulting baroclinic circulation around a square bump in a wide channel is shown on Figures 21g (the case of equal transports) and 21h (double transport in the opposite direction). Note that about 30% of the incoming transport in the first case, and about 40% in the second case is diverted back upstream by the opposing current. This is the same recirculation as in the case of the channel mouth (Figures 19a,b) and is caused by the dynamical constraint due to the scale of the Rossby radius of the flow.

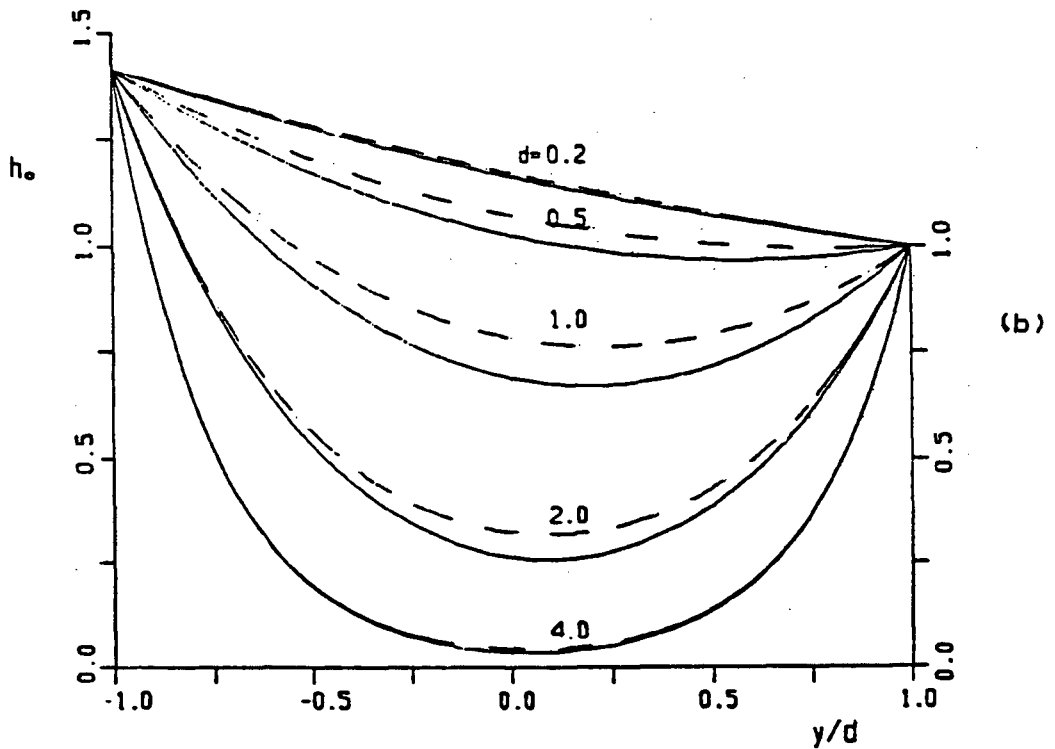
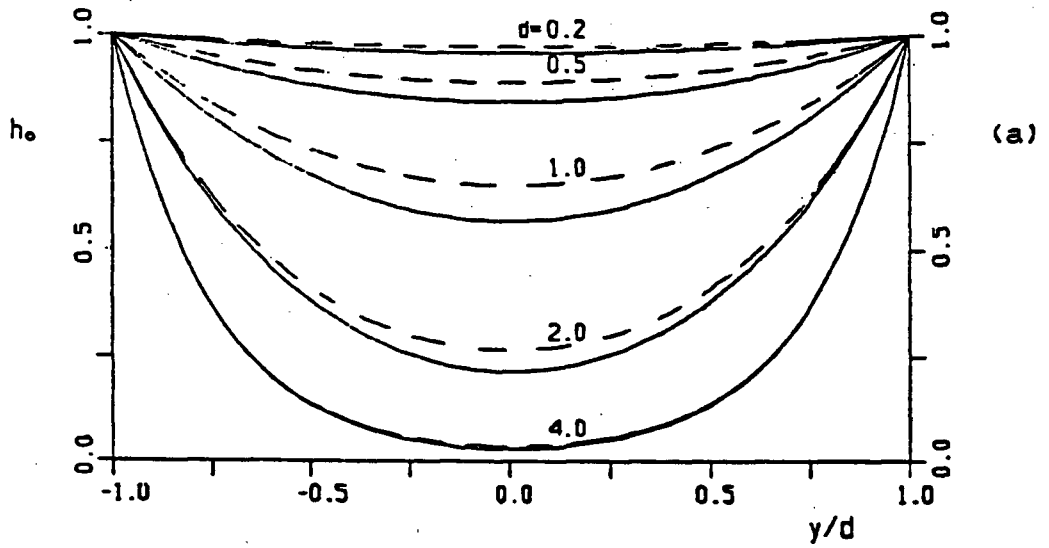


Figure 18. $h_0 = p^{2/3}$ inside a channel (solid line), compared to the exact solution h (dashed, from chapter 5), for several values of width, d , and for two values of the excess transport: (a) $A=0$ and (b) $A=1$.

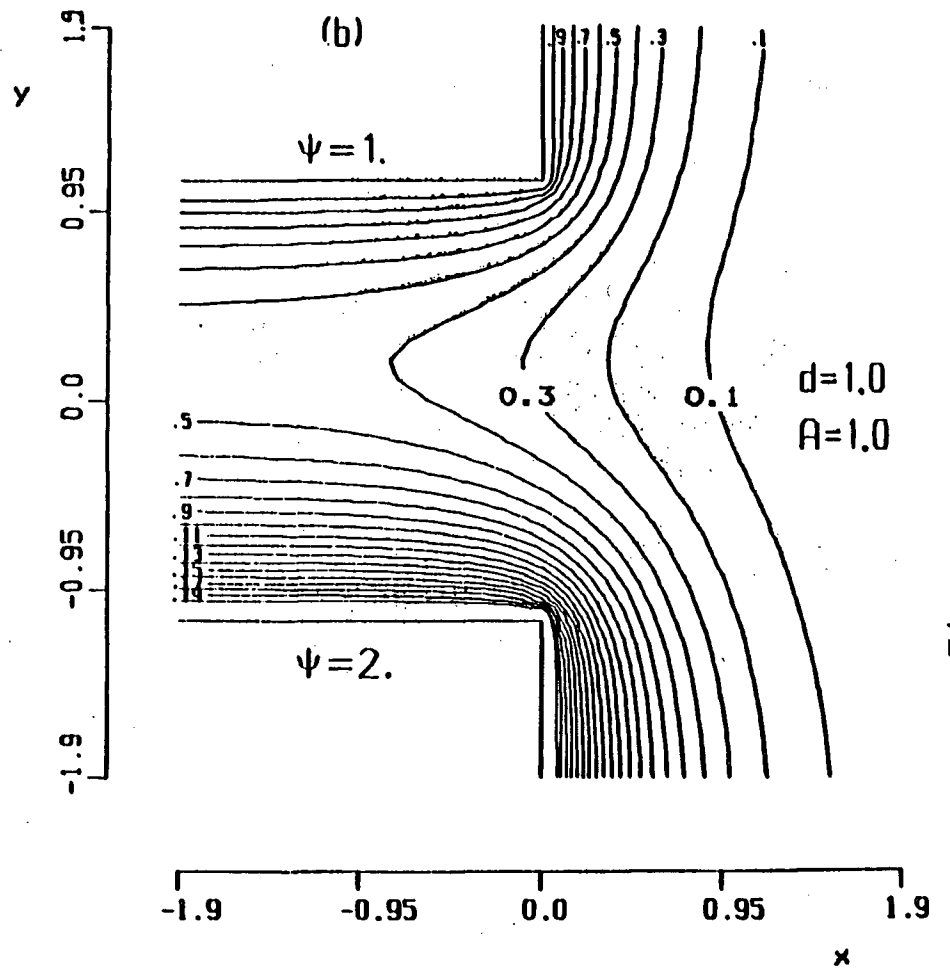
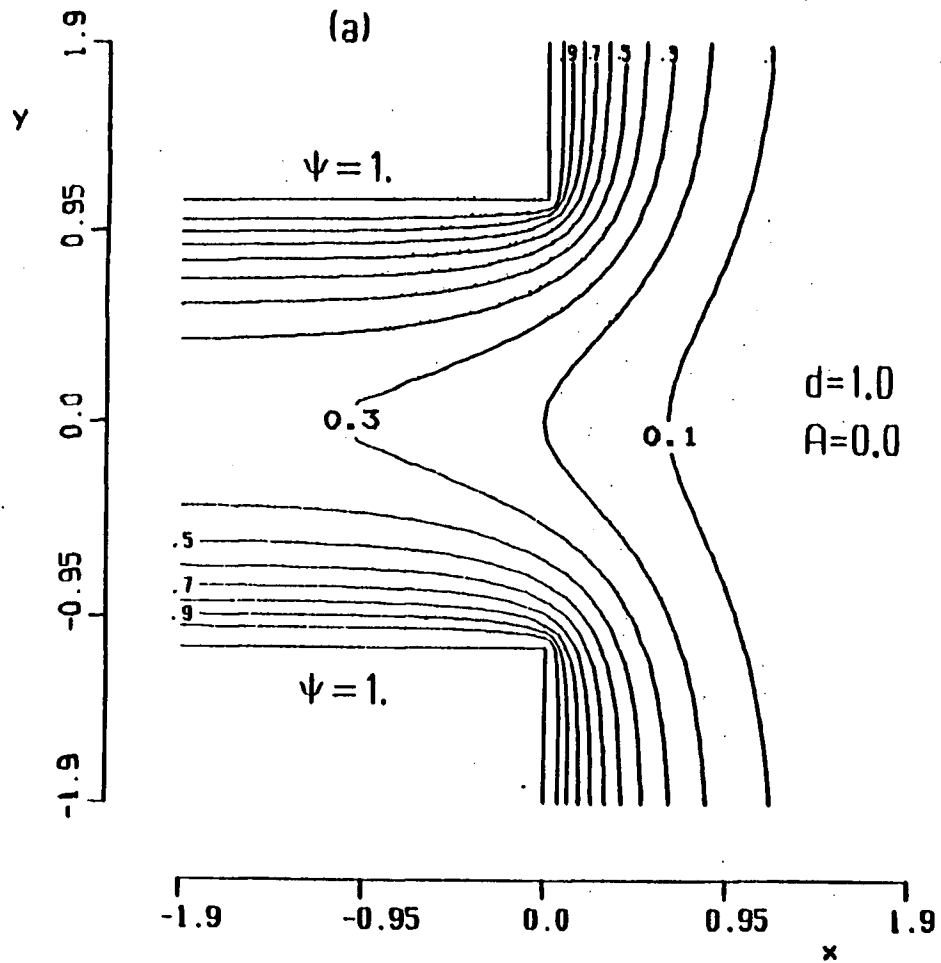


Figure 19. Circulation in the mouth of a channel: contours of the transport streamfunction ψ_0 for $d=1.0$, $f=0.1$: (a) $A=0$, (b) $A=1$.

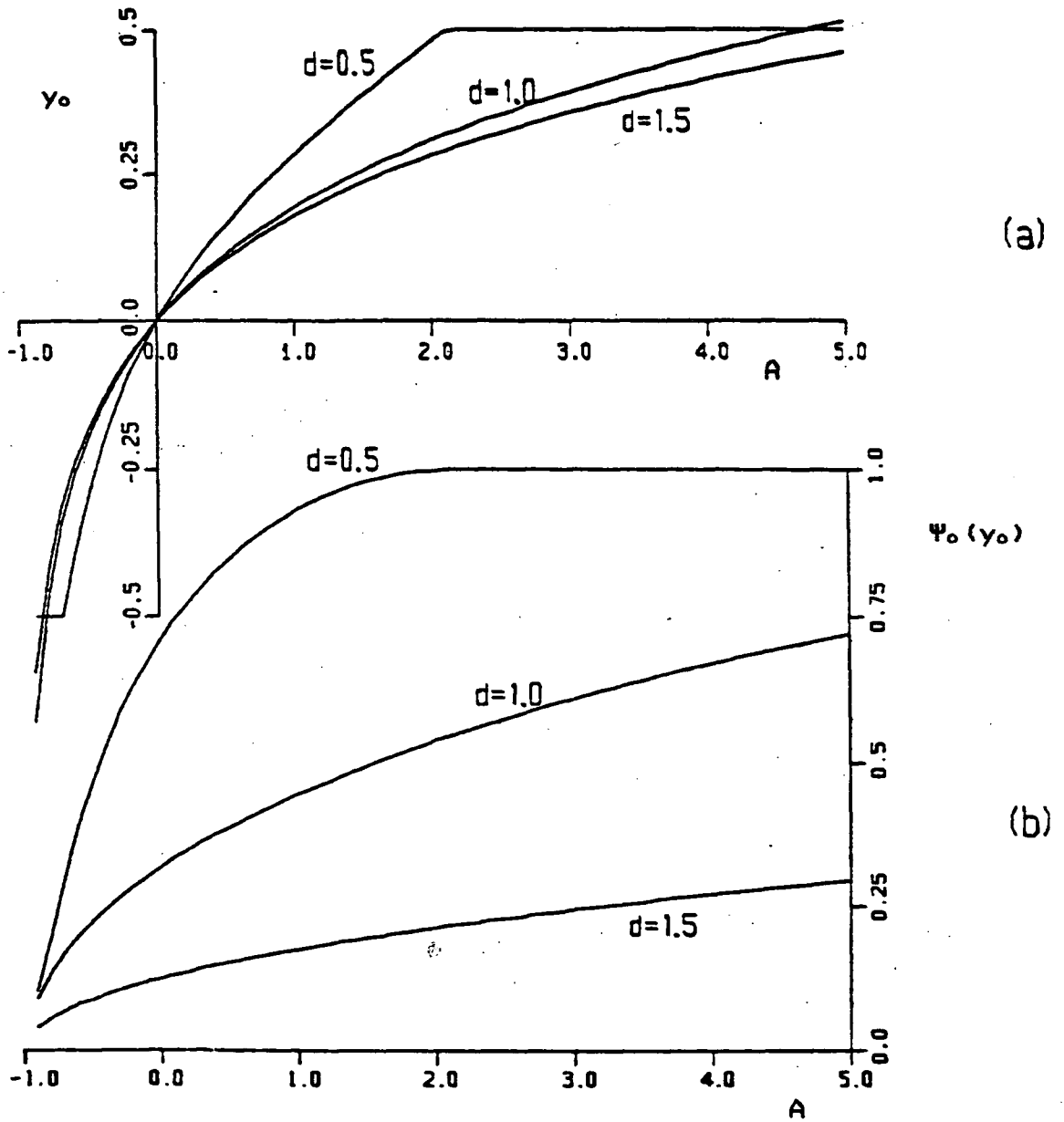


Figure 20. Location of the stagnation streamline, y_0 and its value there $\Psi_0(y_0)$, as functions of the transport parameter A , for 3 values of channel width: $2d=1$, $2d=2$ and $2d=3$.

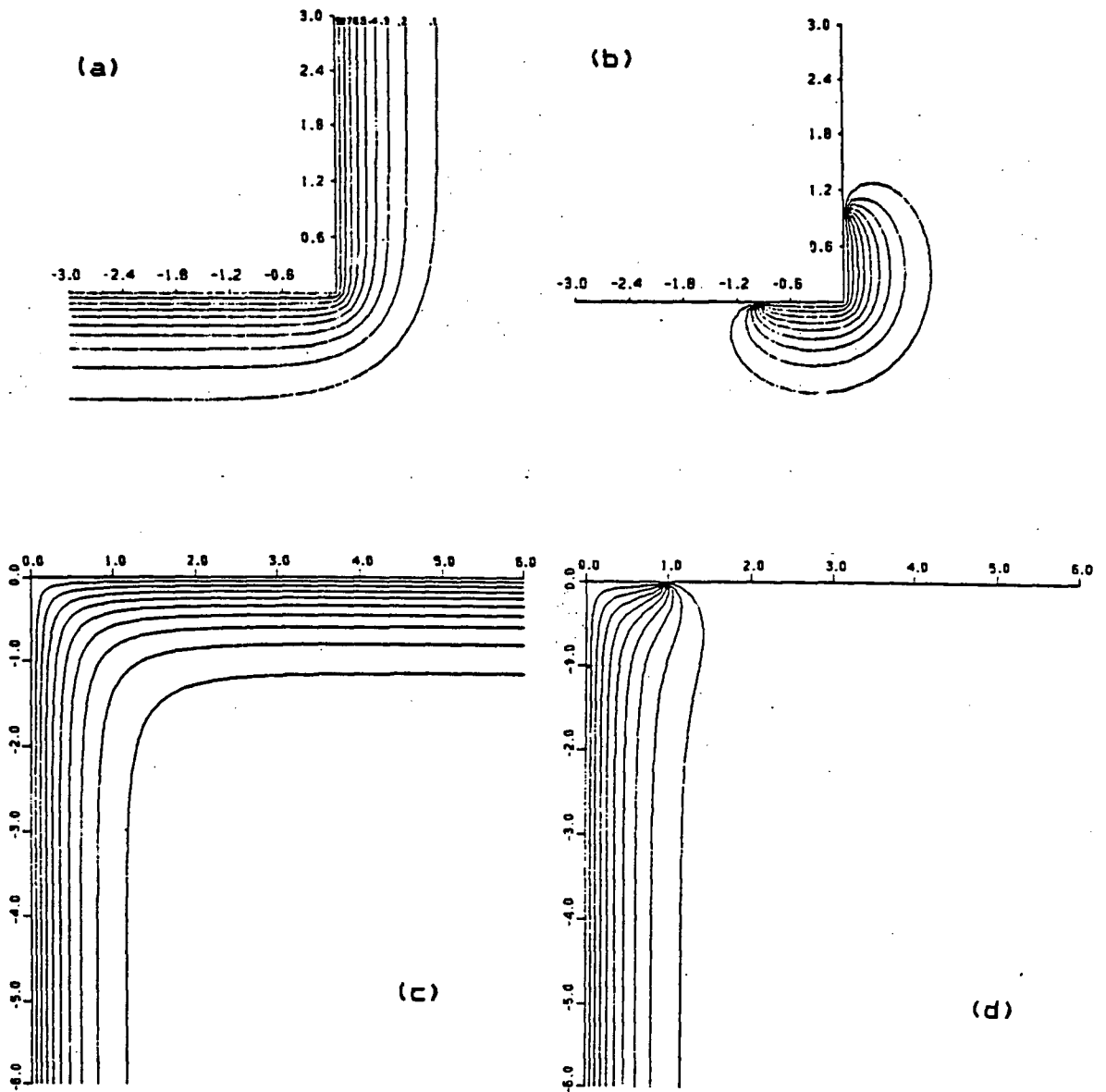
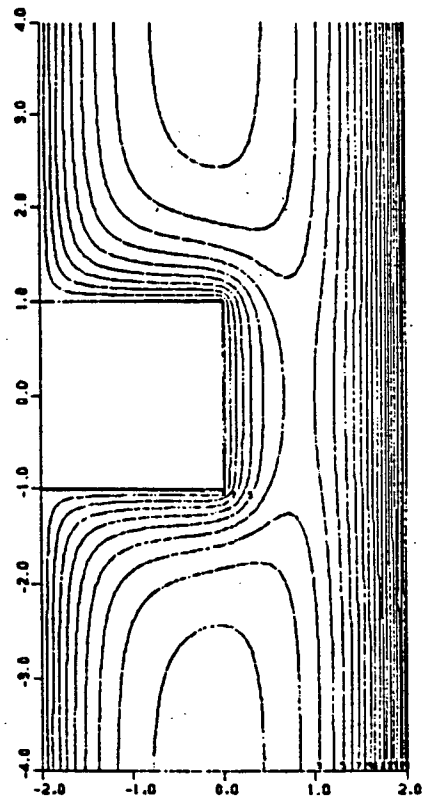
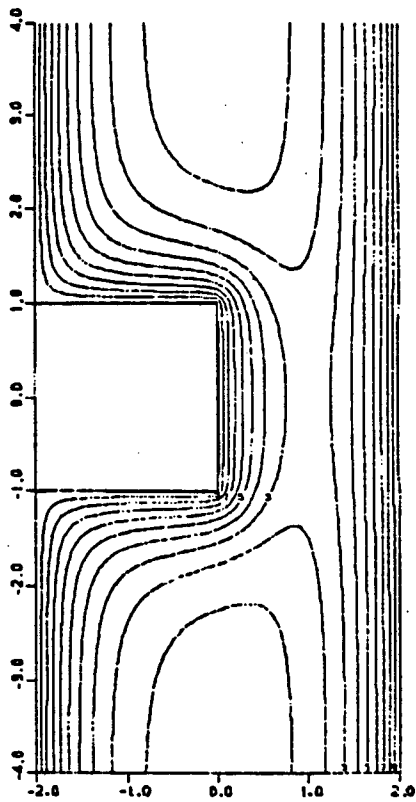
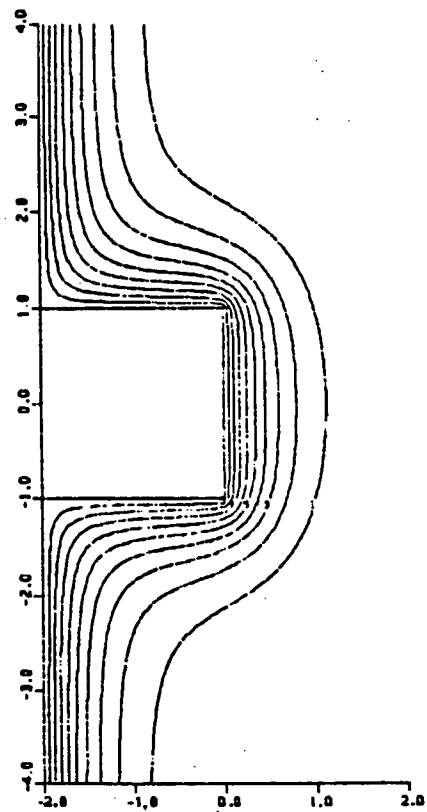
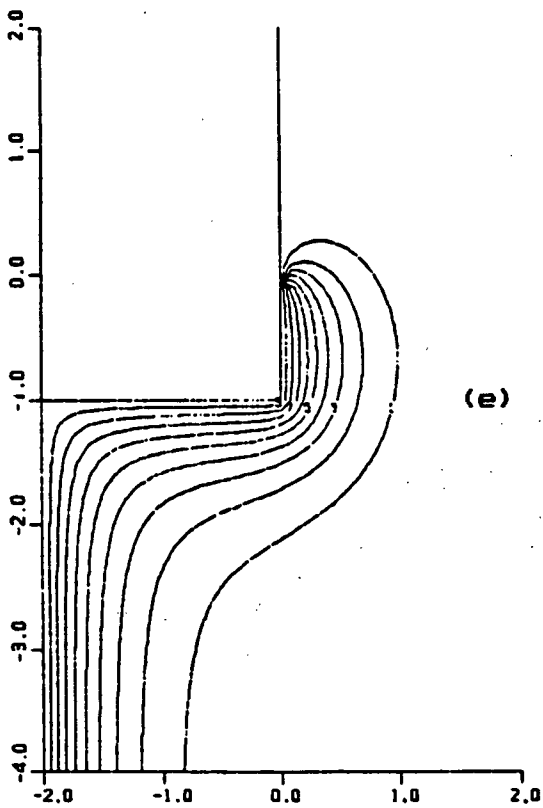


Figure 21. (a)-(f) Construction of the solution for a flow around a square bump in a coastline. A square bump in a channel for (g) $A=0$ and (h) $A=1$.



Chapter 9

Baroclinic circulation in Hudson Strait

In this Chapter we use the method outlined in the previous Chapter to model the baroclinic circulation near the mouth of Hudson Strait. It is expected that such a model would provide an adequate description of an upper layer flow above a quiescent lower layer, or whenever the changes in bathymetry are small enough, so that a modal decomposition is valid. Since the bathymetric changes in the mouth of Hudson Strait are not small (Figures 3b and 22a), we may alternatively consider the present model to represent only the "baroclinic part" of the total flow in and out of the strait.

For the purposes of this model (in order to provide upstream conditions), we require estimates of transports and of lateral scales for various currents inside and upstream of Hudson Strait. Where available, we rely on historical oceanographic data to obtain these quantities. Otherwise, we must make an intelligent guess.

The existing hydrographic and surface drogue data (Campbell, 1959; Drinkwater, 1983, 1985; Osborn et al., 1978; LeBlond et al., 1981, and references therein) and satellite imagery combine to give us a consistent picture of the late summer residual circulation in the strait. The Baffin Current flows south along the coast of Baffin Island (see Figure 22a).

At about 63°N it branches into two parts. The eastern part continues south past the mouth of Hudson Strait, while the western branch enters the strait on either side of Resolution Island. Inside the strait, one part of the flow is recirculated across and out of the channel. The remainder continues along its northern boundary and is gradually drawn across the strait into an estuarine type circulation, driven by the significant melt-water outflow from Hudson Bay. This water forms the current on the south side of the strait. It is fresher, colder and more strongly stratified than the one on the northern side. From the salinity and temperature sections across Ungava Bay (see Figure 23, from Campbell, 1959), it is apparent that a significant part of this current turns the corner at Cape Hope's Advance and enters Ungava Bay west of Akpatok Island. The remainder joins the above-mentioned cross-strait flow north of Akpatok Island and exits Hudson Strait past Cape Chidley together with the coastal current from Ungava Bay. Additional evidence for the Ungava Bay cyclonic gyre is provided by thermal satellite imagery (an example of which is shown on Figure 24) and also by the motion of ice into and out of the Bay. An example of the latter is shown on Figure 25 (from Gray et al., 1985).

The transports

Drinkwater (1985) made current measurements (Figure 3) and collected CTD data (Figure 26) in the eastern Hudson Strait. His

calculations of the total transport show that about $1.2 \times 10^6 \text{ m}^3/\text{s}$ is crossing the channel from north to south between his moorings HS3 and HS5 (see Figure 3). Similar amounts were given for flows along the north ($0.82 \times 10^6 \text{ m}^3/\text{s}$) and south ($0.93 \times 10^6 \text{ m}^3/\text{s}$) sides. This indicates that a total of about $2 \times 10^6 \text{ m}^3/\text{s}$ enters and exits the eastern entrance of the strait, which includes both the baroclinic and the barotropic parts of the flow. There are not enough data to calculate the transports of other current branches in the strait. Nevertheless, it may be logical on the basis of drogue tracks (Figure 2b) and satellite imagery (Figure 24) to assume that the flow that continues westward, on the north side of the channel, comes mainly from the shelf water east of Baffin Island and, hence, that most of it enters through Gabriel Strait. This would then indicate that the approximate transports on either side of the Resolution Island are of the order of $10^6 \text{ m}^3/\text{s}$ each. Similarly, we may assume that a large part of the $0.9 \times 10^6 \text{ m}^3/\text{s}$ flowing eastward at Cape Hope's Advance enters Ungava Bay east of Akpatok Island, while more than $1 \times 10^6 \text{ m}^3/\text{s}$, mostly from the cross-channel flow, rounds this island on its northern side. This completes the total transport estimates.

Since we are attempting a baroclinic model, we are more interested in estimates of geostrophic transports, which yield the baroclinic part of the flow. These are calculated from the temperature and salinity transects, assuming existence of a level of no motion (say, at 200m). Campbell's (1958) geostrophic calculations for July 1956 gave southeast transports along the

Quebec side of $0.6 \times 10^6 \text{ m}^3/\text{s}$ and northeast transports along the Baffin Island coast of $0.3 \times 10^6 \text{ m}^3/\text{s}$. He admitted that these might be underestimates, since his stations were not close enough to the shore. Drinkwater's (1985) calculations yielded comparable values of $0.66 \times 10^6 \text{ m}^3/\text{s}$ and $0.26 \times 10^6 \text{ m}^3/\text{s}$, respectively. After adjusting to current meter readings (at 200m at HS1 and at 100m at HS4), Drinkwater gave revised total transport figures of $0.59 \times 10^6 \text{ m}^3$ for the north side and virtually unchanged $0.66 \times 10^6 \text{ m}^3/\text{s}$ for the south side of the strait.

In our baroclinic model, we will assume that about $0.6 \times 10^6 \text{ m}^3/\text{s}$ enters Ungava Bay around Cape Hope's Advance, while $0.4 \times 10^6 \text{ m}^3/\text{s}$ rounds Akpatok Island on its north side, so that the total baroclinic outflow from the strait is about $10^6 \text{ m}^3/\text{s}$. In addition, we "guess" a value of $0.3 \times 10^6 \text{ m}^3/\text{s}$ entering the strait along the south side of Resolution Island. These values of baroclinic transports are marked beside the corresponding current arrows on Figure 22a.

Lateral scales

We now turn our attention to the lateral scales of the currents. We use the measured offshore values of depth, stratification and velocity in order to calculate X according to (4.1). For the south side of the strait (near Cape Hope's Advance), Drinkwater's calculations gave $C=0.8\text{m/s}$ and $R=6\text{km}$. Using his HS1 30m value of $V=0.3\text{m/s}$, we get $F=0.37$ and, from

(4.1), $X=18\text{km}$. We can also estimate X using the exponential profile for velocity $v(x)$ (equation (4.3)) and the two along-strait 30m velocity values at HS1 and HS2, which are 0.29m/s and 0.07m/s , respectively. Since the distance between HS2 and HS1 moorings is about 28km (see Figure 3), we get $28\text{km}/X=\ln(0.29/0.07)$, which gives $X=20\text{km}$, in good agreement with the 18km above. We also note that Drinkwater's mooring HS1 is located near the Cape Hope's Advance where at least part of the flow turns the corner into Ungava Bay and, it may be narrower there than the flow farther upstream.

Despite different water masses and weaker stratification on the north side of the strait (Figure 26), the lateral scale there may be comparable to that on the south side. This is because of the inverse dependence on V (equation (4.1)); in order to conserve the total transport, slower flows must be wider and deeper. To see this, let us use $\Delta\rho=0.3\text{kg/m}^3$ (compared to 1.5kg/m^3 on the south side; see Figure 26) and assume a reasonable value of $H=90\text{m}$, which is half the depth at HS4. Then, using the 30m (HS4) value of $V=0.09\text{m/s}$, we get from (4.1) a comparable value, $X=25\text{km}$. We also note that since HS4 is about 20km offshore, Drinkwater's measurements may have missed most of the baroclinic wedge at that location.

Because of large uncertainties in the method used to calculate these values of X , and in order to keep our model simple, we will assume that $X=20\text{km}$ on both sides of the strait. Moreover, in order to see the effect of larger scales, we will

repeat our calculations with a larger value, $X=30\text{km}$. The following argument lends support to also using a higher value of X in our model. The transport in a model baroclinic wedge profile (4.1) is given by

$$Q = VHX/2 = g'H^2/2f, \quad (9.1)$$

which for the southern side of the strait, near Cape Hope's Advance, gives (using Drinkwater's values, extrapolated to within 2km offshore, $H=75\text{m}$ and $V=0.45\text{m/s}$) $Q=0.34 \times 10^6 \text{m}^3/\text{s}$, which is about half of Drinkwater's geostrophic (relative to 200m) transport value of $0.66 \times 10^6 \text{m}^3/\text{s}$. On the north side (near HS4), a similar calculation (with $H=90\text{m}$, $X=20\text{km}$ and, $V=0.19\text{m/s}$, extrapolated to within 5km offshore, since the bottom is less steep there) also gives $Q=0.34 \times 10^6 \text{m}^3/\text{s}$, which is comparable to Drinkwater's value of $0.26 \times 10^6 \text{m}^3/\text{s}$.

There is a disagreement between the two methods used to calculate Q on the south side, near Cape Hope's Advance. One possible reason for this is that we may have underestimated X . From the cross-channel density contours (Figure 26, if the σ_t surface of 25.75 is taken as the interface) we may infer that the cross-stream scale is closer to $X=35\text{km}$. Then, using the same extrapolated values of $H=75\text{m}$ and $V=0.45\text{m/s}$, we get a revised figure of $Q=0.59 \times 10^6 \text{m}^3/\text{s}$, which is much closer to Drinkwater's $0.66 \times 10^6 \text{m}^3/\text{s}$, or to Campbell's (1958) value of $0.6 \times 10^6 \text{m}^3/\text{s}$. This last calculation lends extra support for trying both values,

$X=20\text{km}$ and $X=30\text{km}$ in our model.

The circulation

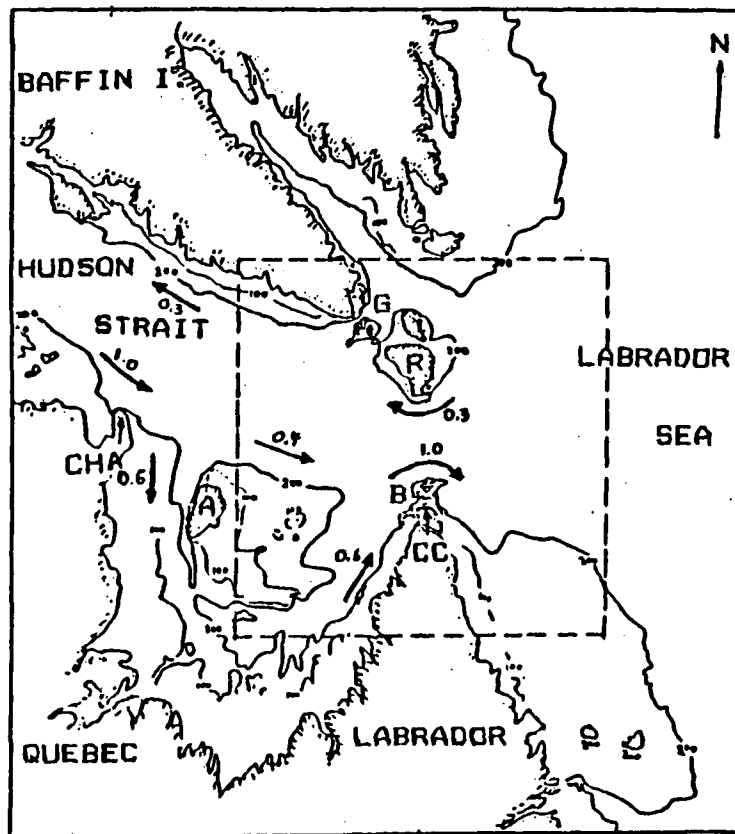
We now proceed to construct analytical solutions of the baroclinic circulation in the mouth of Hudson Strait. Since the Rossby number of the flow upstream of Cape Chidley is of the order of $\epsilon=0.2$ (based on $F=0.37$, from Drinkwater's (1985) values), the extent of the centrifugal upwelling is quite small (less than $0.1X$ in this case, which is 3km at most), and is even smaller at other capes. Hence, for corners with radii of curvature of the order or greater than $0.1X$, the centrifugal upwelling is negligible. The radius of curvature of the Cape Chidley coastline (or even of the Button Islands group) is of the order of 10km . Hence, except for the extra spreading of streamlines near the apex, the $O(1)$ solution is quite adequate to describe the baroclinic flow around Cape Chidley. The same applies to other capes in our model, such as the southern tip of Resolution Island.

Using the method of a linear superposition of recessed corner solutions, which was described in the previous chapter, we construct the contours of the function p in the $320 \times 320\text{km}$ area, centered at the midpoint of the mouth of Hudson Strait (Figure 22b). We approximate the 100m contours (where available; or else, we interpolate inside the 200m contours; see Figure 22a) with straight line segments, which are combined to represent the tip

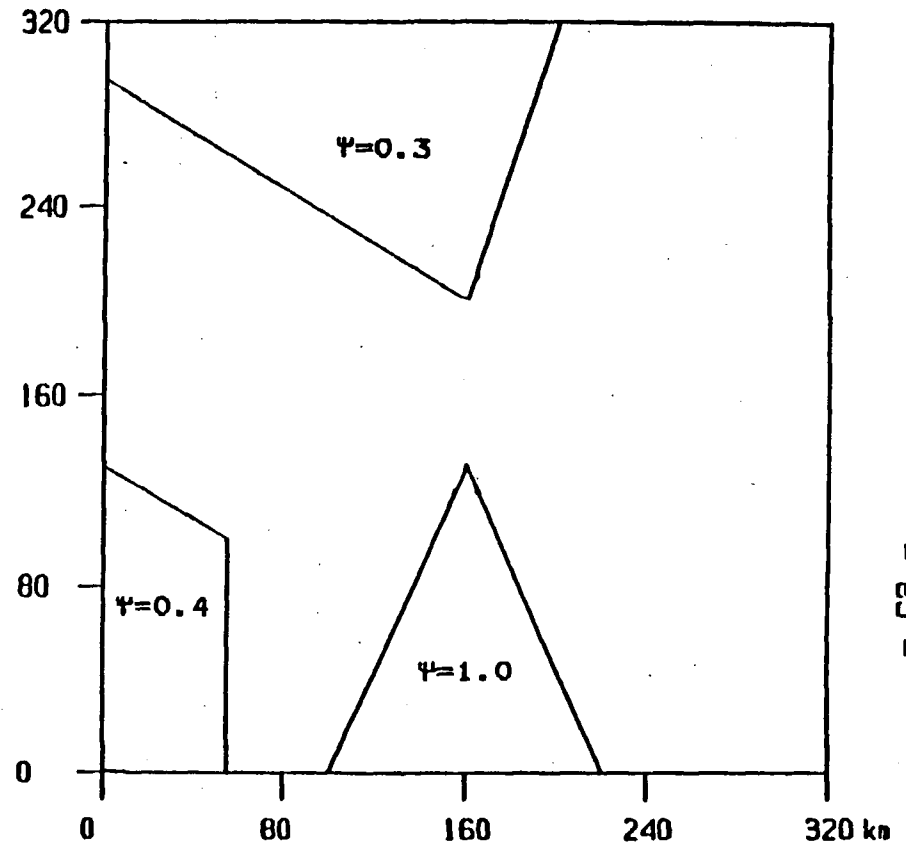
of Resolution Island, the Labrador Peninsula and the shallow (about 100m deep) bank east of Akpatok Island (see Figure 22b). The 100m value was chosen, since no charts with lesser contours are available and also because the boundary value H is close to this value. The resulting contours of $h=p^{2/3}$ and $\Psi=h^2$ are shown for $X=20\text{km}$ on Figures 27a,b, and for $X=30\text{km}$ on Figures 27c,d. The transports were normalized to the baroclinic outflow around Cape Chidley, which was assumed to be about $10^6\text{m}^3/\text{s}$ (composed of $0.6 \times 10^6\text{m}^3/\text{s}$ from Ungava Bay and the more uncertain value of $0.4 \times 10^6\text{m}^3/\text{s}$ from the north side of Akpatok Island; alternatively, the last value may be treated as another parameter of the model). We also selected the baroclinic part of the transport on the south side of Resolution Island to be $0.3 \times 10^6\text{m}^3/\text{s}$, which is comparable to the given value of the geostrophic transport on the north side of Hudson Strait.

Comparison between Figures 27a-d and the sigma-t section in Figure 5 seems to indicate that the higher value of $X=30\text{km}$ fits the data better. This is especially true for the south side of the strait, where there is a more pronounced two-layer structure. We can conclude this section by saying that despite our assumptions of a uniform stratification and of equal scales for the two sides of the strait and despite "guessing" the value of Ψ on the north side, we got a good qualitative agreement between the model and the known circulation pattern near the mouth of Hudson Strait. In order to have an even better agreement, it may be necessary to have a model which combines two (or more) moving

layers with the realistic bathymetry of the strait. Such task is best accomplished using numerical methods.



(a)



(b)

Figure 22. (a) The eastern Hudson Strait and Ungava Bay area. Only 200m and 100m (where available) contours are shown. The dashed box contains the area covered by the present baroclinic model. Arrows with numbers show directions and approximate values ($\times 10^6 \text{ m}^3/\text{s}$) of baroclinic transports (see the text). Place names abbreviations: CHA - Cape Hope's Advance, A - Akpatok Island, R - Resolution Island, CC - Cape Chidley, B - Button Islands and G - Gabriel Strait. (b) Simplified model boundaries, with adopted values of Ψ .

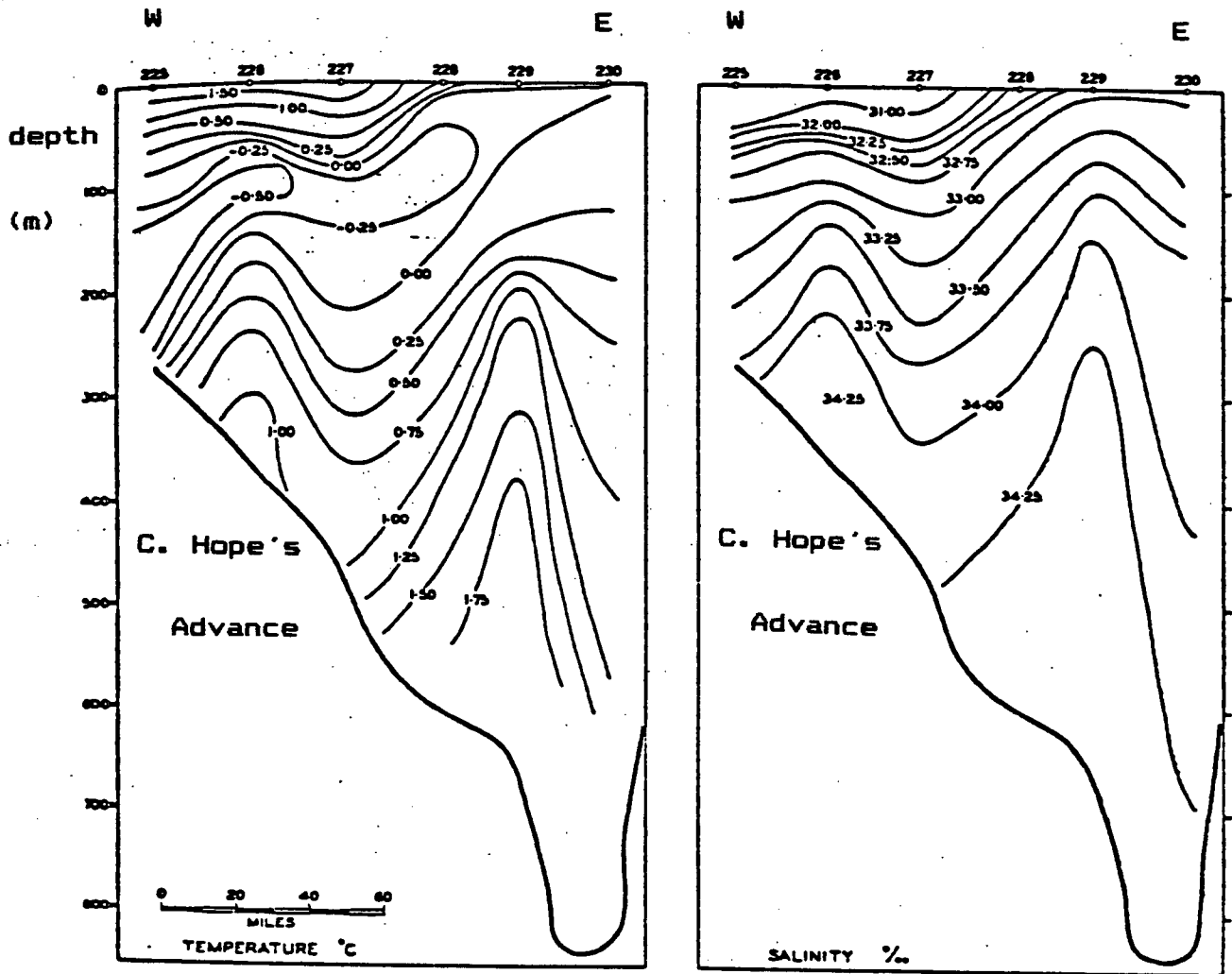


Figure 23. East-west sections of temperature and salinity across the mouth of Ungava Bay (reproduced with permission from Campbell, 1958).

Figure 24 (next page). An example of thermal surface signature of circulation in Hudson Strait and Ungava Bay. The coldest water (-2 deg C) is dark blue, while the warmest (about 5 deg C) is deep red. Clouds, fog and ice are at about the same temperature, they were given here a bright blue shade. Land (black) features can be identified from Figure 22.



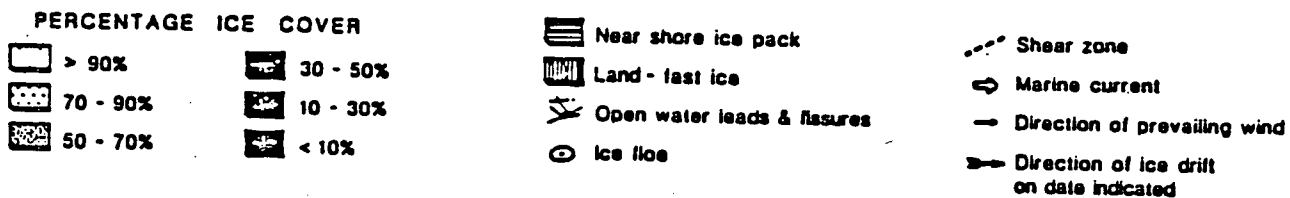
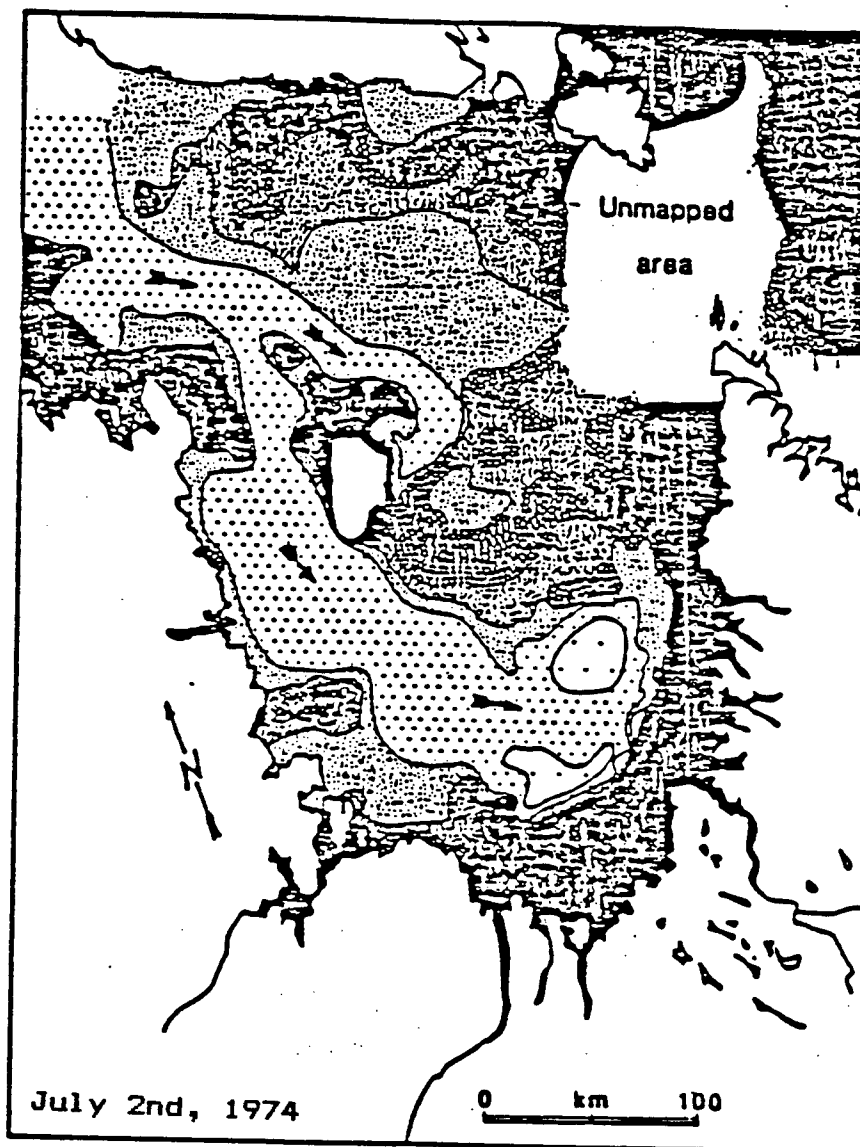


Figure 25. Map of the ice cover in Ungava Bay and eastern Hudson Strait on July 2nd, 1974 (reproduced with permission from Gray et al., 1985).

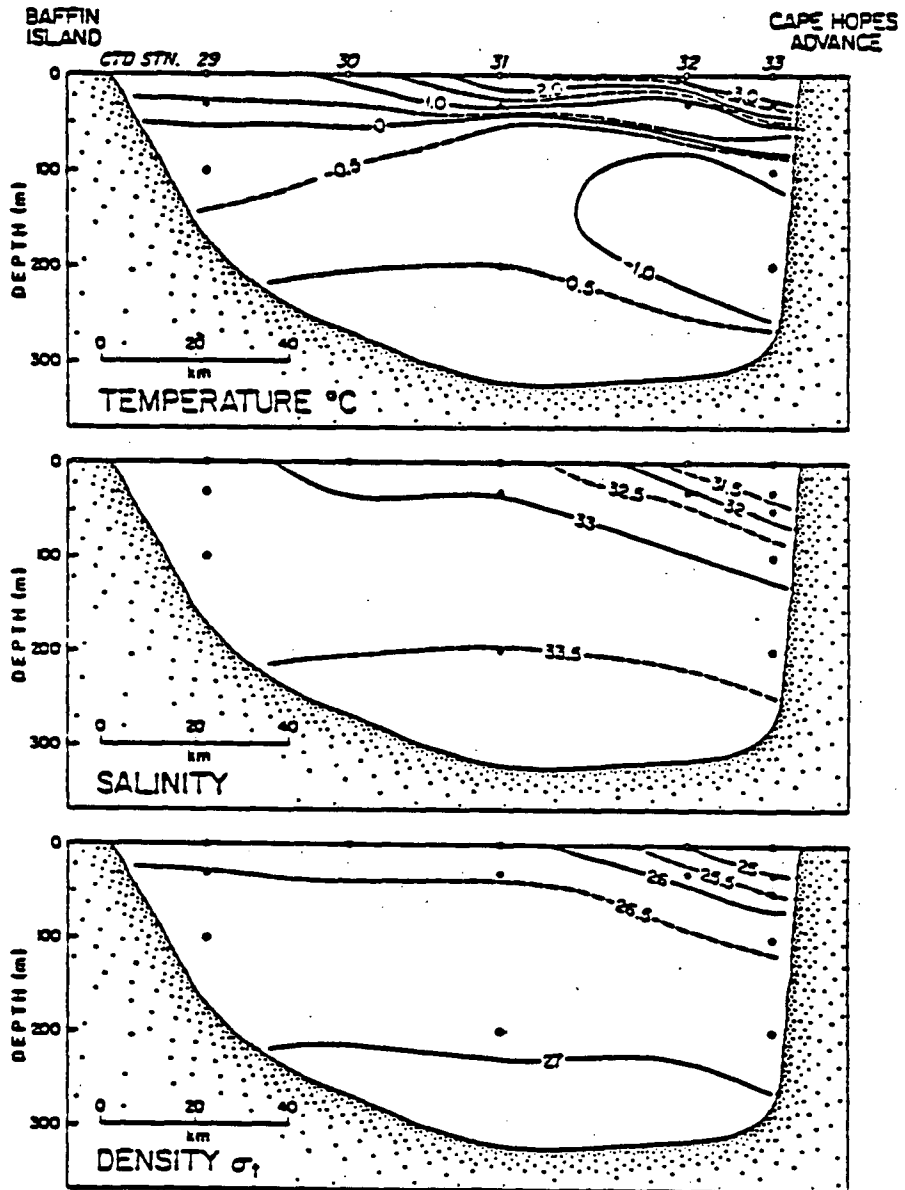


Figure 26. Temperature, salinity and sigma-t transects across Hudson Strait in Aug. 1982. These transects were made along the line occupied by moorings HS1-HS4, shown on Figure 3a (reproduced with permission from Drinkwater, 1985).

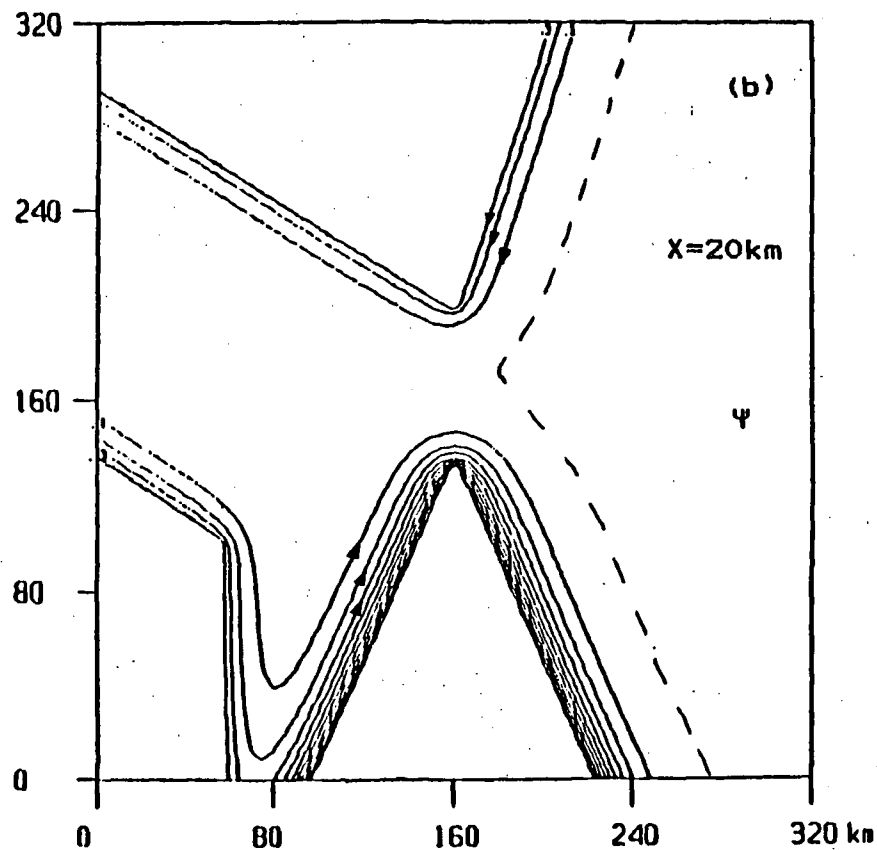
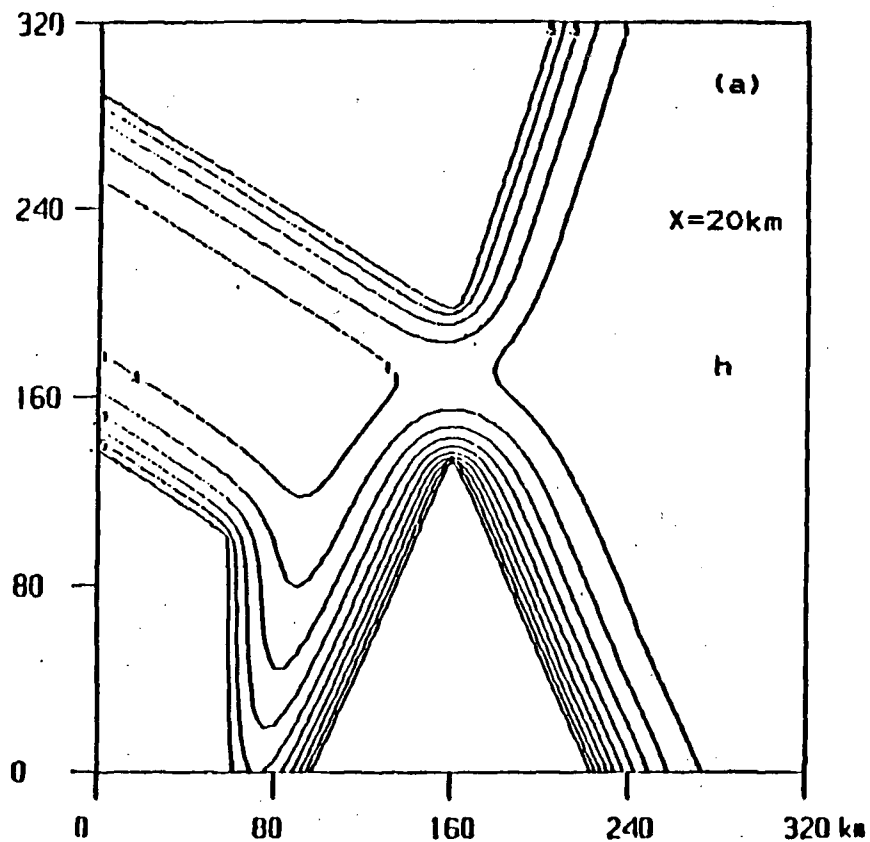
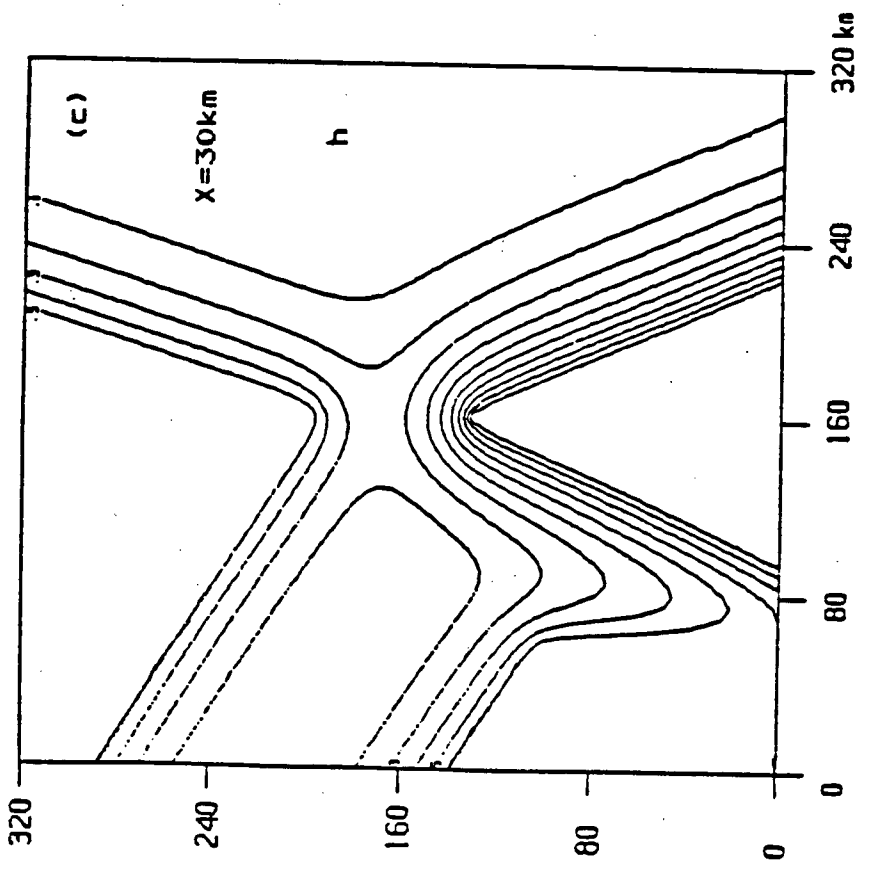
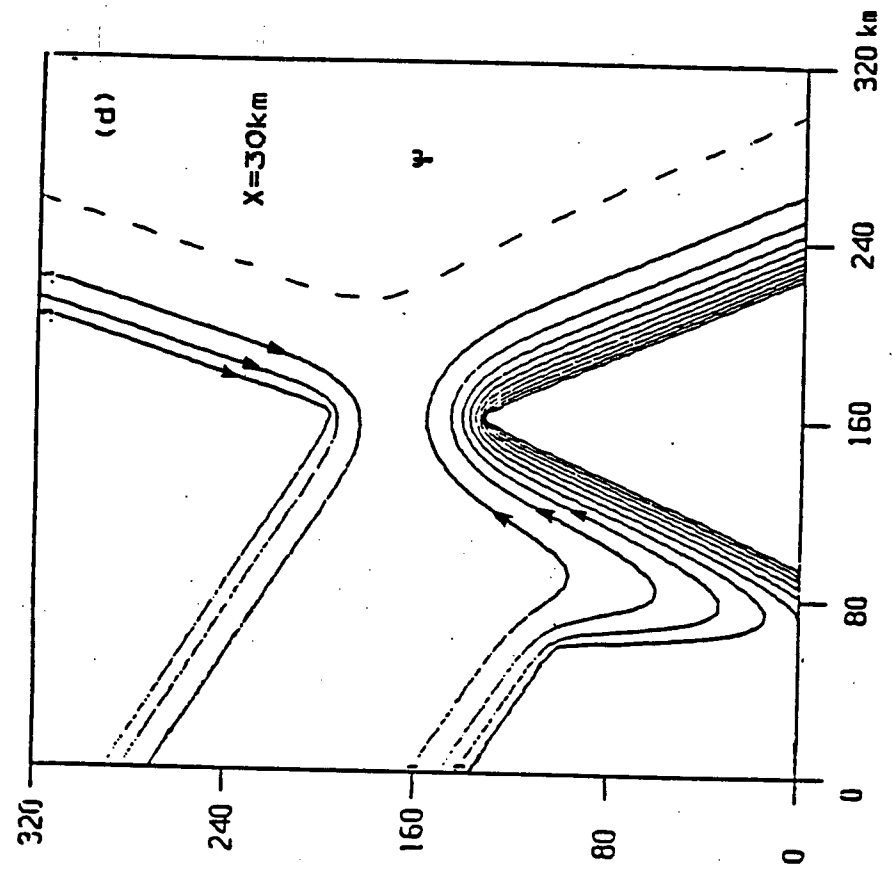


Figure 27. Baroclinic model contours of the $O(1)$ depth h_0 and the $O(1)$ transport streamfunction Ψ_0 for (a,b) $X=20\text{km}$ and (c,d) $X=30\text{km}$. As before, contour spacing is 0.1, except that one extra 0.01 contour was added to plots of Ψ_0 (dashed line), indicating schematically the edge of the flow, where $h_0=0.1$.



Chapter 10

Discussion

From the nonlinear conservation equations that govern an inviscid upper-layer flow in a two-layer rotating fluid, we obtained the first two terms of the power series which represents the solution to the problem of a flow around an arbitrary corner. It was found that the $O(1)$ term is geostrophic and, except for narrowing (widening) of the flow near a re-entrant (inside) corner, it does not differ qualitatively from the flow upstream. The effects of the nonlinear (advection) terms in the equation of motion become quite evident when the $O(\epsilon)$ term is added to the first: the flow widens (for re-entrant corners) due to the centrifugal acceleration of the fluid and, in addition, the depth of the upper layer decreases to almost zero near the apex of the corner (although we did not calculate this explicitly, we assumed that near inside corners the effect is opposite; the $O(\epsilon)$ terms cause some increase in the depth). This is a manifestation of the centrifugal upwelling (downwelling). This upwelling is only important for relatively sharp corners. The validity of the solution and the continuity of the boundary streamline (i.e., the absence of separation) require that the sharp apex of the re-entrant corner be blunted to a certain extent. This can be successfully accomplished if one of the neighboring streamlines is assumed to be the physical boundary, the choice depending

upon the required radius of curvature. Using these recessed corner solutions we were able to generate streamlines of plausible flows in more general domains: inside channel mouths and around coastal indentations.

The relative simplicity of the model as well as the scarcity of data do not allow for more than a qualitative comparison between the theory and actual baroclinic corner flows in the vicinity of the mouth of Hudson Strait. Nevertheless, there is fairly good agreement between the model flow and the baroclinic circulation in the eastern part of the strait. There is no contradiction between the tracks of drogues that were released near the mouth of Hudson Strait (figure 2b) and the current meter measurements inside this channel (figure 3). Surface drogues show the Lagrangian component of the motion that is subject to preferential diffusion in a shear current and to wind drift effects. On the other hand, current meters and geostrophic calculations give Eulerian velocities at a fixed location. The existence of opposing currents is strong evidence of the importance of stratification in these channels, and, hence, justifies the use of a baroclinic model. The reversals in these currents are most likely caused by adverse (barotropic and/or baroclinic) pressure gradients, which may be due to the influx of fresh water or changes in bathymetry.

Further improvements to the present model will come from the incorporation of alongshore pressure gradients effects. These may be due to changes in buoyancy (e.g., due to coastal sources),

or due to compression of the vortex lines by changes in the total depth. For example, in the case of a "long" bathymetry (horizontal scale L much larger than X), we may use a method similar to that of Cushman-Roisin and O'Brien (1983) and apply a perturbation expansion in a small parameter X/L . For $X/L \ll \epsilon < 1$, the full corner solution is still valid locally near each corner, including the $O(\epsilon)$ terms, except that k (e.g., in equation (7.9)) is modulated (in the WKB sense) by changes in bathymetry. If $X/L \sim \epsilon$, then the $O(\epsilon)$ equation (7.10) must also be modified to include these barotropic effects.

The infra-red image of the surface temperature in Hudson Strait (see figure 24) is an especially good example of complexity of the flow and, in particular, of the role of bathymetry and mixing, which were not included in the present model. The effect of bathymetry on the circulation inside the strait can be seen from the cross-channel flow north of Akpatok Island. It can be traced by the intrusion of cold (blue colour) water into the warmer (red and pink) flow on the south side. Similar, but weaker (because of smaller along-channel bottom slopes), current reversals can be seen farther inside the channel. In addition, the bathymetry has a strong channeling effect on the outflow east of Cape Chidley, where the presence of relatively shallow (with depth of the order of 100m) and wide (about 120km) shelf splits this cold (blue) outflow into two parts. Temperature is only a surface tracer and, hence, it is a poor indicator of actual transports. Nevertheless, it seems to

show that a larger portion of the flow follows the shelf-break eastwards into the Labrador Sea, while the rest flows along the eastern coast of Labrador Peninsula.

Diffusion affects coastal currents on scales that are much larger than the width (X) of the flow (e.g., Sanderson and LeBlond, 1984). In the same satellite image (figure 24), the cooling and warming of coastal currents along the eastern shores of Quebec and Labrador are most likely due to tidal mixing. Moreover, it is most pronounced in the mouth of the channel, where the sill and the constriction produce very strong tidal currents, of the order of 2m/s (Osborn et al., 1979). As a result of the strong mixing in the mouth, the generally warmer (pink and red colours) surface flow east of Resolution Island cools down closer to an average temperature of the water column (blue colour) as it enters the strait south of the island. The same thing happens to the outflow around Cape Chidley. The warm (pink) surface layer is mixed closer to the average temperature of the water column. It is interesting to note that despite this vigorous mixing, the strong residual motion keeps the flow stratified in the mouth (see figure 5).

Effects stemming from the variability of the flow were not included in the present study. For example, the criterion for separation of the flow at a sharp cape (chapter 7 and appendix C) would have to be modified if the sum of residual and tidal currents is sufficient to cause separation at some stage of the tide. Once separated, the flow is likely to remain that way,

even during reversals of the tide. This is due to the adverse pressure gradient from the closed gyre (see figure 17) that was created on the downstream side of the cape. It is tempting to suggest that this mechanism may be responsible for the separation of the Gibraltar surface flow from the right bank as it enters the Alboran Sea. A detailed investigation of the available data may provide a test of this suggestion.

References

- Ames, W.F. 1965 Nonlinear Partial Differential Equations in Engineering. Academic Press.
- Bromwich, T.J. 1915 Diffraction of waves by a wedge. Proc. London Math. Soc. 14, 450-463.
- Buchwald, V.T. 1968 The diffraction of Kelvin waves at a corner. J. Fluid Mech. 31, 193-205.
- Buchwald, V.T. 1971 The diffraction of tides by a narrow channel. J. Fluid Mech. 46, 501-511.
- Campbell, N.J., 1958 The oceanography of Hudson Strait. Fish. Res. Board Can. MS Rep. Ser. No. 12.
- Carrier, G.F., Krook, M. and Pearson, C.E. 1966 Functions of a complex variable: theory and technique. McGraw Hill.
- Carslaw, H.S. 1919 Diffraction of waves by a wedge of any angle. Proc. London Math. Soc. 18, 291-306.
- Charney, J.G. 1955 The Gulf Stream as an inertial boundary layer. Proc. Nat. Acad. Sci. 41, 731-740.
- Cherniawsky, J. and LeBlond, P.H., Rotating flows along indented coastlines. J. Fluid Mech., in press.
- Collin, A.E. 1962 The waters of the Canadian Arcipelago. Bedford Inst. Oceanogr. Report No. 62-2.
- Cushman-Roisin, B. & O'Brien, J.J. 1983 The influence of bottom topography on baroclinic transports. J. Phys. Oceanogr. 13, 1600-1611.
- Drinkwater, K.F. 1983 Moored current meter data from Hudson Strait, 1982. Can. Data Rep. Fish. Aquat. Sci. 381: iv+46p.
- Drinkwater, K.F. On the mean and tidal currents in Hudson Strait. Atmosphere-Ocean, in press.
- Fenco Consultants Ltd and F.F. Slaney & Co. Ltd 1978 An Arctic Atlas: Background information for developing marine oil spill countermeasures. Arctic Marine Oil Spill Program Report EPS-9-EC-78-1. Fisheries and Environment Canada.
- Fissel, D.B., Lemon, D.D. & Birch, J.R. 1982 Major features of

- the summer near-surface circulation of western Baffin Bay, 1978 and 1979. *Arctic* 35(1), 180-200.
- Flierl, G.R. 1979 A simple model for the structure of warm and cold core rings. *J. Geophys. Res.* 84(C2), 781-785.
- Gill, A.E. 1977 The hydraulics of rotating-channel flow. *J. Fluid Mech.* 80, 641-671.
- Gill, A.E. 1982 *Atmosphere-Ocean Dynamics*. Academic Press.
- Gill, A.E. & Schumann, E.H. 1979 Topographically induced changes in the structure of an inertial coastal jet: application to the Agulhas Current. *J. Phys. Oceanogr.* 9, 975-991.
- Gray, J.T., Dupont, J. and Lauriol, B. Application of Landsat images to the mapping of seasonal and diurnal sea ice regimes in Ungava Bay and Hudson Strait. *Arctic*, in press.
- Gutman, L.N. 1972 *Introduction to the Nonlinear Theory of Mesoscale Meteorological Processes* (translated from the Russian 1969 ed.). Israel Program for Scientific Translations, Jerusalem.
- Hughes, R.L. 1981 A solution technique for deep baroclinic rotating flows. *Dyn. Atmos. Oceans* 5, 159-173.
- Hughes, R.L. 1982 On a front between two rotating flows with application to the Flores Sea. *Dyn. Atmos. Oceans* 6, 153-176.
- Janowitz, G.S. & Pietrafesa, L.J. 1982 The effects of alongshore variation in bottom topography on a boundary current -- (topographically induced upwelling). *Cont. Shelf Res.* 1(2), 123-141.
- LeBlond, P.H. 1980 On the surface circulation in some channels of the Canadian Arctic archipelago. *Arctic* 33(1), 189-197.
- LeBlond, P.H., Osborn, T.R., Hodgins, D.O., Goodman, R. & Metge, M. 1981 Surface circulation in the western Labrador Sea. *Deep-Sea Res.* 28A(7), 683-693.
- Macdonald, H.M. 1915 A class of diffraction problems. *Proc. London Math. Soc.* 14, 410-427.
- MacLaren Atlantic 1977 Portion of environmental impact assessment for exploratory drilling in the Davis Strait region south of Cape Dyer. November 1977.
- Marko, J.R., Birch, J.R. & Wilson, M.A. 1982 A study of long-term

sattelite-tracked iceberg drifts in Baffin Bay and Davis Strait. *Arctic* 35(1), 234-240.

Marsili, L.M. 1681 Osservazioni intorno al Bosforo Tracio o vero Canale di Constantinopli, rappresentate in lettera alla Sacra Real Maesta Cristina Regina di Svezia, Roma. [Reprinted in *Boll. Pesca, Piscis. Idrobiol.* 11, 734-758, (1935).]

Merkine, L.-O. & Solan, A. 1979 The separation of flow past a cylinder in a rotating system. *J. Fluid Mech.* 92, 381-392.

Miles, J.W. 1972 Kelvin waves on oceanic boundaries. *J. Fluid Mech.* 55, 113-127.

Nof, D. 1978a On geostrophic adjustment in sea straits and wide estuaries: theory and laboratory experiments. Part I: One-layer system. *J. Phys. Oceanogr.* 8, 690-702.

Nof, D. 1978b ----. Part II -- Two-layer system. *J. Phys. Oceanogr.* 8, 861-872.

Nof, D. 1984 Shock waves in currents and outflows. *J. Phys. Oceanogr.* 14, 1683-1702.

Oberhettinger, F. 1954 Diffraction of waves by a wedge. *Comm. Appl. Math.* 7, 551-563.

Osborn, T.R., LeBlond, P.H. and Hodgins, D.O. 1979 Analysis of ocean currents: Davis Strait - 1977, vol. I and II. APOA Rep. No. 138 (available from the Arctic Petroleum Operators Association, P.O. Box 1281, Station M, Calgary, Alberta, Canada T2P 2L2).

Packham, B.A. & Williams, W.E. 1968 Diffraction of Kelvin waves at a sharp bend. *J. Fluid Mech.* 34, 517-530.

Pedlosky, J. 1979 *Geophysical Fluid Dynamics*. Springer-Verlag.

Roed, L.P. 1980 Curvature effects on hydraulically driven inertial boundary currents. *J. Fluid Mech.* 96(2), 395-412.

Roseau, M. 1967 Diffraction by a wedge in an anisotropic medium. *Arch. Rational Mech. Anal.* 26, 188-218.

Sanderson, B.G. & LeBlond, P.H. 1985 The cross-channel flow at the entrance of Lancaster Sound. *Atmosphere-Ocean* 22(4), 484-497.

Sommerfeld, A. 1896 Mathematische theorie der diffraction. *Math. Ann.* 47, 317-341.

Sommerfeld, A. 1954 Optics. Academic Press.

Stakgold, I. 1968 Boundary Value Problems of Mathematical Physics, Vol. I and II. Macmillan.

Stommel, H. 1965 The Gulf Stream, 2nd ed. University of California Press.

Stommel, H. & Luyten, J. 1984 The density jump across Little Bahama Bank. J. Geophys. Res. 89(C2), 2097-2100.

Whipple, F.J.W. 1916 Diffraction by a wedge and kindred problems. Proc. London Math. Soc. 16, 94-111.

Whitehead, J.A. 1985 The deflection of a baroclinic jet by a wall in a rotating fluid. J. Fluid Mech. - in press.

Whitehead, J.A., Leetmaa, A. & Knox, R.A. 1974 Rotating hydraulics of strait and sill flows. Geophys. Fluid Dyn. 6, 101-125.

Appendix A

Derivation of the $O(\epsilon)$ equation for s_1

We derive an equation for s_1 , treating s_0 as a known function of x and y . If we add (6.7c) to (6.8c) and use (6.10) and (6.11), we obtain

$$(s_0 v_1)_x - (s_0 u_1)_y + s_1 \nabla^2 s_0 = 2s_0 s_1 + s_0 h_1. \quad (A1)$$

But, from (6.9b)

$$(s_0 v_1)_x - (s_0 u_1)_y = \nabla^2 (s_0 s_1) - h_1 \nabla^2 s_0 - \nabla s_0 \cdot \nabla h_1, \quad (A2)$$

so that,

$$\nabla^2 (s_0 s_1) - h_1 \nabla^2 s_0 - \nabla s_0 \cdot \nabla h_1 + s_1 \nabla^2 s_0 = 2s_0 s_1 + s_0 h_1. \quad (A3)$$

We eliminate h_1 in favour of s_1 using (6.14), which also gives

$$\nabla s_0 \cdot \nabla h_1 = \nabla s_0 \cdot \nabla s_1 + s_0 (\nabla s_0)^2 - (\nabla s_0 \cdot \nabla) (\nabla s_0)^2 / 2, \quad (A4)$$

from which, (6.17), the equation for s_1 , follows:

$$s_0 \nabla^2 s_1 + \nabla s_0 \cdot \nabla s_1 + (\nabla^2 s_0 - 3s_0) s_1 = W, \quad (6.17)$$

where

$$W = (\nabla^2 s_0 + s_0) [s_0^2 - (\nabla s_0)^2] / 2 + s_0 (\nabla s_0)^2 - (\nabla s_0 \cdot \nabla) (\nabla s_0)^2 / 2. \quad (A5)$$

But, from (6.16), we have

$$\nabla^2 s_0 + s_0 = [5s_0^2 - (\nabla s_0)^2] / 2s_0, \quad (A6)$$

so that, W simplifies to

$$W = [s_0^2 - (\nabla s_0)^2]^2 / 4s_0 + s_0^3 - (\nabla s_0 \cdot \nabla) (\nabla s_0)^2 / 2. \quad (6.18)$$

Appendix B

Behaviour of s_0 for small and large r

In this appendix we derive simple expressions for s_0 , which are valid for small, or large, distances from the apex of the corner. If we replace p with $p'=1-p$, then, for small r , we get from (6.22)

$$\nabla^2 p' \approx 0 \tag{B1}$$

and hence,

$$p' \approx (kr)^a \sin(a\theta), \tag{B2}$$

which is a potential flow streamfunction solution in a wedge π/a . Consequently,

$$p \approx p_p = 1 - (kr)^a \sin(a\theta) \tag{B3}$$

and hence,

$$s_0 \approx s_p = p_p^{2/3} = [1 - (kr)^a \sin(a\theta)]^{2/3} . \tag{B4}$$

s_p and the exact solution s_0 are shown on Figure 28a for several small values of r .

In order to get the behaviour of s_0 for large r , we note first that in this case, the integrand in (7.9) is a rapidly oscillating function of u and hence, most of the contribution to the integral comes from the vicinity of $u \approx 0$. Therefore, since for small u ,

$$\sinh(u/a) = \sinhu/a + O(u^3) , \quad (B5)$$

we get the approximate expression

$$p \approx p_1 = \frac{2b}{\pi} \int_0^{\infty} \frac{\cos(krsinhu/a) \coshu \, du}{\sinh^2u + b^2} , \quad (B6)$$

where $b = \sin(a\theta)$, for short. Replacing \sinhu with x , we get

$$p_1 = \frac{2b}{\pi} \int_0^{\infty} \frac{\cos(krx/a) \, dx}{x^2 + b^2} = \exp(-krb/a) . \quad (B7)$$

The function $s_1 = p_1^{2/3}$ and s_0 are plotted for comparison on Figure 28b for several values of r . They agree best near the boundaries, where most of the transport takes place.

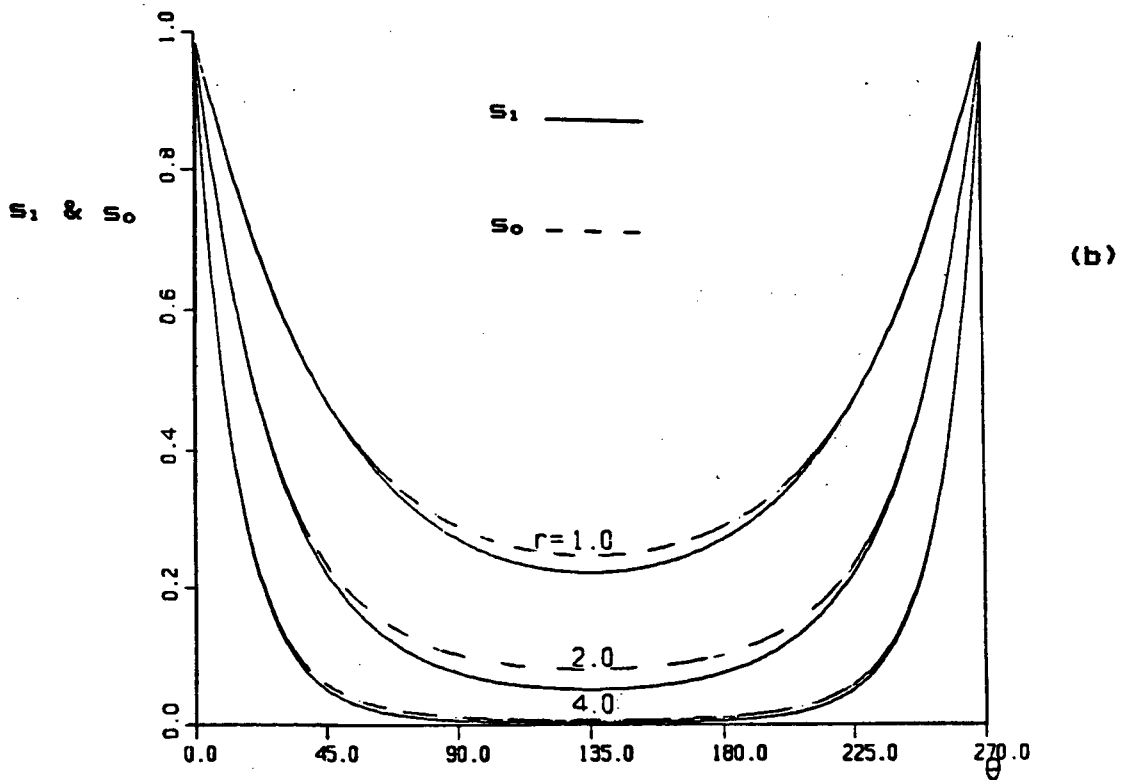
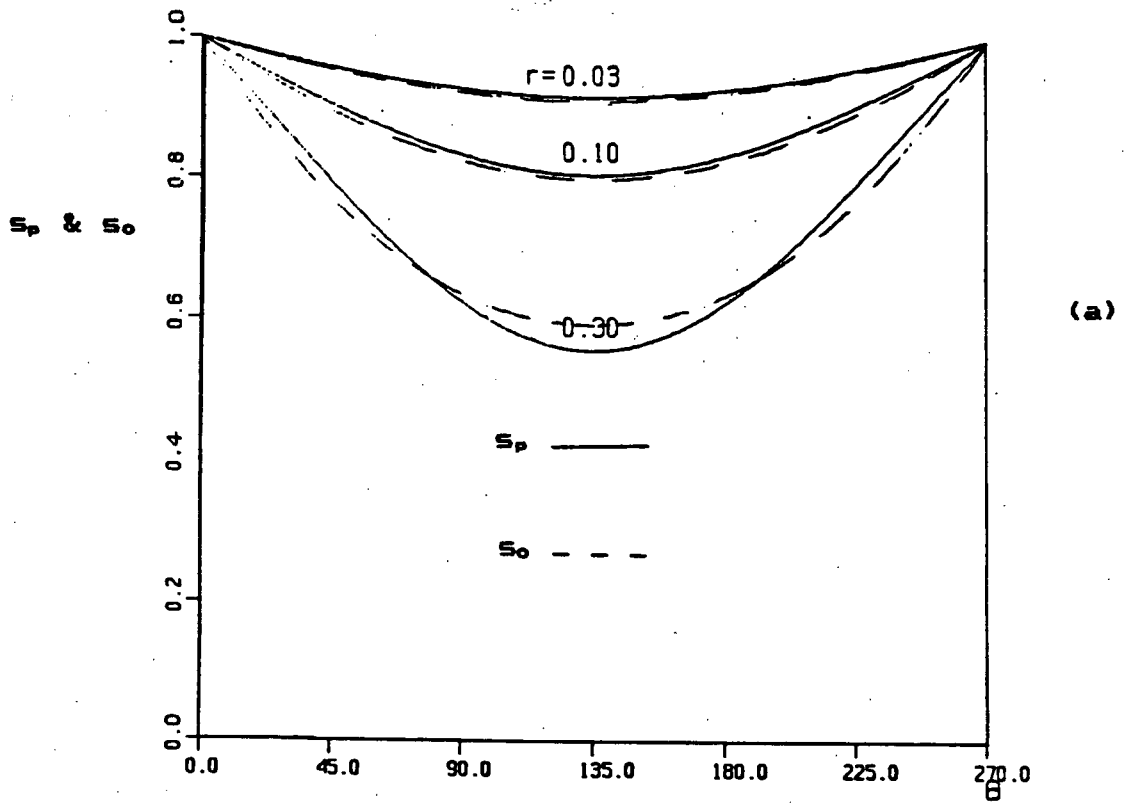


Figure 28. (a) An approximation s_p (solid) and the exact s_0 (dashed) for 3 small values of r . (b) As in (a), except for large r .

Appendix C

The extent of the centrifugal upwelling

In this appendix we follow the method of chapters 6 and 7 in deriving an explicit solution for the upwelling region at distances from the apex which are of the order of $\epsilon^2 X$. We are mostly interested in the size of the upwelling region, and not in exact details, so that no attempt is made to match the new solution to the one derived in chapter 7. We nondimensionalize, as in chapter 6, equation (6.1), except for

$$(x, y) = \epsilon^2 X(x', y'), \quad h = H(1-h') \quad \text{and} \quad \Psi = Q(1-2\epsilon^2\Psi'). \quad (C1)$$

The last scaling was used, since $\Psi \approx Q$ near the apex. Dropping primes, we get (as in chapter 6)

$$(1 - h) + \epsilon(u^2 + v^2)/2 = (1 - 2\epsilon^2\Psi)^{1/2} + \epsilon(1 - 2\epsilon^2\Psi) \quad (C2)$$

$$v_x - u_y + \epsilon = \epsilon(1 - h)[(1 - 2\epsilon^2\Psi)^{-1/2} + \epsilon] \quad (C3)$$

$$v(1 - h) = -\Psi_x \quad \text{and} \quad u(1 - h) = \Psi_y \quad (C4)$$

Expanding in powers of ϵ , while using

$$(1 - 2\epsilon^2\Psi)^{\pm 1/2} = 1 \pm \epsilon^2\Psi + O(\epsilon^4),$$

and retaining terms up to $O(\epsilon^2)$, we get

$$h_0 = 0 \tag{C2a}$$

and hence, $h = \epsilon h_1 + \epsilon^2 h_2 + \dots$. Similarly,

$$-h_1 + (u_0^2 + v_0^2)/2 = 1/2 , \tag{C2b}$$

$$-h_2 + u_0 u_1 + v_0 v_1 = -\psi_0 , \tag{C2c}$$

$$v_{0x} - u_{0y} = 0 , \tag{C3a}$$

$$v_{1x} - u_{1y} = 0 , \tag{C3b}$$

$$v_{2x} - u_{2y} = 1 - h_1 , \tag{C3c}$$

where we have used (C2a) to derive the last two equations. Also, we get

$$-v_0 = \psi_{0x} , \quad u_0 = \psi_{0y} , \tag{C4a}$$

$$-v_1 + v_0 h_1 = \psi_{1x} , \quad u_1 - u_0 h_1 = \psi_{1y} , \tag{C4b}$$

$$-v_2 + v_1 h_1 + v_0 h_2 = \psi_{2x} , \quad u_2 - u_1 h_1 - u_0 h_2 = \psi_{2y} . \tag{C4c}$$

Equations (C3a) and (C4a) give immediately

$$\nabla^2 \psi_0 = 0 , \tag{C5}$$

while from (C2b), together with (C4a), we get

$$h_1 = (\nabla \psi_0)^2 / 2 - 1/2 . \tag{C6}$$

Differentiating (C4b) with respect to x and y , respectively, and adding, upon using (C4a) and (C3b), we obtain

$$\nabla^2 \psi_1 = -\nabla \psi_0 \cdot \nabla h_1 . \quad (C7)$$

We multiply the first of (C4b) by $-v_0$, the second by u_0 and add, using (C4a). Then, from (C2c) we get

$$h_2 = \nabla \psi_0 \cdot \nabla \psi_1 + h_1 (\nabla \psi_0)^2 + \psi_0 . \quad (C8)$$

The solution of (C5), with $\psi_0=0$ on $\theta=0, \pi/a$, is

$$\psi_0 = r^a \sin(a\theta) , \quad (C9)$$

where the multiplicative constant was chosen to be unity, for consistency with the solution in chapter 7 (see also (C1)); this can be verified if we expand the nondimensional counterpart of (4.4) in powers of small x). We get from (C6)

$$h_1 = [(a/r^{1-a})^2 - 1]/2 . \quad (C10)$$

Note that, consistent with (C1) and an expansion of (4.2) in small x , $h_1=0$ identically for $a=1$. Using (C10), C(7) becomes.

$$\nabla^2 \psi_1 = -a^3(1-a)\sin(a\theta)/r^{4-3a} , \quad (C11)$$

with $\Psi_1=0$ on $\theta=0,\pi/a$. The solution to (C11) is

$$\Psi_1 = -a^3 \sin(a\theta) / [4(2a-1)r^{2-3a}] + C_1 \Psi_0, \quad (C12)$$

which is a sum of the particular solution, $\Psi_{1,p}$, and the solution of the homogeneous problem (C5), multiplied by an arbitrary constant C_1 , which, in general, is a function of a (the angular parameter). In order to be consistent with (C1) and the expansion of (4.4) in small x , we must have $\Psi_1=0$ for $a=1$ and hence,

$$\Psi_{1,p}(a=1) = r \sin \theta / 4 = -C_1 r \sin \theta,$$

so that $C_1(a)$ must satisfy $C_1(1)=-1/4$. That is as far as we get, without doing a formal matching with the solution from chapter 7. There are many functions of a that satisfy the last condition. In particular, we can use the power functions

$$C_1(a) = -a^b / 4, \quad (C12a)$$

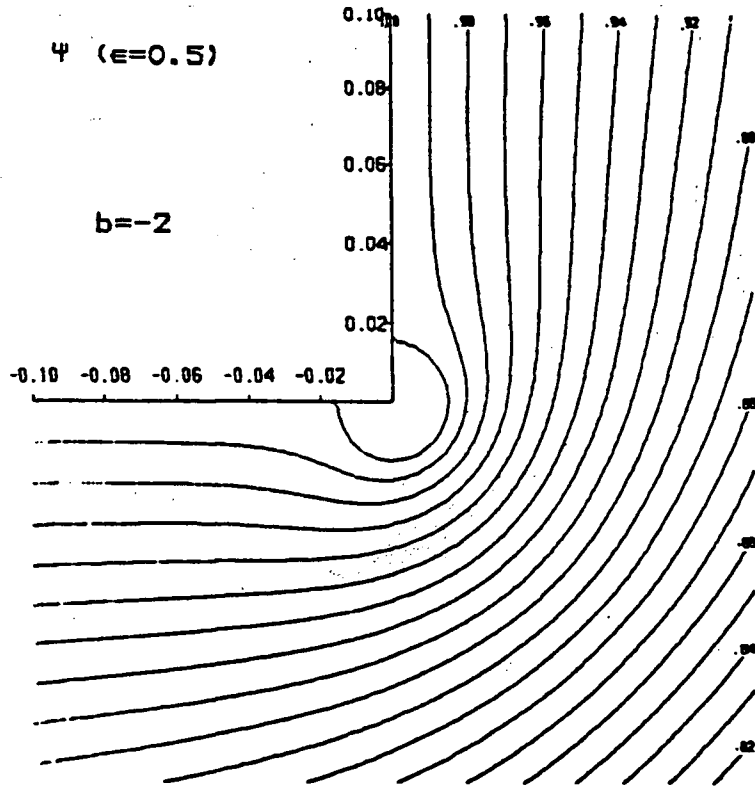
where b is any real number. We can narrow the choice of b if we demand, for example, that Ψ and h have a similar upwelling area.

After some algebra, we get from (C8)

$$h_2 = -\frac{a^4 [2(a-1) \sin^2(a\theta) - 5a + 2]}{4(2a-1)r^{4(1-a)}} + \frac{(2C_1-1)a^2}{2r^{2(1-a)}} + r^a \sin(a\theta). \quad (C13)$$

Again, we note that for $a=1$ ($C_1=-1/4$), $h_2=r\sin\theta$, which agrees with (C1) and the power expansion of (4.2), for small x . We tried several values of b (in (C12)), both positive and negative, and found that the best agreement between Ψ and h happens for $b=-3$. This is evident from Figures 29a-c, which show the plots of the total streamfunction $1-2\epsilon^2\Psi$ and the total depth of the interface $1-h$ (see (C1)) for three values of $b=-2,-3,-4$. We note that the effect of C_1 on Ψ is much stronger than on h . In fact, for $b<-4$, the area of upwelling shown by Ψ extends beyond the area plotted on these figures, while for $b>-2$, the upwelling area shown by Ψ is much smaller than the one shown by h .

What is more important, we have shown in this appendix that for $\epsilon=0.5$ the upwelling region is smaller than about $0.05X$. For example, if $X=20\text{km}$, this amounts only to about 1km radius.



(a)

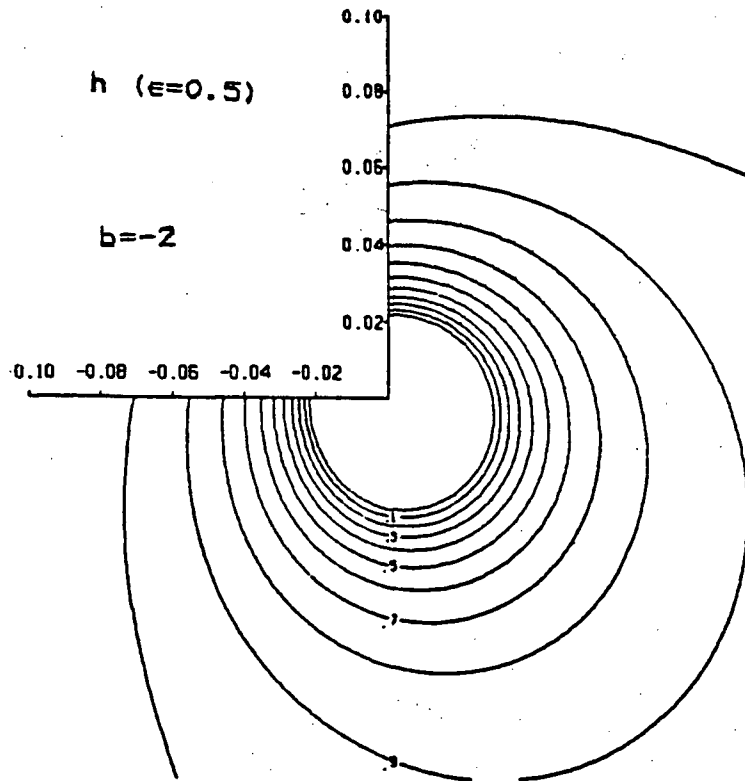
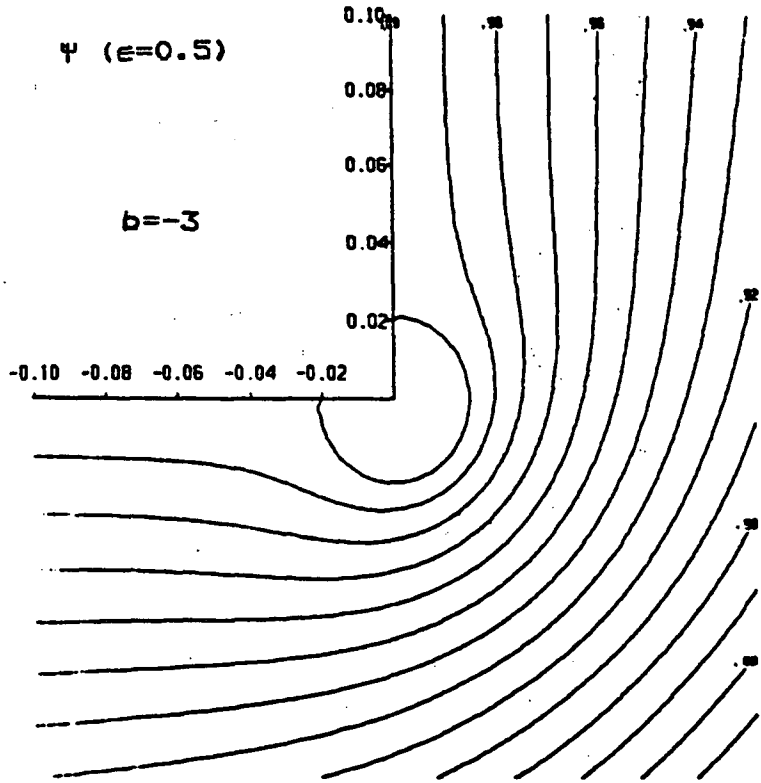
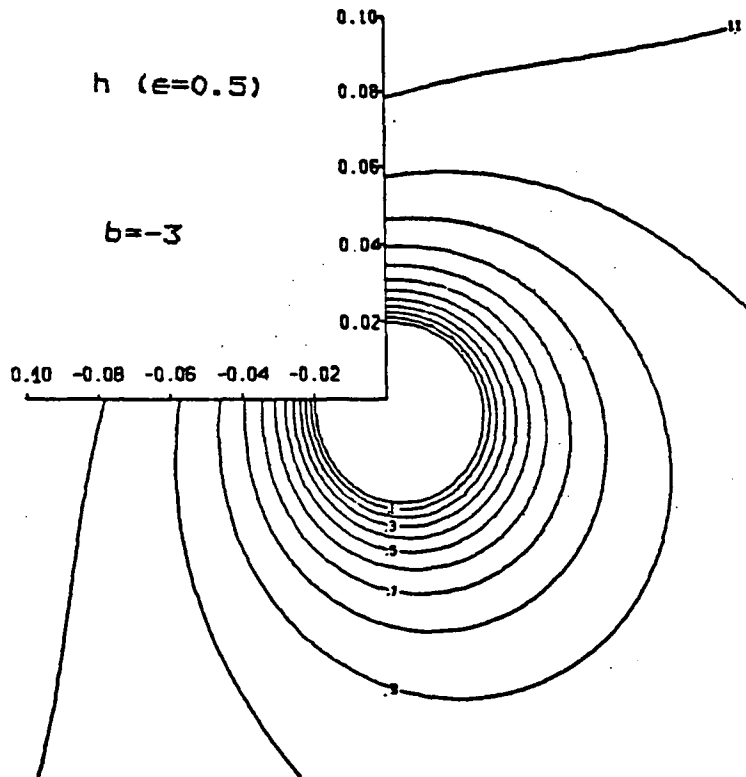
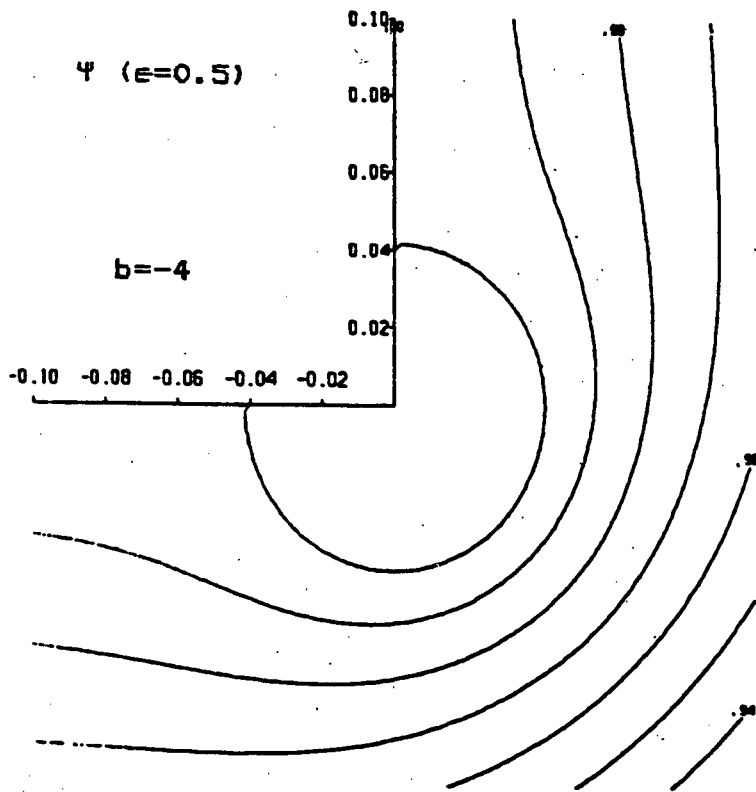


Figure 29. Contours of Ψ and h ($\epsilon=0.5$) for (a) $b=-2$, (b) $b=-3$ and (c) $b=-4$. The domain is 0.2×0.2 large and contour spacings are 0.1 for h and 0.01 for Ψ .



(b)





(c)

